ASSESSMENT OF THE MYELINATION OF CEREBRAL TISSUE USING MRI

MOHAMED EL BASHIR MUSTAFA EL SAYED

Department of Medical Physics and Bioengineering
University College London

submitted for
The Degree of Doctor of Philosophy
University of London
March 1999

ProQuest LLC.
789 East Eisenhower Parkway
P.O. Box 1346
Ann Arbor, MI 48106 – 1346

ABSTRACT

The aim of this study was to assess the myelination process of cerebral tissue in vivo using different Magnetic Resonance Imaging (MRI) techniques at high field strength and to suggest the optimum MRI technique for the correlation of myelination with the gestational age in the rat brain.

Several different techniques have been implemented in order to assess brain maturation. The first approach has been to quantitatively measure the Nuclear Magnetic Resonance (NMR) T_1 and T_2 relaxation times of brain gray and white matter which is shown to provide a certain degree of tissue characterization (Davis *et al* 1981). The second approach has been to measure the Apparent Diffusion Coefficient (ADC) which has proven to be of value in cerebral white matter which has been shown to demonstrate anisotropy of water diffusion (Chevert *et al* 1990).

Sprague Dawley (S/D) rats with different age groups ranging from 7 days to adult were used for this study. Studies were carried out in a 7T, 20 cm clear bore magnet (Bruker Biospec). Data were acquired using two different diameter inductively coupled saddle coils. Imaging pulse sequences used were the Spin Echo (SE) and the Stimulated Echo (STEAM).

Images were obtained with sufficient resolution to permit clear delineation of selected regions of interest in both gray and white matter. T_1 values did not show any significant difference with age in the selected regions of interest whereas T_2 and ADC values showed a marked change in signal intensity as the animals age increase.

The results obtained have demonstrated the feasibility of accurate high resolution quantitative MRI measurements in S/D rat brain. These techniques may be applied in the assessment of myelin related or white matter pathologies.

CONTENTS

List of Tables

List of Figures

Page No.

Acknowledgements

I wish to express my deep and sincere gratitude to Professor David Delpy for his valuable advice, practical assistance, constant support, continual encouragement and friendship while supervising this project.

I also wish to thank Professor Roger Ordidge for his guidance and help in understanding the intricate physics of the Nuclear Magnetic Resonance. I am grateful to Dr. Robert Speller for the opportunity to have such a valuable experience and gain knowledge in the Medical Physics and Bioengineering Department of the University College London. I am truly indebted to Dr. John Thornton, Dr. Matthew Clemence and Dr Rolly Blomberge for their help and practical assistance and continual encouragement during the progress of this project. I particularly want to thank Ernest Cady, Marzena Arridge and Richard Aldridge of the UCL Magnetic Resonance Spectroscopy laboratory for their co-operation and assistance. I must also include my colleagues Humberto Gamba, Patricia D'Souza, Gaby Pell, and Shonit Punwani all of whom were very friendly and helpful. In the Medical Physics Department my thanks go to David Plummer in the computer section of the department for his practical assistance with the computer work involved in this thesis. My thanks are extended to all the administration staff for their help. In the workshop I wish to thank Denzil Booth, Jose Pe'z, Billy Raven for their assistance in building the animal holders and the RF coils for this project.

I am grateful to my brother Abdul Rahman in Sudan, Mr. Tawfeig Mustafa and Mr.Ahmed Gama of the Sudan Embassy in London for their understanding and help.

My thanks also extended to my wife Amani and my little ones Huda Ahmed Heba and Mustafa for being beside me all the way.

CHAPTER (1)

Introduction

The medical need to see inside the human body from the outside has been met for many decades by recording the differential absorption of X-rays. A major deficiency of the standard method of radiography, it's inability to discriminate among overlapping structure was remedied in the 1970's by the development of X-ray computerized tomography, or CT scanning, a technique in which X-ray data recorded from many different directions are reconstructed mathematically to yield cross-sectional views of selected regions of any part of the body. Although CT scanning has proved to be an extremely useful diagnostic tool, the information its images provide is basically anatomical, they tell little about the functional or physiological state of the internal organs. Moreover, some pathological lesions have X-ray absorption properties so similar to those of the surrounding tissues that the lesions can go undetected in a CT scans unless they are large enough to change the size or shape of the organ. In addition X-rays, even in small doses, carry a finite risk of doing harm.

An alternative technique for obtaining cross-sectional pictures through the human body without exposing the patient to ionizing radiation is Nuclear Magnetic Resonance Imaging (MRI). This technique yields anatomical information comparable in many ways to the information supplied by a CT scan but also promises to discriminate more sensitively between healthy and diseased tissue. The latter prospect is founded on the well-established ability of NMR spectroscopy to elucidate the intricate conformation of organic molecules and to provide insight into dynamic chemical processes (Pykett et al 1982).

Imaging of the central nervous system (CNS) is nowadays one of the most important applications of medical MRI. The development of the human brain is incomplete at birth and this is reflected in the limited capabilities of the human

neonate, particularly when compared with the new-born infants of other species. In the prenatal period, myelination proceeds rapidly following the order of phylogenetic development, occurring first in the peripheral nervous system, then the spinal cord followed by the brain. Myelination in the brain occurs in different regions at different times. Although this process has been well studied in animals, the normal development of the human brain during the first decade of life has remained somewhat ambiguous and inaccessible to study in vivo. The sequential changes in the appearance of the postnatal brain have been incompletely characterized on the basis of autopsy studies. The unique sensitivity of magnetic resonance imaging to alterations in myelin content and in distinguishing between gray and white matter now provides the opportunity to trace the stages of brain maturation (Holland et al 1986).

It is generally agreed that the relaxation times T_1 and T_2 plus the proton density ρ (sec. 3.7) and diffusion (Chapter 7) are the quantities likely to give the best tissue discrimination in nuclear magnetic resonance imaging (Edelstein et al 1983). These parameters play a pivotal role in determining tissue contrast. Differences between hydrogen (^1H) NMR relaxation times of normal and pathological tissue are key to NMR image contrast and the discrimination of disease. They directly affect the selection of imaging pulse sequence timing parameters, and consequently, the total image scan time. They also influence the choice of the optimum magnetic field strength for MRI because of their significant variation with NMR frequency (Bottomley et al 1984).

The diagnostic utility of proton MRI is greatly enhanced when the image intensity is weighted with proton relaxation time information. This is because of the very significant variation of the proton spin-lattice (T_1) and spin-spin (T_2) relaxation times among various normal and abnormal soft-tissue structures which have essentially similar proton densities

The objective of the present study, which concentrates on normal Sprague Dawley rat brain tissue, is to assess the myelination process of the cerebral tissue in vivo using MRI and to suggest the optimum MRI technique for the assessment of important diseases involving delayed myelination and demyelination. Several different techniques have been implemented in order to assess brain maturation. The first approach has been to measure the NMR parameters T_1, T_2 of brain gray and white matter at the very high magnetic field strength of 7T available in the Bruker Biospec NMR system at UCL.

There are several reasons why it is useful to separate the individual contributions of T_1 and T_2 to the NMR signal. Firstly, in vivo measurements of these inherent tissue parameters may provide a useful diagnostic index, and might ultimately provide a certain degree of tissue characterisation (Davis et al 1981). Secondly, proton density and relaxation time data help elucidate the underlying physiochemical phenomena responsible for image alteration in diverse disease states and hence aid in the design of more sensitive imaging schemes. Thirdly, several design criteria for NMR imaging instruments and pulse sequences are intimately linked with the relaxation times of the object to be studied (Fischer et al 1990).

The second approach has been to measure the Apparent Diffusion Coefficient (ADC). This is a parameter which is monitored via the ability of MRI to visualize the diffusion of water molecules in biological tissue. This has recently been shown to be valuable as a means of evaluating the properties of brain tissues (Le Bihan 1990). Cerebral white matter has been shown to demonstrate anisotropy of water diffusion, which is relatively less restricted when measured parallel to the orientation of the myelinated white matter tracts and more restricted when the diffusion is measured perpendicular to the tracts (Chevert et al 1990). This means that an anisotropic index

map can be generated which may highlight the myelinated white matter relative to the surrounding tissue.

In this thesis the myelin formation and the demyelination processes are dealt with in chapter two. Possible myelin disorders are also listed in this chapter in an attempt to reflect the importance of this study which is primarily for the assessment of myelination pathologies. The phenomenon of magnetic resonance is introduced in chapter three where its history and development are reviewed, the underlying principles are explained and basic pulse sequences are described. MRI techniques and the pulse sequences used for collecting the data in this thesis are shown in chapter four. Chapter five describes the experimental work carried out and the results of T_1-relaxation time measurements for rat brain at 7T. This is followed by the results for T_2-relaxation times measurements as a function of gestational age in chapter six. The results of the Diffusion Weighted Images (DWI) are described in chapter seven. Chapter eight examines these results and discuss their validity in assessing the myelination process together with a conclusion which suggests future work.

CHAPTER (2)

2. Myelination and Myelin Disorders

2.1 Myelin

Myelin is a membranous structure present in the nervous system in the form of sheaths around axons. It is quantitatively and functionally of major importance in both the central and the peripheral nervous system (Norton WT *et al*,1984; Raine CS,1984). Myelin in the central nervous system (CNS) is different from myelin in the peripheral nervous system (PNS) in its composition and origin. In the PNS the myelin membrane is produced by Schwan cells whereas in the CNS oligodendrocytes are responsible for its production (Fig. 2.1). If we consider the central nervous system, the oligodendrocytes form flat cell processes which are wrapped around nerve axons in a spiral fashion (Fig. 2.2). The cellular cytoplasm disappears from these processes and the remaining cell membranes condense into a compact structure in which each membrane is closely opposed to the adjacent one. The myelin sheath is not continuous along the entire length of an axon, each oligodendrocyte furnishing myelin for only a segment of the axon. Unsheathed parts called the nodes of Ranvier, remain between the myelinated segments. The distance between the nodes is determined by the length of the myelin segments. Generally the larger the diameter of the axon, the longer the myelin segments and the thicker the myelin sheath (McDonald WI *et al*,1971; Friede RL *et al* 1982). A single oligodendrocyte provides the myelin for many internodal segments of different axons simultaneously. One oligodendrocyte may be responsible for the production and maintenance of myelin segments in up to 50 nerve fibres (Bologa L, 1985).

Membranes are composed predominantly of lipids and proteins and contain few carbohydrates. The lipid elements of membranes are cholesterol, glycolipids and phospholipids. Although myelin is an extension of the oligodendroglial cell membrane the chemical composition of myelin is quite different from the oligodendroglial cell membrane

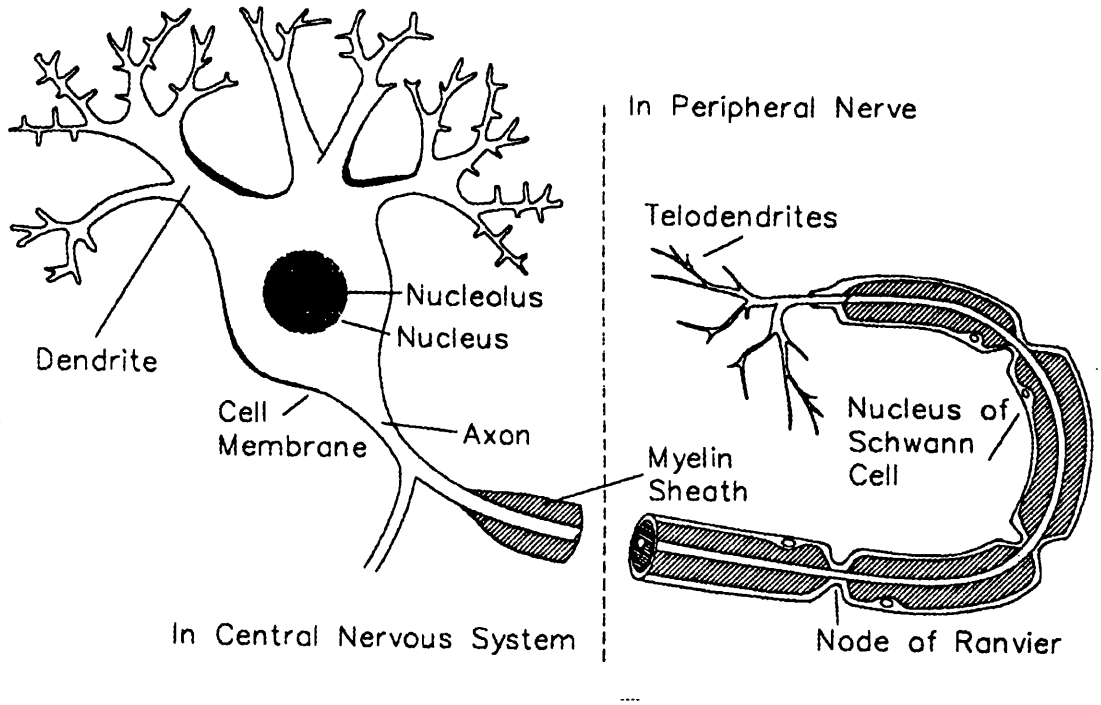

Fig. 2.1: *Myelin sheath in central and peripheral nervous systems respectively.*

in having a very high lipid content and low protein content (Norton WT, 1981 & 1984). Because of this special composition, myelin has an unusually stable and compact structure (Braun PE, 1984; Kirschner DA, *et al*, 1984; O'Brien JS, 1965). CNS white matter has a very high myelin content since it is composed of vast number of axons ensheathed with

myelin. These axons originate from neuronal cell bodies in the grey matter. Grey matter, therefore, contains only a small amount of myelin.

Initially, it was believed that the function of the myelin sheath was to isolate nerve fibres in order to prevent transfer of signals between adjacent axons. However its function in facilitating nerve conduction appears to be more important (Ludin HP, 1984; Ritchie JM, 1984).

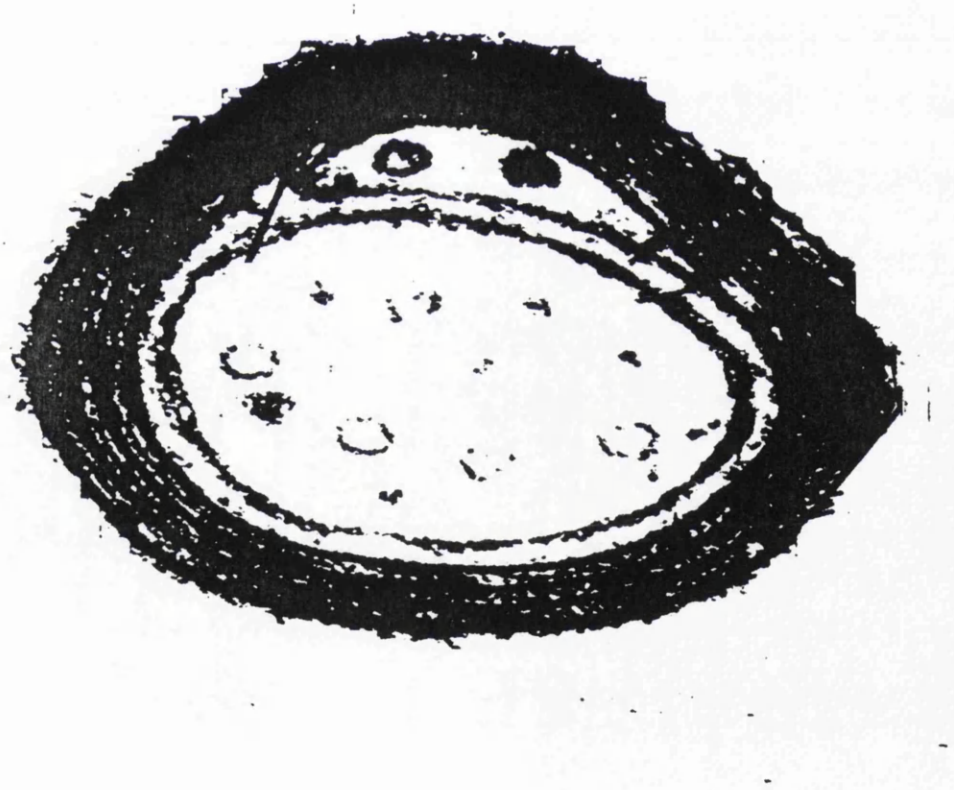

Fig 2.2: *Cross section through a typical CNS myelinated fiber from the spinal cord of an adult dog. Dark lines represent the protein layers separated by lipid. (from Pierre Morell, Myelin 1984)*

As the presence of myelin increases the resistance and lowers the capacitance of the underlying axonal membrane, the action potential is not conducted smoothly along the axonal membrane, but jumps from an uncovered part of the axonal membrane (node of Ranvier) over a segment of myelinated membrane to the next uncovered part and so on. The conduction velocity is increased considerably by this so called saltatory conduction. In addition, energy is saved because only parts of the axonal membrane need to depolarize and repolarize during impulse conduction.

2.2 Myelination Process

The brain is subject to major changes before and after birth. The process of myelination (Keene MFL, *et al* 1931; Brody BA, *et al* 1987) commences before birth in the spinal nerve roots and spinal cord. Towards the end of the second and beginning of the third trimester of pregnancy myelination starts in the brain stem tracts. Soon thereafter myelin appears in the cerebellar white matter and in the posterior limb of the internal capsule. At birth, most of the cerebral white matter is still unmyelinated, while myelin is present in considerable amounts in the brain stem, cerebellar white matter, internal capsule (Fig. 2.3) and corona radiata subjacent to the central sulcus (Fig 2.4). After birth myelin spreads over the reminder of the brain and it's density per fibre tract increases. The most important part of this process takes place during the first year of life with extension during the second and the third years of life. Myelination does not reach completion until early adult life.

The process of myelination is a highly controlled phenomenon evolving with regular times and sequences. It is therefore clear that there must be some initiating

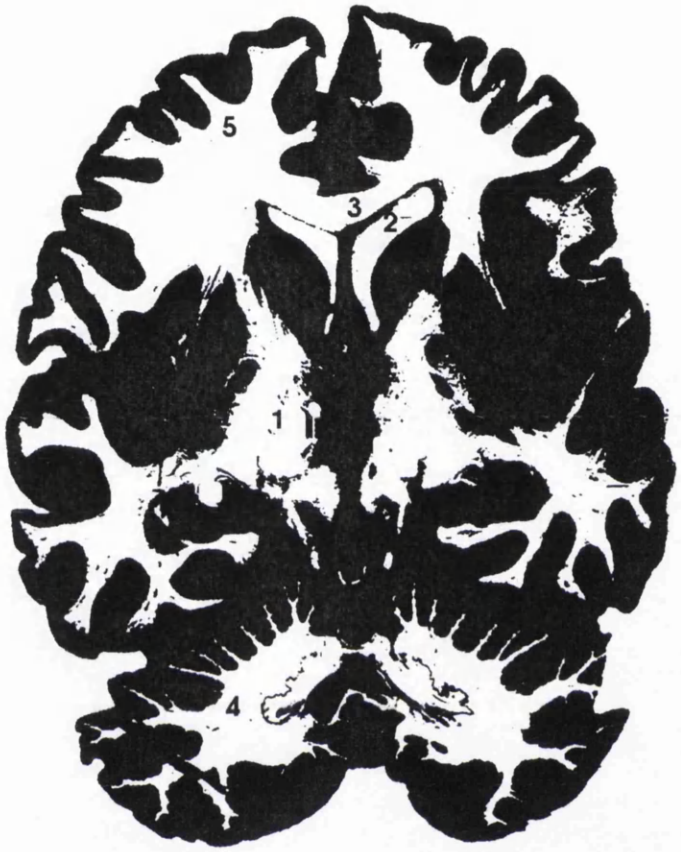

Fig. 2.3: *Horizontal section of human brain at the level of the basal ganglia showing 1- internal capsule 2- lateral ventricle 3- corpus callosum 4-cerebellum 5- cerebral white matter.*

stimulus of the onset of myelination and the factors controlling myelin formation. There is evidence that the axonal diameter is an important factor in initiating myelination and in determining the internodal length and the thickness of the myelin sheath (Friede R.L, 1972). The influence of the axonal diameter is particularly clear in the peripheral nervous system, but in the central nervous system this is less evident. Sometimes large diameter

axons have short internodes and very thin sheaths (Waxman SG, 1974). Hence, factors other than the absolute physical size of the axon must play a role in the initiation and the control of myelin formation. There is evidence that stages of postnatal development play a role in determining the relationship between axonal size and initiation of myelination (Remahl S, 1982). However, it has also been found that myelination is diminished by preventing the conduction of impulses along a nerve (O'Brien JS, 1970). This finding points to the importance of impulse conduction in a nerve as a stimulus for myelination. Although oligodendrocytes may form myelin in tissue culture in the absence of an axon (Szuchet S, 1986), it has been shown that oligodendrocytes require non-oligodendrocyte

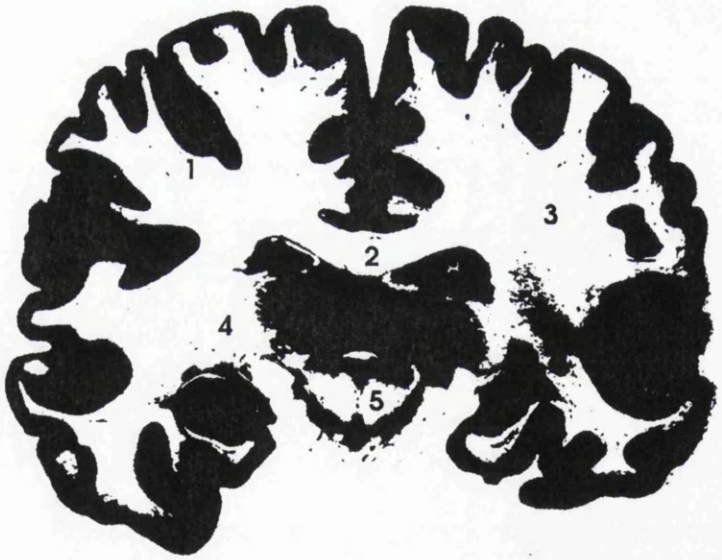

Fig 2.4: *Coronal slice of human brain showing: 1- cerebral white matter 2- corpus callosum 3- corona radiata 4- internal capsule (posterior limb) 5- midbrain.*

and specially neuronal signals for the optimal expression of myelin related functions (Bhat S, 1981). Addition of brain extracts leads to an increase in the number of oligodendrocytes in the culture (Pettmann B, 1980). There is therefore a oligodendrocytes-neuron interaction in myelination, but the mechanism of the interaction has not yet been completely elucidated. It is possible that this interaction is mediated by a chemical messenger secreted by neurons (Singer M, 1968) or by properties of axonal membrane (Waxman SG, 1985), or by properties of the oligodendroglial membrane (Brady RO, 1973), or a combination of these. Of course internal and external environment factors also play a role in the initiation and the regulation of the myelination, such as hormonal and nutritional balances.

After formation, the myelin sheath and axon remain mutually dependent. The myelin sheath needs an intact axon as demonstrated by studies on Wallerian degeneration. On the other hand, for maintenance of normal structure and function, the axon requires an intact myelin sheath. The precise nature of this mutual dependency is as yet undetermined

2.3 Demyelination Process

The term demyelination is commonly used to indicate the process of losing myelin, caused by primary affection of oligodendroglia or myelin membranes. Myelin loss that is secondary to axonal loss and simultaneous loss of axons and myelin sheath are not usually included under the heading demyelination. However, there is a considerable confusion about the meaning of the terms demyelination and demyelinating disorders. Some times, demyelination is used for all conditions in which loss of myelin occurs irrespective of whether the myelin membrane was primarily affected or was broken down secondary to or

at the same time as axonal loss (van der Knaap MS, 1991). This is partly due to the fact that it is not always clear whether the loss is primary or secondary in nature. The mutual dependency of axons and myelin sheaths is an important factor in this respect. Demyelination will eventually lead to axonal loss and axonal degeneration will in the end always result in loss of myelin (Lassmann, *et al.* 1978). Hence using histological examination, it may be very difficult to differentiate between primary and secondary myelin loss. Another confusing factor is that some disorders, e.g. gangliosidoses, show evidence of simultaneous occurrence of primary neuronal degeneration and primary demyelination. The random use of related terms, such as dysmyelination, myelinoclastic disorders, white matter disorders, leukoencephalopathies and leukodystrophies add to the confusion. Poser (Poser, 1961) introduced the concept of dysmyelimination. He proposed dividing the disorders characterized by primary myelin loss into "myelinoclastic disorders " and " dysmyelinating disorders " and he considered the former to be the true demyelinating disorder, in which the myelin sheath is destroyed after having been normally constituted. Examples are multiple sclerosis and acute disseminated encephalomyelitis. The dysmyelinating disorders comprise those disorders in which myelin formation is delayed or arrested or in which the maintenance of already formed myelin is disturbed. Examples are metachromatic leukodystrophy and adrenoleukodystrophy.

The idea behind the concept of dysmyelinating and myelinoclastic disorder is to distinguish between inborn errors of metabolism leading to myelin loss and acquired disorders characterized by primary myelin loss.

2.4 Myelin Disorders.

A large group of diseases of the nervous system possess, as a common pathological feature, foci in which the myelin sheath of the nerve fibres are destroyed. These foci, mainly situated in the white matter, vary in size, shape and distribution and also in the acuteness of the pathological process of which they are the result, but they are sufficiently similar in the different diseases to justify the appellation, demyelinating disease of the nervous system (Walton, 1985)

The aetiology of most of the demyelinating disorders remains obscure, though many seem to be due to a complex interrelationship of genetic, infective, immunological and biochemical mechanisms. Hence an aetiological classification of myelin disorders is rather difficult. Nevertheless, with the increase in knowledge in various fields of science over the years pathologists, biochemists and neurologists have sought ways of distinguishing between different disorders and have drafted classifications in an attempt to facilitate recognition of disease entities. Table 2.1 shows a classification which is based on dividing the myelin disorders into two main categories according to the cause: inherited and acquired disorders. The inherited disorders are caused by an inborn error of metabolism while the acquired disorders are secondary to adverse factors in the internal or external environment. This classification can not be considered final because, as shown in the table, the cause of a number of disorders is still unknown. However, the structure of this classification may allow easy integration of additional information with the scientific development.

Table 2.1: Classification of myelin disorder

I. Hereditary myelin disorders	II. Acquired myelin disorders
• 1. *Lysosomal storage disorders* a. metachromatic leukodystrophy b. globoid cell leukodystrophy (Krabbe's disease). c. Wolmann's disease and cholesterol ester storage disease. d. Niemann-Pick disease. e. GM_1 gangliosidosis. f. GM_2 gangliosidosis. g. fucosidosis. • 2. *mitochondrial dysfunction with leukoencenphalopath.* • 3. *peroxisomal disorders.* a. Zellweger cerebrohepatorenal syndrome. b. neonatal adrenoleukodystrophy. c. infantile Refsum's disease.* d. hyperpipecolic acidemia. e. pseudo-Zellweger syndrome. f. pseudo-neonatal adrenoleukodystrophy. g. X-linked adrenoleukodestrophy h. adrenomyeloneuropathy. i. classical Refsum's disease. • 4. *nuclear enzyme defects.* a. Cockayne's disease..	• 1.*noninfectious-inflammatory disorders* a. mutiple sclerosis. b. neuromyelitis optica. c. concentric sclerosis. d. Schilder's diffuse sclerosis. e. acute disseminated encephalomyelitis and acute hemorrhagic encephalomyelitis. • 2. *infectious-inflammatory disorders.* a. progressive multifocal leukoencephalitis. b. subacute sclerosing panencephalitis. c. progressive rubella panencephalitis. d. AIDS encephalitis. e. Creutzfeldt-Jacob disease. f. other infections. • 3. *toxic-metabolic disorders.* a. central pontine and extrapontine myelinolysis. b. vitamin B_{12} deficiency. c. Marchiafava-Bignami syndrome. d. malnutrition. e. toxic leukoencephalopathies (endogenous and exogenous toxins). • 4. *hypoxic-ischemic disorders* a. posthypoxic leukoencephalopathy.

5. *disorders of amino acid and organic acid metabolism.* a. Canavan's disease. b. other. • 6. *disorders of ganglioside anabolism.* a. GM_3 gangliosidosis.** • 7. *demyelinating disorders with unknown metabolic defect.* a. Pelizaeus-Merzbacher's disease b. Alexander's disease. c. congenital muscular dystrophy in combination with demyelination. d. cerebrotendinous xanthomatosis e. abetalipoprteinemia (Bassen-Kornzweig disease)	b. Binswanger's disease. c. other hypoxic-ischemic white matter lesions. • 5. *traumatic disorders* a. radiation. b. hydrocephalus.

* the presence of demyelination is questionable.
** the presence of this disease is questionable.

CHAPTER (3)

3. Nuclear Magnetic Resonance

3.1 Introduction

In this chapter the basic physics concept of magnetic resonance is summarised. There will be no discussion of Magnetic Resonance Spectroscopy (MRS) since MR imaging is the technique used in this study for the assessment of Myelination. The chapter starts by describing the early history and developments of the technique (3.2). followed by a summary of the general principles (3.3). Basic physics concepts of magnetization, precession, excitation and relaxation times with the appropriate pulse sequences for measuring the relaxation times will be discussed in the subsequent sections (3.4-7). The chapter will be concluded by description of a MRI system where the properties of the main components will briefly be examined.

3.2 Early History and Development.

Nuclear Magnetic Resonance (NMR) was seen for the first time by two independent groups, one under the leadership of Bloch (Bloch, Hansen and Packard 1946), the other under Purcell (Purcell, Torrey and Pound 1946). Both observations were made within a few days of each other and were reported in the same issue of Physical Review. Bloch and Purcell later shared the 1952 Nobel prize for their pioneering achievements. The discovery of chemical shift soon followed in 1949 by Proctor and Yu (Proctor and Yu 1950), and independently by Dickinson (Dickinson 1950). Their results, by a strange quirk of fate, were again published in the same issue of Physical Review. This technique allows nuclei in different chemical environments to be identified as a result of

the small change in resonant frequency caused by the electron cloud of the molecule. The first commercial NMR spectrometer appeared in 1953 (Morris 1986). Many of the applications of NMR in the 1950's and 1960's were concerned with investigations of molecular structure.

Although high-resolution NMR has developed as a versatile tool for studying the chemistry and structure of solids and liquids, the major recent biochemical and medical interest has arisen from the possibilities of making non-invasive measurements in living tissue. Initial measurements of ^{31}P spectra in intact blood cells were carried out by Moon and Richards (1973). The early experiments were limited by the small bore of the available magnets. Developments in magnet technology permitted phosphorus studies to be extended, initially to small animals and recently, with the advent of wide bore high field magnets, to studies of humans. ^{1}H , ^{13}C and ^{19}F spectroscopy can also be performed on these instruments. As in vivo NMR spectroscopy of animals and humans has become possible, methods of obtaining spatially localised signals from a well defined region of tissue have been developed.

In parallel with the development of spectroscopic techniques, methods of imaging the distribution of protons in tissue evolved. In 1973 the principle of utilising the shift in resonant frequency resulting from the imposition of a magnetic-field gradient was proposed by Lauterbur (1973), and by Mansfield and Grannell (1973). The early images that were formed were limited to small objects, but the first whole-body image was published in 1977 by Damadian *et al* (1977). These early results have been followed rapidly by technical and commercial developments, producing a variety of techniques that

allow proton images to be acquired, providing information on proton density and T_1 and T_2 relaxation times. Fast and real-time imaging methods have been developed, as well as methods for separating images from the protons in water and fat, and techniques for measuring blood flow in vivo. Whole-body systems are now available that permit both imaging and spectroscopy. Despite the rapid rate of development in recent years, NMR is still at a relatively early stage in its development and many further advances are likely. (Leach 1988).

3.3 General principles of NMR.

The physical principles of most aspects of diagnostic radiology have been concerned with interactions with the electron shells of atoms in the tissue, in particular the atom's ability to produce or attenuate electromagnetic radiation. However this is not the case for NMR. The term Nuclear Magnetic Resonance gives a good indication of the basis of the technique. It is the nucleus of the atom which is of interest in this technique and it's ability to resonate under certain conditions in the presence of a magnetic field. This resonance effect derives from a quantum mechanical origin, namely the existence of discrete sets of energy levels between which transitions can be observed . However, in the case of NMR, we are not dealing with electronic transitions but with nuclear ones. The particular property of the nucleus with which we are concerned is its angular momentum or spin which was suggested by Pauli in 1924 (see sec. 3.4). Therefore the technique of NMR can not be applied to any nucleus, only those nuclei which possess the property of spin and of particular interest are those with spin ½, (^1H for example). This is because

nuclei with zero spin give no signal and those with spin > ½ have an electric quadrupole moment resulting in a short NMR lifetime.

3.4 The nuclear spin system.

Many atomic nuclei exhibit the property of spin and since they bear electric charges, their spinning produces a magnetic moment μ aligned along the axis of the spin which expresses the strength and direction of the magnetic field surrounding the nucleus. The fields produced by these magnetic dipoles are analogous to those of a microscopic magnet Fig. 3.1.

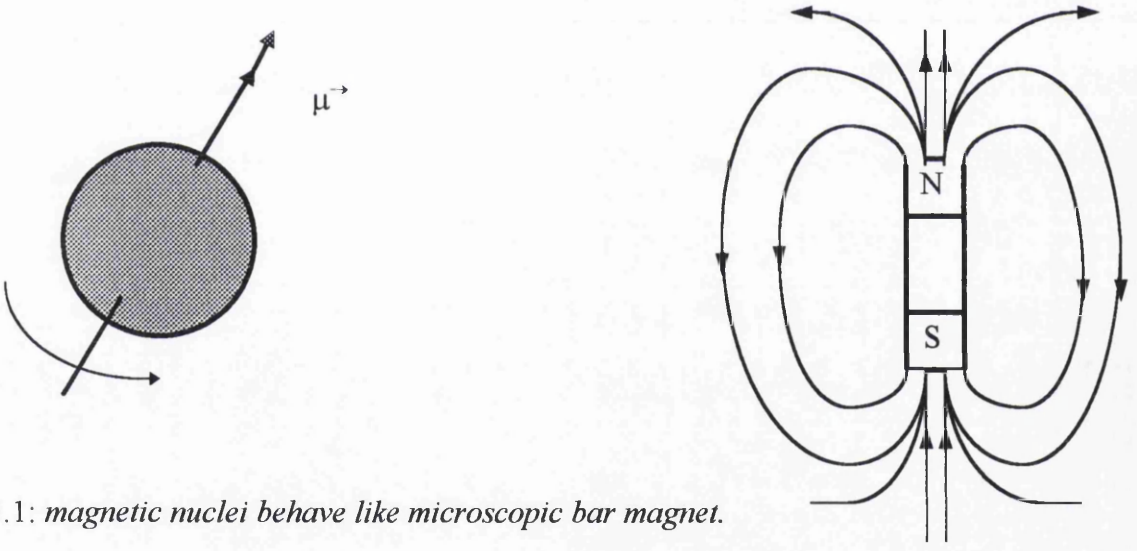

Fig. 3.1: *magnetic nuclei behave like microscopic bar magnet.*

Quantum mechanics tells us that the angular momentum of atomic nuclei can only have certain discrete values, specified by a quantum number I. The magnitude P of the angular momentum is given by,

$$P = hI/2\pi \qquad (3.1)$$

where h is Plank's constant. The quantum number I, usually called the spin of the nucleus, may only have integral or half-integral values which are governed by three simple rules namely

a) If the mass number is odd, I is half-integral.

b) if the mass number is even but the atomic number is odd, I is integral.

c) if both the mass and the atomic numbers are even, I is zero.

Nuclei of spin ½, such as ^{1}H, ^{13}C and ^{31}P are particularly important in NMR as these are the nuclei that give rise to signals of biological significance.

The angular momentum of a nucleus is a vector property, and in order to specify it's direction, it is necessary to introduce a second quantum number, m for it is found that the angular momentum vector can only take up certain discrete orientations with respect to the direction of an externally applied magnetic field. If we consider a field applied along the z-direction, for example, the component P_z of the angular momentum is given by,

$$P_z = mh/2\pi \qquad (3.2)$$

and so for a nucleus of spin ½, m can be ± ½. Hence the above relation can be rewritten as follows,

$$P_z = \pm \tfrac{1}{2}\, h/2\pi \qquad (3.3)$$

The magnetic moment of a nucleus is closely related to its angular momentum, in fact for a positively charged spinning particle, which the nucleus is, the magnetic moment acts in the same direction as the angular momentum, and has a magnitude μ given by,

$$\mu = \gamma P \qquad (3.4)$$

where gamma is a proportionality constant known as the magnetogyric or gyromagnetic ratio of the nucleus. Thus the component of the magnetic moment along the z-axis can be written as,

$$\mu_z = m\gamma h/2\pi \qquad (3.5)$$

substituting for $m = \pm \frac{1}{2}$ we get

$$\mu_z = \pm \frac{1}{2} \gamma h/2\pi \qquad (3.6)$$

these two spin states are shown in fig. 3.2.

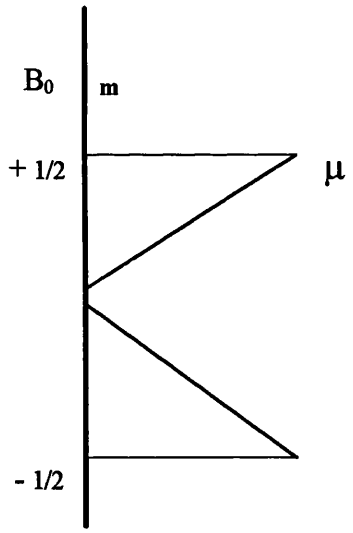

Fig. 3.2 *Quantisation of nuclear spin in the magnetic field for spin quantum number m=1/2.*

This means that for nuclei of spin ½, the only allowed orientation of the dipoles are parallel or antiparallel to the field. The two orientations have slightly different energies described as a Zeeman splitting of the energy level (Fig. 3.3).

At equilibrium in the presence of an external magnetic field the difference between the number of nuclei with spin up (parallel) and spin down (antiparallel) is very small, with a slight excess in the lower energy state (spin up). This small energy difference between the states leads to a very weak absorption of energy and is responsible for the inherently low sensitivity of NMR. The nucleus of the hydrogen atom contains only a single proton, that is why ^{1}H NMR is sometimes referred to as proton MR.

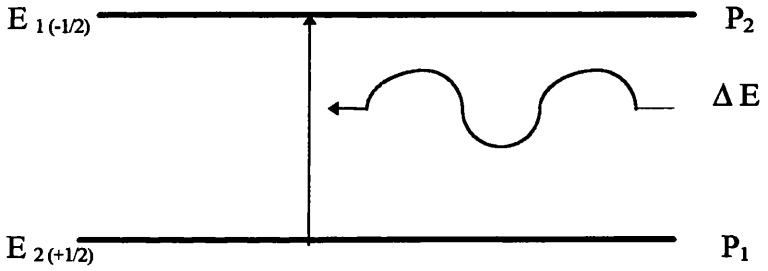

Fig. 3.3: *Transitions are induced by irradiating with energy that correspond to the difference between the two energy states. At equilibrium there is slight excess of spin population $P_1 > P_2$*

3.5 The Larmor precession frequency.

The difference in energy between the two spin states is governed by the equation,

$$\Delta E = \gamma h B_0/2\pi \qquad (3.7)$$

i.e. ΔE is proportional to the applied magnetic field B_0. In order to excite a transition from one Zeeman state to another it is necessary to supply an energy quantum (Fig. 3.3) given by the relation,

$$\Delta E = h\omega/2\pi = \gamma h B_0/2\pi \qquad (3.8)$$

where ΔE is the energy separation of the levels, γ is the gyromagnetic ratio in radians/sec/Tesla. B_0 is the magnetic flux density or the magnitude of the applied field and ω is the angular frequency (the rate of rotation in radians per second). From the above equation the frequency required to induce the energy transition is

$$f_0 = \omega/2\pi = \gamma B_0/2\pi \qquad (3.9)$$

and it is known as the Larmor frequency.

3.6 Motion of magnetization, the rotating frame and B_1 field.

Considering the practical situation of a sample comprising many nuclei, the net magnetic moment M will be derived from the vector sum of all the individual nuclear magnetic moments. Classical theory is inadequate to describe fully the behaviour of single spins because of the quantum nature of nuclear properties, but for a large ensemble of nuclei, the classical description is normally adequate. In a magnetic flux density B_0 the net magnetic moment of M at equilibrium will be aligned with B_0. As only the xy component of M gives rise to a measurable signal, M must be tilted away from B_0. This can be accomplished by applying a much smaller rotating magnetic field B_1 in the xy plane at right angles to the static (non rotating) field.

In order to understand how this process works it is most useful to introduce the concept of the rotating frame. By analogy with the laboratory frame, which has co-ordinates x,y and z, we may label the co-ordinates of the rotating frame x‘,y‘ and z‘(in fact z and z‘ are usually equivalent). The application of B_1 in the rotating frame causes the nuclear magnetization M to rotate about B_1 with angular frequency $\omega_1 = \gamma B_1$ (fig. 3.4). If the field B_1 is applied for time t_p, the nuclear magnetization will rotate through an angle

$\alpha = \gamma B_1 t_p$, and will rotate through an angle of 90° if t_p is such that $\gamma B_1 t_p = \pi/2$. A pulse of B_1 field that has this duration is known as a 90° pulse, and it's effect is to tilt the magnetization away from the z'-axis into the x'y'-plane of the rotating frame.

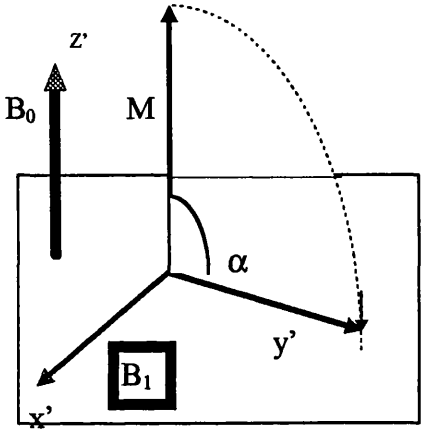

Fig. 3.4: *Transverse magnetization is induced by a radiofrequency field B_1 rotating synchronously with the precessing spins. If the duration of the B_1 field is sufficient to nutate the magnetisation by an angle of 90°, the entire magnetisation ends up in the transverse plane.*

In practice the rotating magnetic field is applied by surrounding the sample with a coil connected to a source of radiofrequency power. We should note that in order to tip the macroscopic spin vector away from the z-axis, the frequency of the applied electromagnetic radiation must match the natural precession frequency of the nuclei of the sample, hence the term nuclear magnetic resonance (Pykett 1982). When the cause of this nutation is removed, the magnetization is subjected to the effect of the static magnetic

field B_0 only and hence precesses about it. If a coil is now placed with its axis oriented along the y axis of the static coordinate system, an AC voltage will be induced in the coil which is given by:

$$V \propto M_0 \exp(i\omega t) \qquad (3.10)$$

where M_0 is the static magnetisation. Hence the oscillating transverse magnetization has a real and an imaginary component Fig 3.5 given by:

$$M_{im} \propto M_0 \sin(\omega t) \qquad [3.11a]$$

$$M_{re} \propto M_0 \cos(\omega t) \qquad [3.11b]$$

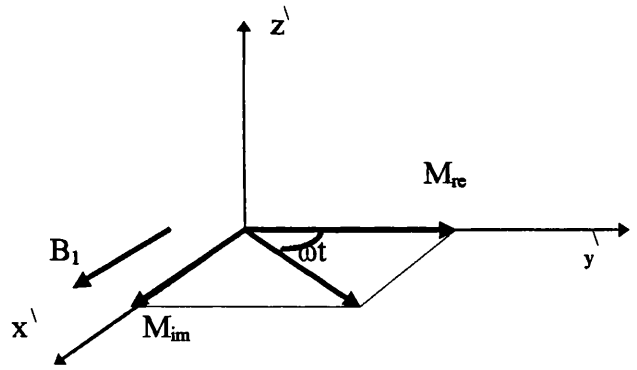

Fig. 3.5: *Transverse magnetization in the rotating frame of reference.*

The transverse magnetization does not persist. It decays to zero with a time constant T^*_2 and so does the amplitude of the detected voltage, V. Therefore the real component of the induced voltage may be written as:

$$V_{re} \propto M_0 \cos(\omega t) \exp(-t/T^*_2) \qquad [3.12a]$$

and the imaginary component as:

$$V_{im} \propto M_0 \sin(\omega t) \exp(-t/T^*_2) \qquad [3.12a]$$

The induced voltage has the characteristics of a damped cosine, which is also denoted as Free Induction Decay (FID) Fig. 3.6. The imaginary corresponds to the in-phase component of the transverse magnetization e.g. in phase with the B_1 RF field, whereas the real component corresponds to the out-of-phase component of the transverse magnetization (90° out of phase with B_1).

Figure 3.6 also shows the four components of an NMR signal which are the amplitude, the duration, the frequency and the phase.

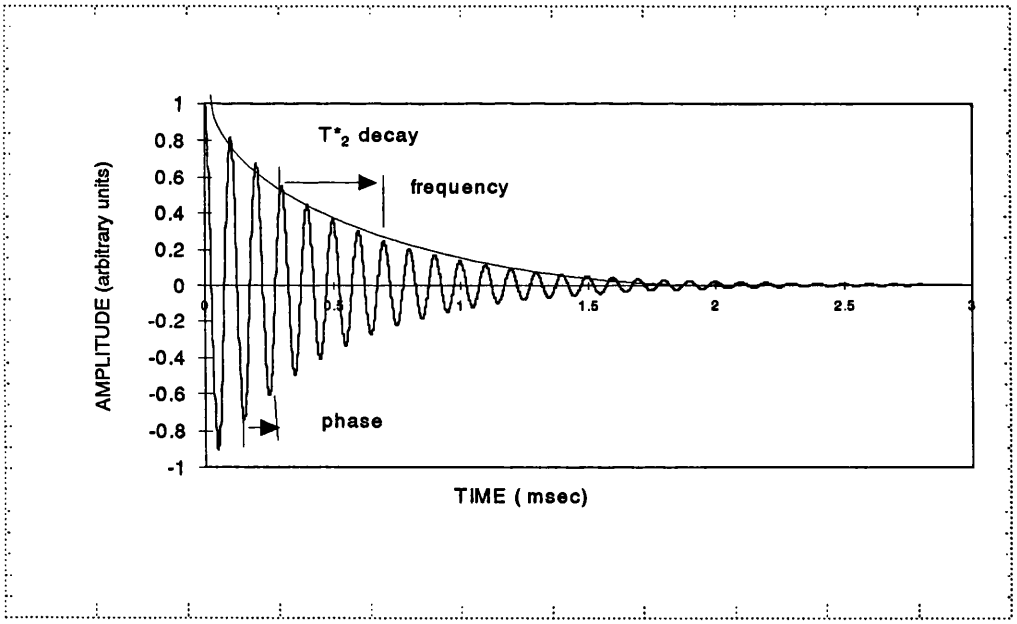

Fig. 3.6: *The real components of the transverse magnetization.*

This is simply the basis of practical NMR measurements where this signal is further processed to produce an spectrum or an image (Chapter 4).

3.7 Relaxation process and their measurements.

In 1946 Bloch *et al* proposed a set of equations, which for most purposes, accurately describe the behaviour of the nuclear magnetic moment of a sample of non-interacting or minimally interacting spins, such as a liquid sample. In a homogeneous field with flux density B, the equation of motion is given by;

$$d\overline{M}/dt = \gamma \quad \overline{M} \times \overline{B}_0 \qquad (3.13)$$

This equation of motion would allow the magnetization to precess forever once it had been excited, which is unrealistic. In practice we should expect the component of magnetization M_z to eventually revert to M_0, the equilibrium state, after a certain relaxation time following the excitation. There are, in fact two distinct relaxation processes that work in a spin system, each is characterized by it's own time constant, and these are named T_1 and T_2.

3.7.1 Longitudinal relaxation process.

This process is characterized by the T_1 relaxation time. In this process, the spin system loses energy to the molecular environment. Taking the static field as being in the z-direction, the magnetization energy will be M_zB_z , so when the spin system as a whole loses energy, it is M_z, the longitudinal magnetization, which reflects this loss. Left to itself, M_z decays exponentially back to M_0 with time constant T_1. It can be described by Bloch equation as follows;

$$d\overline{M}_z/dt = -(\overline{M}_0 - \overline{M}_z)/T_1 \qquad (3.14)$$

where T_1 is known as the spin-lattice relaxation time due to the exchange of energy between the nuclear spins and molecular framework, which is referred to as the lattice.

At the molecular level, the return to equilibrium depends on the local magnetic and electronic conditions at the location of the excited nuclei. For a given kind of nucleus, T_1 depends on several parameters such as:

a) the type of nucleus.

b) the resonance frequency (field strength).

c) the temperature.

In water-proton studies of biological systems, T_1 varies from a few hundred milliseconds for most tissues to over 1 sec. for cerebrospinal fluid, although there is a dependence on field strength. The T_1 of brain tissue shows a decline with age during maturation at low magnetic field strengths, and there are alterations due to pathological processes. The explanation as to how this occurs and the effect of the above mentioned parameters will be discussed later in sec 3.7.3.

3.7.2 Transverse relaxation.

This process is characterised by the time constant T_2. Here the spin system loses no energy as a whole but the spins can exchange energy amongst themselves. The net effect is a gradual loss of phase coherence in the processional motion of the spins, resulting in a loss of transverse magnetization. This process is known as spin-spin relaxation. However we should note that spin-lattice relaxation, the loss of energy from the system as a whole, also causes a decay of transverse magnetization. Therefore the

observed T_2 depends on both processes. One consequence of this is that T_2 can never exceed T_1, although in pure liquids they are very nearly equal.

From the equation of motion (equation 3.13), T_2 can be described from the magnetization component perpendicular to the z-direction as follows:

$$d\overline{M}_x/dt = -\overline{M}_x/T_2 \qquad (3.15a)$$

$$d\overline{M}_y/dt = -\overline{M}_y/T_2 \qquad (3.15b)$$

In practice, factors other than T_2 relaxation also cause loss of transverse magnetization. These additional factors together with the T_2 relaxation time affect the decay of the envelope of the FID or spin echo (sec. 3.8.2). The decay of the envelope is thus described by T_2^* (Fig. 3.6). This is primarily influenced by magnetic field inhomogeneities which give rise to a spread in frequencies for a given nucleus and therefore a loss in phase coherence, i.e.

$$1/T^*_2 = 1/T_2 + \gamma\Delta B_0/2 \qquad (3.16)$$

where ΔB_0 is the variation in magnetic field due to inhomogeneities.

3.7.3 Biological T_1 & T_2.

Hydrogen nuclei (i.e protons) giving rise to an NMR signal are mainly those in cellular water which constitutes by far the greatest proportion of hydrogen atoms in the body. Those in macromolecules such as proteins, lipids, and solid structures like bone do not usually contribute to the NMR signal because they tend to be immobile and therefore have a very short relaxation time. Hence, it is the behaviour of the water within the tissues

which largely determines the values of T_1 & T_2 in MRI. The biological mechanisms which influence T_1 and T_2 relaxation times are not yet fully understood, and although it is generally accepted that the concept of free and bound water gives the best understanding of T_1, it is still to some extent, an oversimplified model. In tissue a proportion of water is bound to the surface of proteins and as a consequence it's motion is slowed down by it's proximity to these larger molecules. This results in lowering the value of T_1. Other water in the tissue will not be bound to protein and is considered to be free, resulting in having higher T_1. In pure water T_1 is of the order of 3 sec. at a field strength of 0.1T. T_1 in tissue is much lower than this, and will depend on the relative proportions of free and bound water within the tissue. In summary, the larger the proportion of free water the higher the T_1, and the larger the proportion of bound water the lower the T_1. This may explain the assumption that T_1 increases in tumour tissue when compared with normal tissue and that this is due to the release of bound water into the tissue resulting in an increase in free water.

The effect of frequency on the two relaxation parameters is quite different. As the strength of the magnetic field increases the resonant frequency also increases (equation 3.9) leading to a change in T_1 (Mansfield and Morris 1982). It is not therefore possible to quote the T_1 value for a particular tissue without stipulating the frequency at which it was measured. This causes considerable difficulties in comparing in-vivo tissue measurements on patients obtained using different NMR systems, as often different field strengths are used. The magnitude of the change in T_1 with frequency can be appreciated by considering the T_1 of white matter in the brain which varies from 278ms at 0.08T (3.3 Mhz) to 500ms

at 0.26T (10.8 MHz) (Bydder *et al* 1982), and from 640ms at 0.4 T (17 MHz) to 1174 ms at 2.4 T (100 MHz) (Bottomley *et al* 1984).

Compared with the large variation in T_1 with frequency there is very little variation in T_2 with frequency (Gadian 1982). Most biological tissues have T_2 values in the range of about 50-150 ms. T_2 in free water is also longer than that in bound water resulting in an increase in T_2 in lesions within the tissues.

There has been some debate about the reason behind the difference in relaxation times in the grey and white matter of the brain. Protons in lipids have a lower T_1 value, and therefore the higher lipid content i.e. the lower water content of the white versus the grey matter was originally thought to be the explanation of the shorter T_1 in white matter compared with grey matter.

3.8 The Pulse Sequence.

The NMR signal has four separate components (Fig. 3.6) namely the amplitude or size of the signal, the frequency, the phase and the duration of the resonance. If a single NMR signal is obtained from hydrogen nuclei within a sample then the amplitude of the signal is proportional to the proton density. No information about T_1 & T_2 can be obtained from such a single signal. However, if a sequence of differing RF pulses is used then the amplitude of the NMR signal can be changed so that it contains information about T_1 & T_2 in addition to the proton density. This can be achieved by a pulse sequence design technique in which the timing of the pulse sequence is controlled to produce an NMR signal that contains the required information i.e. each pulse sequence is designed to provide certain information. There are many pulse sequences in use at present for

biological applications. The pulse sequences, which will be discussed in this section, are those which have been used to collect data in this study namely the Saturation Recovery (SR), Spin Echo (SE) and the Stimulated Echo (STEAM).

3.8.1 Saturation Recovery.

This is the simplest pulse sequence. In this sequence a 90° RF pulse is repeatedly applied to the sample and the NMR signal is measured after each RF pulse sequence (Fig. 3.7). The repetition time or the time between the pulses is referred to as TR. If TR is relatively long, perhaps 3-4 times the T_1 of the sample, then all the nuclei will have sufficient time to return to equilibrium before the next RF pulse. The amplitude of the NMR signal after each signal therefore contains only proton density information. If, however, the pulse repetition time TR is much shorter, for example approximately equal to the T_1 of the sample, then the nuclei do not have sufficient time to return to their equilibrium position before the next RF pulse and hence the NMR signal is smaller but contains information about the T_1 of the sample. The amplitude of the NMR signal in the Saturation Recovery pulse sequence is a function of the proton density, TR and T_1 according to the relation;

$$I = K \rho (1-\exp \{-TR/T_1\}) \qquad (3.17)$$

where I is the signal intensity, K is a constant comprising bulk flow, diffusion, perfusion and other parameters, and ρ is proton density. TR is the only variable in this sequence and it can be altered so that more or less T_1 information is contained in the signal. The faster the repetition time, (that is the shorter the TR), the smaller the NMR signal becomes and the more T_1 information it contains (chapter 5).

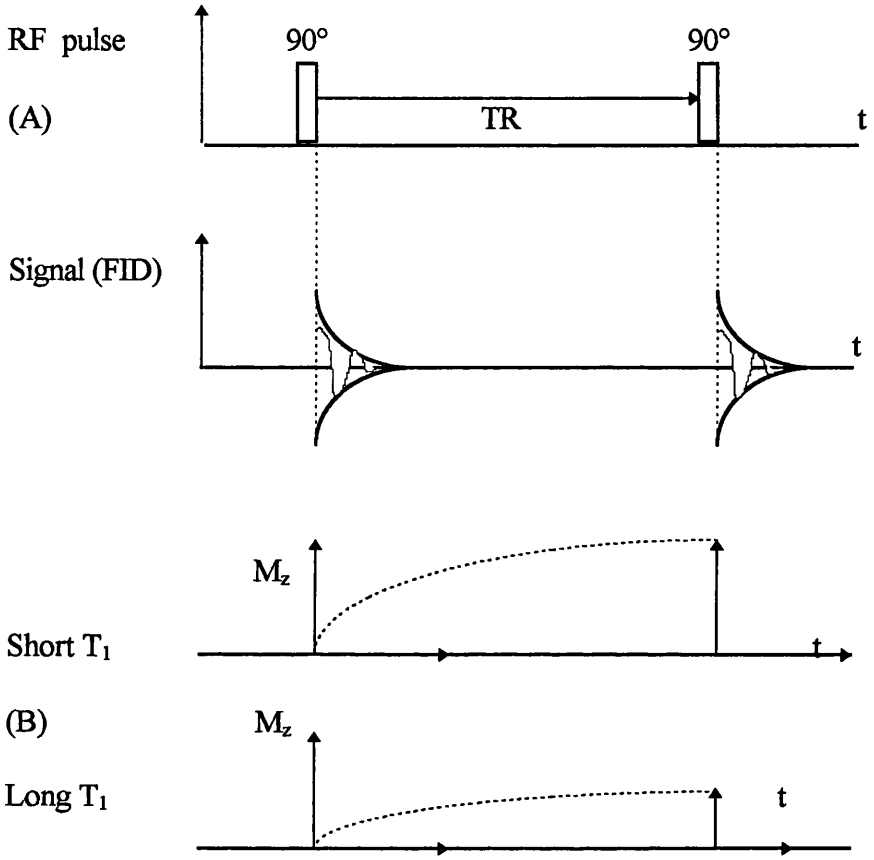

Fig. 3.7: *Saturation Recovery pulse sequence. An FID signal can be detected following a 90° pulse. The Repetition Time (TR) may be changed to reveal T_1 information (A). The effect of short or long T_1 for a given TR is illustrated (B), the short T_1 sample resulting in a larger NMR signal being produced than the long T_1 sample.*

3.8.2 Spin Echo.

The Spin Echo (SE) pulse sequence produces an NMR signal in which T_2 contributes to the signal in addition to ρ and T_1, is principally used to obtain T_2 information.

The physical principle of the SE (Hahn 1950) is that following the application of 90° pulse the nuclei initially precess in phase and then gradually they start to lose phase coherence due to the spin exchange, the reader is refered to (Stark and Bradley 1992) for more details. If after a short time interval, a 180° pulse is applied the nuclei will be inverted about the x-axis so that the position of the faster and slower precessing nuclei are reversed. The effect of inhomogeneities of the magnetic field on phase coherence is constant and so they gradually precess back into phase producing a large net magnetic moment and consequently a peak in the NMR signal which will occur after the 180° pulse and not after the 90° pulse as in the previous pulse sequences. Because of the delay in the appearance of the signal it is referred to as an Echo. The amplitude of the echo will be smaller than the original FID (which occurred immediately after the first 90° pulse) due to the irreversible loss of phase coherence caused by T_2. This process of rephasing the nuclei using 180° pulses can be repeated a number of times, the envelope described by all the echo signals being the T_2 relaxation curve.

The typical spin echo pulse sequence used for imaging contains one or two 180° pulses (Fig. 3. 8). The time between the 90° and the 180° combination is TR as in previous pulse sequences, and the value of TR, as in SR, will determine the T_1 contribution in the echo signal. The time between the 90° and the echo signal is designated as TE, the echo time.

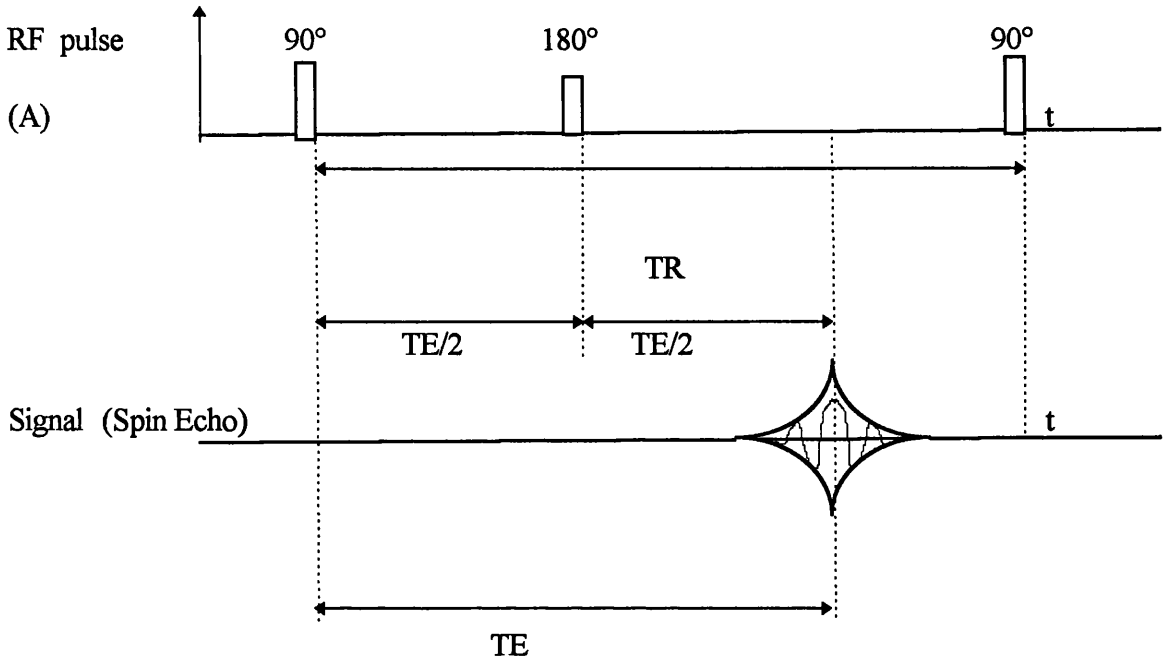

Fig. 3.8: *Spin Echo pulse sequence showing the time to echo (TE) and the repetition time (TR). The time between the 90° and the rephasing 180° pulse is TE/2.*

3.8.3 Stimulated Echo (STEAM)

A stimulated echo pulse sequence consist of three 90° RF pulses separated by time intervals TE/2 and T_m (Fig. 3.9).

This combination of three RF pulses results in several echo formations that occur at defined times. The echo that occurs at time TE/2 after the third pulse is called a stimulated echo (Hahn 1950).

The remarkable features of the stimulated echo are related to the magnetization evolution during the period T_m between the second and the third RF pulse. After the end of the second RF pulse, part of the transverse magnetisation (50% of the whole magnetisation) is stored as longitudinal magnetization. During the T_m period, longitudinal

magnetization thus experiences T_1 relaxation and not T_2. Since T_1 is usually much longer than T_2 in biological tissues, longer evolution times can be achieved than with a spin echo sequence without the usual signal penalty caused by T_2 decay. This feature is particularly useful for diffusion measurement (Chap. 7) when long diffusion times are required. Gradient pulses can be put within the first and third periods of the stimulated echo sequence. This sequence has been proposed for diffusion imaging by Merboldt *et al* 1991.

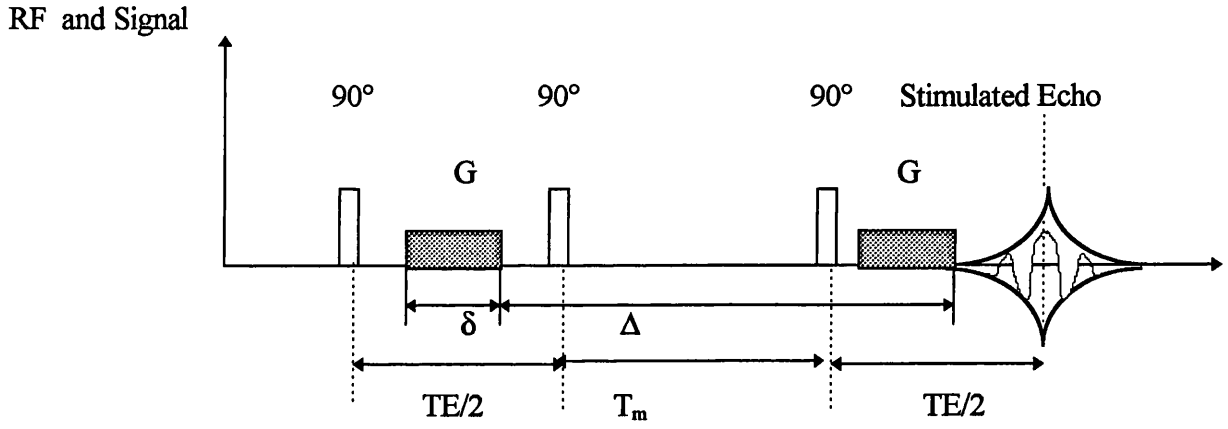

Fig 3.9: *Radio Frequency and Signal for stimulated echo pulse sequence where T_m is the mixing time, TE the Echo Time and G is the diffusion gradient.*

3.9 Basic instrumentation.

Despite the many variations in NMR scanning techniques, most instruments use similar basic hardware of which the principle items are; the magnet including three sets of field gradient windings and their drivers. The RF transmitter and receiver coils and their electronics, the preamplifier and the data acquisition and processing system.

This section describes most of these components briefly and discusses some of their properties which are important in obtaining good images and spectra. The characteristics of the systems used at UCL will where appropriate be given as an example.

3.9.1 The Magnet.

The magnet is perhaps the major component in an NMR system. The capability of an spectrometer is critically dependent upon the magnitude and homogeneity of the static magnetic field as well as the physical dimensions of the magnet. The magnet may be one of three different types namely, permenant, resistive or superconductive magnet. Permenant magnets run at lower cost since there are no electric power or coolant requirements. However, they have difficulty in producing a homogeneous and strong field over a large volume, and are extremely heavy, which make the transport and installation of such magnets rather difficult. The uses of this type of magnet are limited.

Most modern systems utilise either a resistive or superconducting magnet. The resistive magnets are used at low flux densities, 0.3T or below. They require a continuous power supply and generate a significant amount of heat, often being air or water-cooled. An important consideration in their use is the time taken for thermal stability to occur. Due to the high power requirements for magnetization and cooling, these magnets find limited use.

Higher field strengths are normally obtained by using cryogenic superconducting systems. These rely on the ability of certain materials to lose their resistance when cooled close to absolute zero (-273°C). The phenomenon of superconductivity was first discovered in 1911 by Kammerling Onnes in Leiden (Cady 1990), when he observed that

mercury lost it's resistivity at about -269°C. The first known superconductors were all pure metals and were able to achieve magnetic fields of only about 0.1T before the superconductivity "quenched". In the 1950's, a second generation of superconducting materials was discovered, consisting of alloys and intermetallic compound. These materials do not quench until fields of the order 10 to 16 Tesla are reached.

Most superconducting components for magnets are made of niobium-titanium alloy although other intermetallic compounds such as niobium-zirconium, niobium-tin and vanadium-gallium have been used. Almost all the magnets for biomedical magnetic resonance are constructed by using a composite wire manufactured by drawing niobium-titanium alloy strands, about 10μm in diameter embedded in a copper matrix. This material is stable and strong enough to withstand the great electromagnetic stresses that occur in large high-field magnets (Fig. 3.10).

For clinical imaging a large bore is required, the flux density may range from 0.05 to 2T. The homogeneity requirement typically being some 20 part per million (ppm) over the central 50cm of a 1m bore diameter. If spectroscopy is to be carried out on the instrument a homogeneity in the central 10cm of 0.1 ppm is usually required with a flux density of 1.5T or greater. Recent NMR systems using superconductor magnets can provide fields strong enough to carry out both imaging and spectroscopy. Homogeneity at such high field strength is achieved by built-in resistive coils in addition to the main superconducting magnet, which generate smaller, operator controlled magnetic fields. Some of these are used for shimming or making the magnetic field as uniform as possible within the sample so that all the nuclei of a particular type resonate at the same frequency

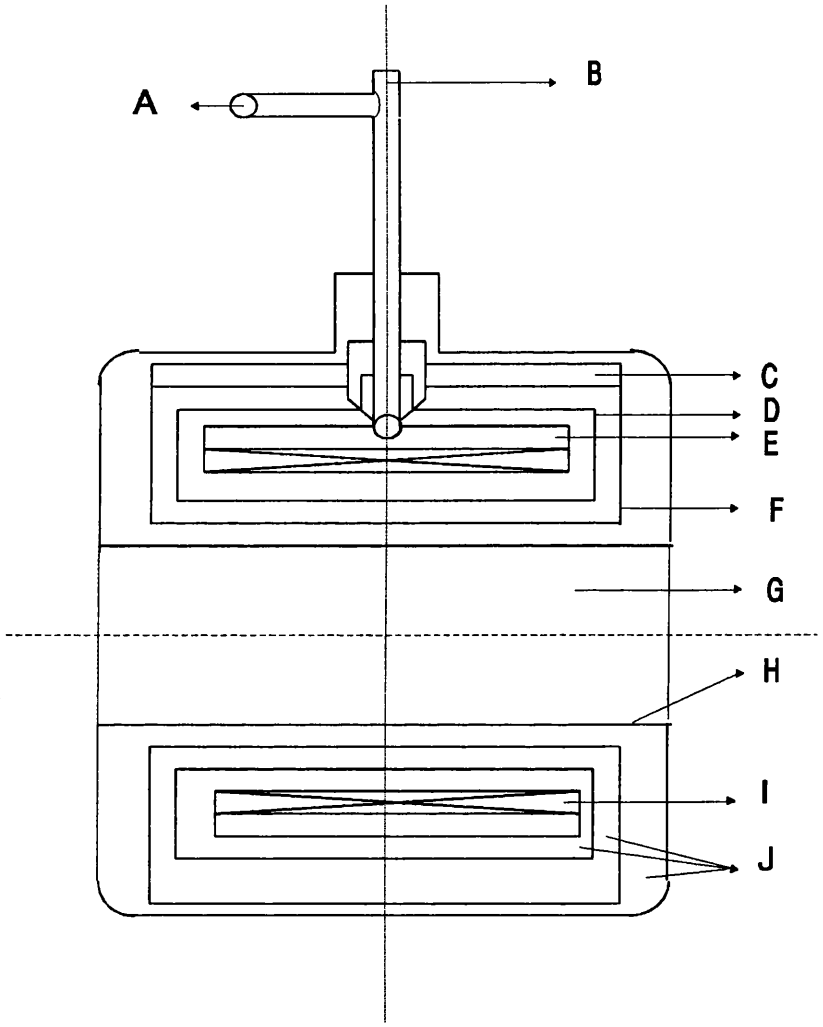

Fig. 3.10: *A cross sectional diagram through the whole body superconducting magnet showing A, helium gas vent; B, neck tube; C, liquid nitrogen; D, helium gas cooled shield; E, liquid helium; F, liquid nitrogen cooled shield; G, room temprature bore; H, outer vacuum case; I, superconducting coils; J, vacuum.(from Leach, 1988)*

and hence produce a well-resolved spectral peak. For some applications it may also be necessary to have gradient coils which are a set of three built in resistive coils to generate

magnetic fields directed along the z-axis but varying linearly in magnitude in the x, y and z directions. thus, they always add to or subtract from the main B_0 field. The magnetic field gradients are essential for imaging applications. For safety purposes the magnetic field strength of NMR systems in routine clinical use is currently limited to 2.5T maximum (Morris 1986). The systems used at UCL are a 2.35T instrument for studies on human infants, and a 7.05T system for animal studies. Both are multipurpose imaging/spectroscopy instruments. The work reported in this thesis has mainly used the 7.05T instrument. This is a Biospec series designed by Bruker Ltd, and intended primarily for biomedical research. The system employs a horizontal axis superconducting magnet with a bore diameter of 21cm. It has been provided with a multi-channel shim system under microprocessor control, it also has a special gradient system for both high field strength and fast switching in order to perform most known NMR experiments for imaging.

3.9.2 The RF Transmitter.

For a fixed-frequency system, the RF source can conveniently be obtained from a quartz-crystal oscillator, but if a variable-frequency system is to be used for multinuclear applications, a frequency synthesizer will be required. The function of the transmitter is to irradiate the sample with radio frequency fields of the appropriate frequency, power and timing. Therefore the RF system should provide non-selective and selective RF pulses of predetermined bandwidth and this is generally achieved by gating and modulation. This pulse processing is carried out prior to power amplification of the signal as shown in Fig. 3.11.

The modulation function is generally derived from a digital to analogue converter and the timing is controlled by a pulse programmer which constitutes part of the interface between the computer and the rest of the system.

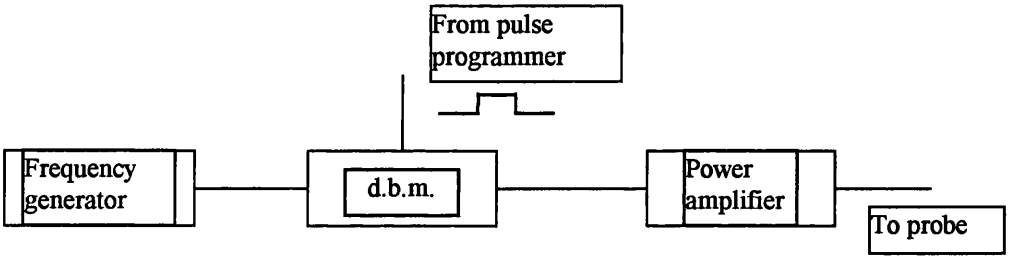

Fig 3.11: *A simple block diagram of the spectrometer transmitter where the double balance mixer (d.b.m.) provides signal modulation and gating.*

3.9.3 The RF coil and the Probe.

The RF magnetic field which is required to interact with the spin system can be achieved by placing the sample within a coil or inductance through which the RF current is passed. The coil basically consists of a combination of an inductor and a capacitor and normally forms part of a tuned circuit as shown in Fig. 3.12. The main characteristics of a particular coil are the frequency at which it resonates and the efficiency or quality factor Q. Hence the coil has to be tuned to the resonant frequency of the nucleus of the sample and should be matched to the impedance of the preamplifier input or the transmitter output (which is normally 50 Ω) so as to prevent reflection of power to the transmitter and ensure delivering of maximum power to the receiver. Tuning is usually performed via

a combination of fixed and variable capacitors, while impedance matching is carried out by using a variable capacitor only.

It is important that the coil be designed to possess a high Q to provide a larger signal for detection. Therefore, if we consider the transmitter coil L of Fig. 3.12 as forming a parallel tuned circuit which resonates at a frequency ω_0 given by

$$\omega^2_0 LC = 1 \qquad (3.18)$$

The quality factor Q of a resonant circuit is then given by

$$Q = \omega L/R \qquad (3.19)$$

where R is the RF resistance of the inductive element i.e the coil's conductor itself in this case. Diodes have the property that they only conduct when the forward bias voltage exceeds a certain level (about 0.6V in the case of silicon devices). The crossed diodes D_1 and D_2 shown in Fig. 3.12 thus provide a threshold barrier, removing low-level noise and cutting off the falling edge of the transmitter pulse.

Some coils are responsible for both transmitting and receiving the RF signal (transceiver),whereas others are responsible only for transmitting or only for receiving the signal. The optimum requirements for these two functions differ. Although many systems use separate coils for transmitting and receiving in order to eliminate the need for electronic switching between the two modes of operation, it is often desirable to use the same coil for both transmitting and receiving. However, in both cases it is necessary to provide protection for the receiver circuitry while the transmitter is transmitting to the coil. This is conveniently achieved by using crossed diodes with a quarter-wavelength coaxial line in the case of the transceiver. The passive circuit of Fig 3.12 can be used as a

transceiver. During the transmission phase, both sets of cross diodes conduct, those at the end of the quarter wave line effectively shorting out the receiver. This short circuit looks

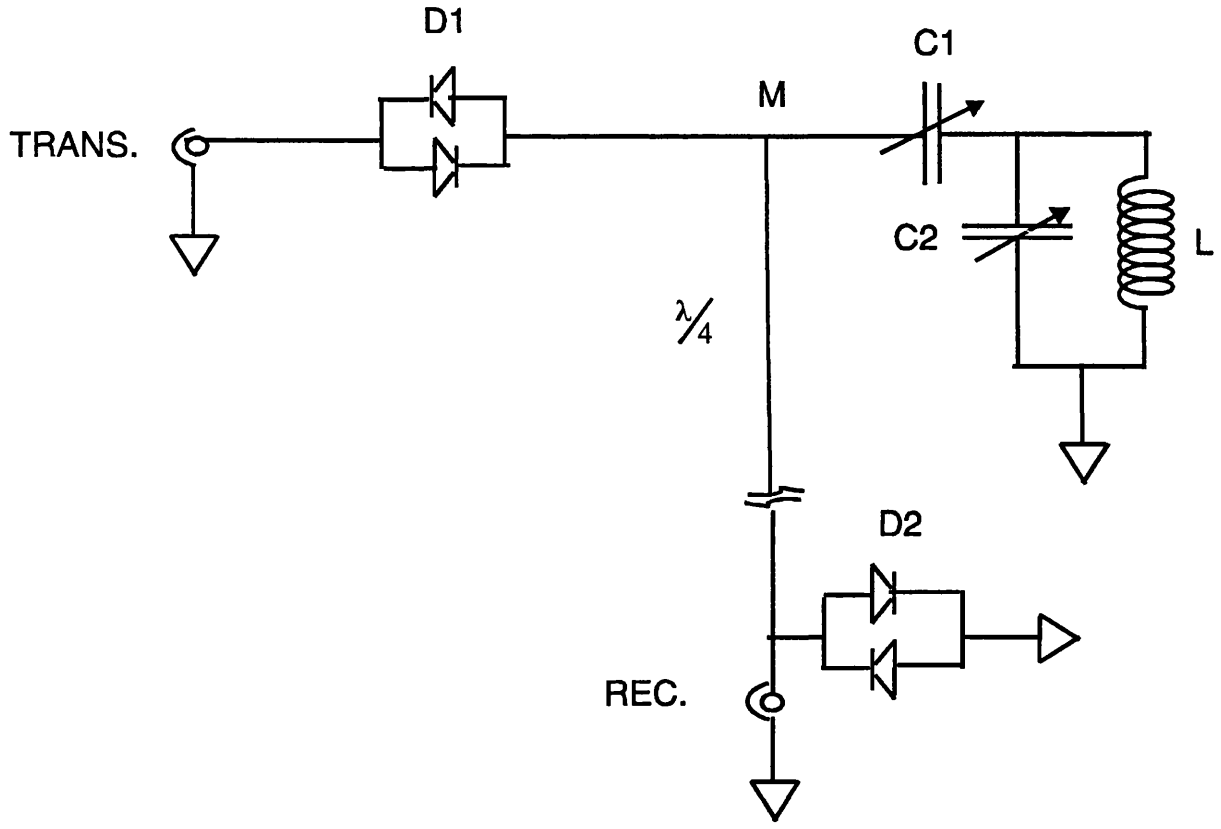

Fig. 3.12: *Passive receiver protection using crossed diodes and a quarter wavelength ($\lambda/4$) coaxial line. (from Morris P. 1986).*

like an open circuit when viewed from point M, so virtually all the transmitter power passes through to the tuned circuit. In the receiver phase, the induced e.m.f. is far too small to bias the diodes on, so the transmitter is effectively isolated and the short at the receiver input is removed (Morris 1986).

Many successful coils are of relatively simple design, often comprising one or more circular loops of highly conductive material, such as copper placed close to the sample. These are called surface coils. They are of great importance in spectroscopy. For imaging, a transmitter coil giving a homogeneous B_1 field is generally a primary requirement. This is achieved by using a probe which consist of a pair of saddle coils or at higher frequencies by arrangements such as the birdcage coil (Hayes *et al* 1985)

3.9.4 The Preamplifier.

The signal from the sample coil is in the order of a few μV. This signal should be amplified before significant noise or distortion is introduced, because at this stage, a small amount of additional noise can greatly degrade the signal-to-noise ratio that is finally obtained since the noise will also be amplified by the subsequent RF amplifier. The preamplifier task is therefore to amplify the signal at this stage.

Noise performance is normally measured in terms of a noise figure F which is defined as the ratio of the noise power at the output to that at the input, expressed in decibels dB as follows;

$$F = 10\log (N_A^2 + N_S^2)/ N_S^2 \qquad (3.20)$$

where N_A and N_S are the rms voltages of the amplifier and signal noise respectively.

A noise figure of 3dB indicates that the noise power is doubled by the amplifier and the S/N thereby reduced by a factor of $\sqrt{2}$. It is therefore important to ensure that the preamplifier selected has a noise figure which is less than 3dB. FET amplifiers have been designed for high-frequency with a noise figure of 0.3dB (Hoult and Richard 1976). Since the breakdown voltage of these FET's is rather low, it is essential to provide adequate

protection for the device during the transmitter pulse (such as crossed diodes). The amplified signal will then be fed to the receiver.

3.9.5 The Receiver.

The function of the receiver is to further amplify the signal from the pre amplifier and also change the frequency from RF to the more manageable audio frequency (AF). This change of frequency is often done via a middle stage using an intermediate frequency (IF). Ideally we wish to end up with an AF signal containing frequencies resulting from the difference between the NMR frequencies and a suitable RF reference frequency. This task is achieved by using a phase-sensitive-detector. The block diagram of Fig. 3.13 illustrate the general feature of a receiver system where the double balance mixer (d.b.m) acts as an RF gate and mixer.

It is appropriate here to consider the nature of the spectrum we hope to obtain. Typically, the NMR spectrum will be in the region of, say, 100MHz. It usually contains a mixture of resonances of a few hertz in width occupying a total spectral width of a few kilohertz. For such high frequency signals it is almost impossible to accurately detect or directly analyze the spectral characteristics. In addition no filter can easily select a region occupying only a few kilohertz at a frequency of 100MHz. Therefore the approach taken is to subtract the frequency f_1 of the applied B_1 field from the frequency f_0 of the NMR signals thereby generating a group of frequencies in the range of zero to a few kilohertz which are in the audio frequency range and which can easily be handled by the computer and be filtered adequately. The required frequency subtraction is accomplished with the

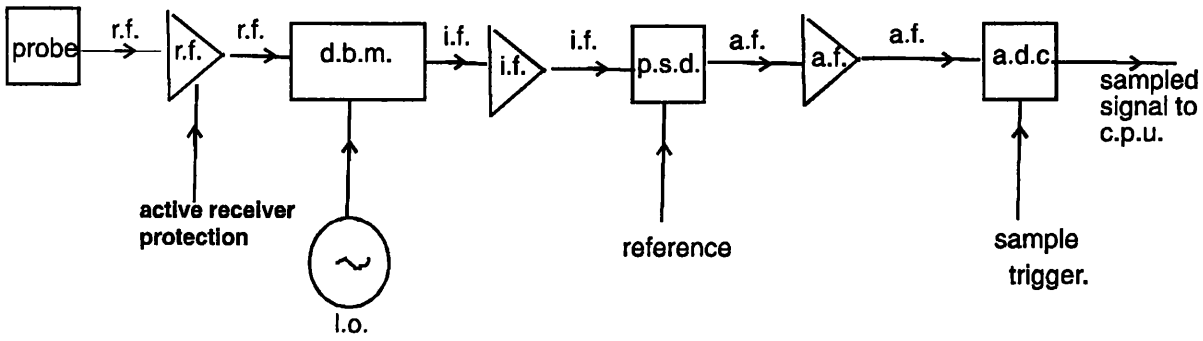

Fig 3.13: *Block diagram of the receiver system. r.f. radio frequency; i.f. intermediate frequency; a.f. audio frequency; p.s.d. phase senseitive detector; d.b.m. double balance mixer; a.d.c. analogue to digital converter; c.p.u. central processing unit.*

aid of the phase-sensitive-detector (PSD). The resulting audiofrequency is filtered and then amplified to the required level (usually 2V peak to peak) before being fed into the computer. The filter's function is to remove high-frequency noise which affects the S/N ratio. Many spectrometers convert the RF to an intermediate frequency of about 1MHz before the conversion to audio frequency.

An important drawback of the phase sensitive detector is that information is lost as to whether f_0-f_1 is positive or negative, resulting in all signals appearing on one side of the reference frequency following a Fourier Transformation. This can lead to errors in interpreting the spectrum. This problem is overcome by the use of two phase sensitive detectors in quadrature as shown in Fig. 3.14. In this situation the reference and signal are fed into two separate phase sensitive detectors where the phase of the reference is shifted

by 90° in one of the detectors (hence the term quadrature). The outputs from the two PSD differ in phase by 90°, but should be similar in all other respects. They are both filtered and amplified before being fed into two separate channels of the computer.

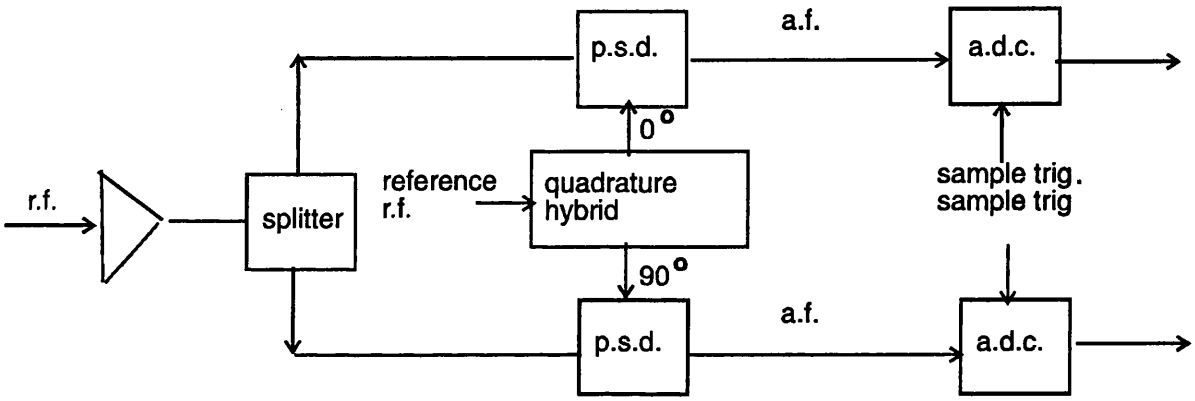

Fig 3.14: *Quadrature phase sensitive detection scheme.*

3.9.6 The Data Acquisition.

The initial RF signal processing starts in the receiver as discussed above, where it is changed from RF to AF. The next step is to measure the amplitude as a function of time and feed this information to the computer for further processing and accumulation. This is performed by the analogue to digital converter (ADC). The ADC samples the input waveform at regular intervals and converts the measured voltage to a sequence of binary numbers, which can then be stored into the computer memory. A fundamental theorem of digitization, according to Nyquist, states that the sampling rate must be greater than or equal to twice the highest frequency present in the signal to avoid aliasing. If the signal consisted of RF at 100MHZ, for example, then the ADC would have to sample at a

minimum of 200MHz (i.e 2×10^8 samples per second) for the duration of the FID. Whereas for a 10 kHz signal a much slower sampling rate is needed and far less computer memory is required without the loss of important information. This is a further advantage of changing the signal from RF to AF.

The computer of the NMR system has a wide range of functions. The main functions are to control the timing of the experiment, for example the pulse width and interval control, the accumulation of the data and the processing and display of this data. Following accumulation of the FID, the resulting signal must be processed in order to produce a spectrum or an image. This will include the utilization of Fourier transformation and a number of other additional mathematical steps such as the phase correction, sensitivity and resolution enhancement. Computers designed for use with NMR have a built-in Fourier Transformation program, This employs some form of the algorithm devised by Cooley and Tukey 1965, which is known as the Fast Fourier Transform (FFT). The FFT is a method which accomplishes a computational search of the input waveform for the frequencies and amplitudes present in the signal. By this process, an input which is an amplitude as a function of time is converted to an amplitude as a function of frequency and therefore will be ready for display and spectrum plotting as required. The block diagram of Fig. 3.15 illustrates the various components of a general n.m.r. system.

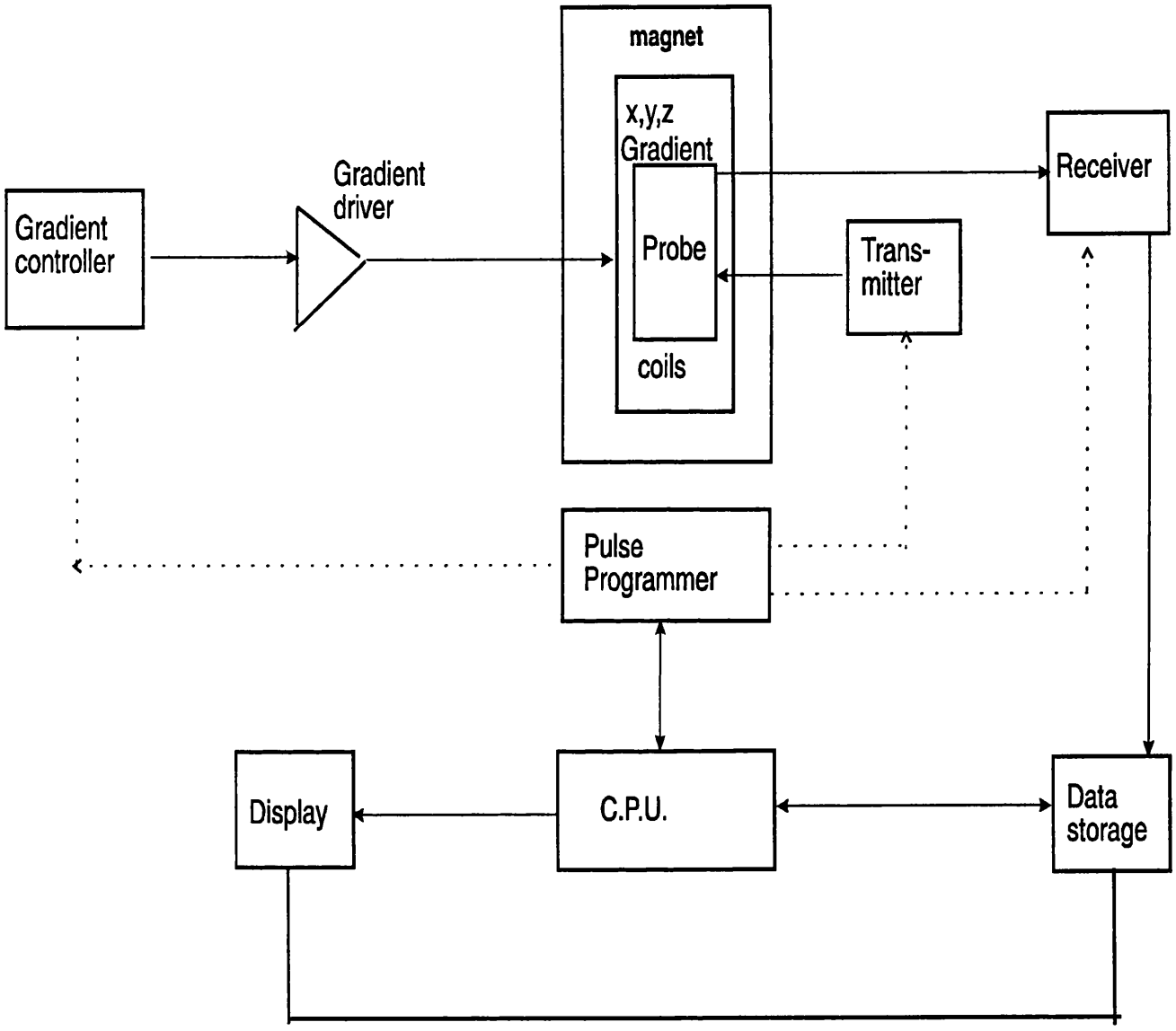

Fig. 3.15: *Schematic diagram of a general n.m.r. imaging system.*

CHAPTER (4)

4. Magnetic Resonance Imaging (MRI)

4.1 Introduction to MRI

The most important medical application of magnetic resonance is imaging. In order to create an image from a patient the magnetic resonance signal from the nuclei has to contain information about where the nuclei are positioned in the patient.

As mentioned earlier, the Larmor frequency is proportional to the magnetic field strength. If the main magnetic field is uniform across the sample, all the nuclei in the sample will precess at the same frequency. However, the frequency of the signal can be varied by changing the magnetic field linearly across the sample. This is done by imposing a field gradient and it forms the basic idea of spatial encoding. Field gradients are generated by a set of coils positioned within the magnet and can produce fields which vary uniformly with position along each of the three main axes (x,y,z). The linear field gradient, although much weaker - typically a few mT - than the main field, is strong enough to create a measurable range of resonance frequencies in the direction of the gradient. This range is directly proportional to the gradient strength i.e the stronger the gradient, the greater the range of frequencies.

With the help of gradients, one can also limit the spatial region being excited. Gradient excitation methods can be used to receive information on points, lines, planes (slices) and volumes, with the slice methods being the most common.

4.2 Basic Imaging.

The basic imaging experiment consists of three main parts 1) the excitation of selected spins, 2) the spatial encoding of the signal from the spins and finally

3) the signal detection.

4.2.1 Slice excitation.

The excitation of a sample can be achieved by applying an RF pulse. For imaging it is generally desired to limit the excitation to a region of the sample. Point and line excitation schemes are possible but the most widely used is the excitation of a slice within the sample.

An RF pulse applied in the absence of any field gradient will excite the whole sample. However, if a field gradient is applied at the same time as the pulse then the magnetic field and hence the resonance frequency changes with position, and only spins that resonate at the applied RF frequency will be excited i.e. a slice of spins in the plane perpendicular to the field gradient. The distance over which the resonance condition is valid is determined by the range of frequencies (bandwidth) produced by the RF pulse and the strength of the field gradient (Fig 4.1).

To produce an exactly defined slice requires that the RF pulse only excites a small and precisely defined range of frequencies. The band width resulting from a simple square (hard) RF pulse has a sinc (sinx/x) form and obviously does not fulfil this criterion. To improve the definition of the pulse bandwidth it is necessary to use a shaped RF pulse in which the amplitude of the RF is modulated during the pulse. Various shapes have been proposed for the modulating envelope, but the two most common forms are the Gaussian and Sinc envelope both of which are a considerable improvement over the simple square pulse. Although the Bruker system we are using can produce both the Gaussian and the Sinc envelopes, the pulse shape commonly used with this system is the Hermitian which

has an envelope shape between the Gaussian and the Sinc shapes.

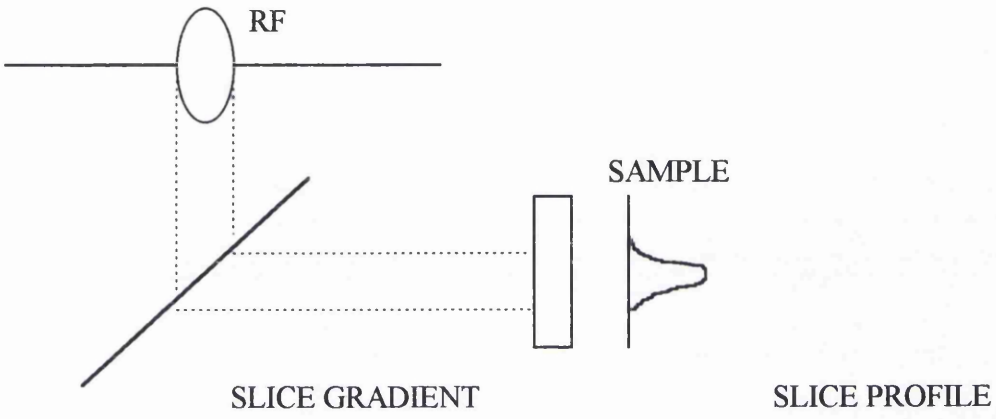

Fig. 4.1: *Combination of an RF pulse and field gradient producing selective excitation of a slice within the sample.*

The width of the profiles can be changed by altering the duration of the pulse or the strength of the gradient. If we apply a field gradient along the Z-direction and then apply an RF pulse, a transverse slice results. Changing the direction of the gradient to X or Y would result in a sagittal or coronal slice, respectively.

4.2.2. Spatial Encoding.

Selective excitation allows us to choose the spins from which we get a signal. If we assume that we have defined a slice we can now use spatial encoding techniques to tell us about their location within the slice. Two methods are commonly used for spatial encoding of the signal subsequent to excitation. The first is frequency encoding and the other is phase encoding.

4.2.2.1 Frequency encoding.

Frequency encoding is the name given to a procedure for resolving spatial information along one direction of an MR image. The key to frequency encoding is that a magnetic field gradient is applied along one axis while each MR signal is being measured. The magnetic field gradient is called the frequency encoding gradient or the read out gradient while the direction in space that is encoded is known as the frequency encoding direction.

The function of the frequency encoding in a 2D image experiment is to spread out the Larmor frequency over a range wide enough to distinguish 128 or 256 different locations along one direction. The actual number of locations is the number of picture elements (pixels) in an MR image along that direction. The Larmor frequency at the centre of the field of view (FOV), which is the distance between the edges of an MR image, remains unchanged by the frequency encoding gradient. However, the gradient increases the Larmor frequency on one side of the centre and decreases the Larmor frequency on the opposite side. The magnitude of the change depends on the distance from the center of the FOV to the particular location. If we apply a gradient across the sample and then measure the signal in the presence of the gradient we will obtain a range of frequencies which will now vary with position according to the following relation assuming the read gradient is applied along the X direction: [$\Delta\omega = \pm\gamma G_x \Delta x$]. The strength of the signal at any one frequency will depend on the number of spins which resonate at that frequency.

Signals from edge of the FOV are usually arranged to have the highest frequency that can be sampled accurately. These signals complete one cycle between each two data

points. The Nyquist sampling theorem specifies that at least two samples be acquired within each cycle.

4.2.2.2 Phase Encoding.

Phase encoding is a procedure to resolve spatial information along the other direction of an MR 2D image. Phase is encoded into MR signals by pulsing a magnetic field briefly before each echo is sampled. While the phase encoding gradient is on, the Larmor frequency is linearly proportional to position along the phase encoding direction. This is similar to the effect of the frequency encoding gradient

The phase encoding gradient is pulsed to a different amplitude before each MR signal. The number of different pulses is equal to the number of picture elements (pixels) along the phase encoding direction to form, with the pixels along the frequency encode direction, the 2D image matrix.

Following excitation of the spins the application of a gradient causes the spins to start dephasing at a rate which is proportional to the strength of the applied gradient. The total amount of the dephasing induced depends on the strength of the gradient, its duration and the position of the spin, expressed by :-

Phase Shift = 360°x 42.58 MHz/T x Gradient amplitude x Gradient duration x Position co-ordinate.

For example, suppose that the amplitude of the gradient pulse is 0.1 mT/m and its duration is 2 ms. This pulse will shift the transverse magnetization from a tissue that is 20 mm from the centre of the FOV by the following amount

360° x 42.58 MHz/T x 0.1 mT/m x 2 ms x 20 mm = 61°

The phase would be shifted twice as much 40 mm from the center of the FOV. Moreover, this pulse shifts the phase of the transverse magnetization from a structure 20 mm on the other side of the center by -61°.

The directions for the phase encoding and the frequency encoding can be swapped, when artifacts occur along the phase encoding direction such as ghosts caused by motion, or along the frequency encoding direction, caused for example by chemical shift. Swapping the directions chosen for frequency and phase encoding can redirect the artifacts onto less important regions of the image.

4.2.3. Signal Detection.

After the excitation of the spins and the spatial encoding, a signal now should be observed. In some cases the FID can be observed, but in most cases either a spin or gradient echo is created and observed.

By applying a Fourier Transform (FT) to the FID, which converts the NMR signal from the time domain to the frequency domain, a frequency spectrum can be obtain which represents a projection or "shadowgraph" of the sample along the direction of the gradient. A single projection contains only one-dimensional information and thus will not give an images but by changing the direction in which we apply the gradient and recording a second signal we can increase the amount of spatial information.

The original magnetic resonance imaging technique was the projection reconstruction or back projection which is equivalent to the techniques used in X-ray CT. It was used for the first demonstration of NMR imaging by Paul C. Lauterbur in 1973 and

was first dubbed Zeugmatography. This technique was based on stepping the direction of the applied gradient through 180° in small increments and recording a signal at each step.

In the creation of a 2D image we need to combine selective excitation with phase and frequency encoding. Subsequent to exciting a slice we need to apply a slice rephasing gradient, a phase encoding gradient, and turn on the frequency encoding gradient. The net effect is that only a very small signal would be present during the sampling period. This is due to the T_2^* decay of the signal and the dephasing effect of the frequency gradient applied prior to the sampling period. We can compensate for the latter effect by reforming an echo at the centre of the sampling period and this can be achieved by incorporating either a spin echo or a gradient echo into the sequence. The spin echo technique, which was discussed in chapter three, involves the application of a second, refocusing 180° RF pulse at a time TE/2 after the 90° excitation RF pulse. The effect of the second pulse is to reverse the sense of precession of the spins leading to the formation of an echo at a time TE after the excitation pulse. The frequency encoding gradient is designed such that at the centre of the echo there is no dephasing effect from the gradient (Fig. 4.2). In addition the effect of local field inhomogenities and chemical shift also cancel so the signal will have only experience T_2 (rather than T_2^*) decay at the centre of the spin echo. Alternatively following excitation it is possible to apply a negative gradient pulse along the frequency encoding gradient. If this gradient has the opposite polarity to the frequency encoding gradient this will start to reverse the dephasing accumulated during this period and an echo will form when the gradient areas are equal. Gradient echoes can be regarded as delayed FID signals and do not refocus the effects of main field imperfections or chemical

shift. Gradient echoes sequence are generally used with comparatively short echo times because the echo decays as T_2^*.

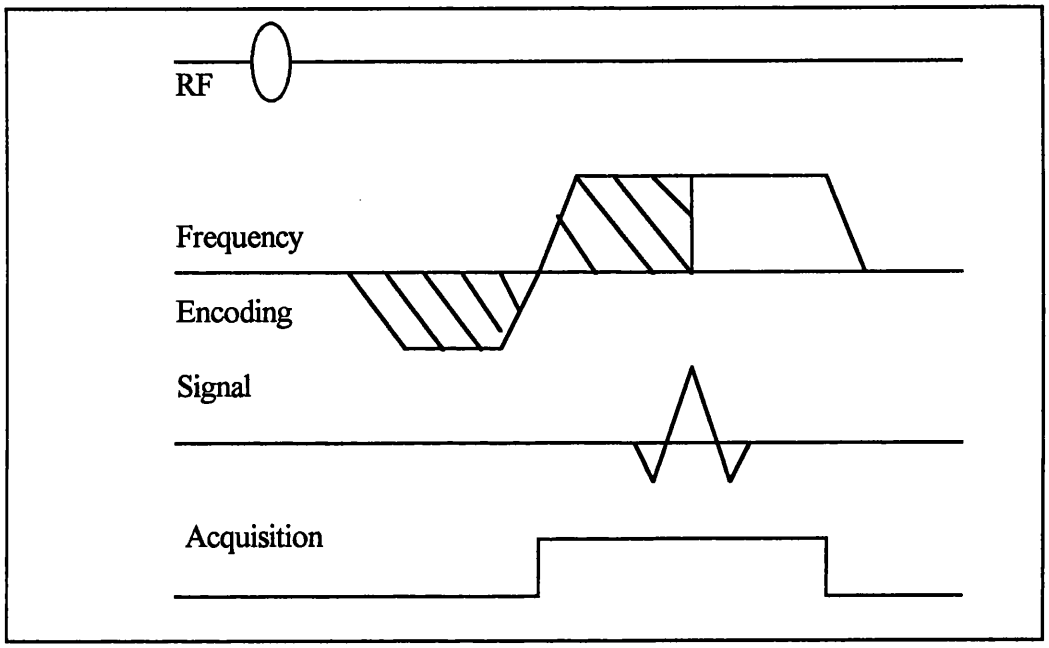

Fig. 4.2 : *RF pulse and frequency encoding gradient used to form a gradient echo.*

The signal resulting from the application of a selective RF pulse in combination with a field gradient produces much less signal than expected due to a phase shift which develops across the slice during the selective excitation of the slice. To compensate for this effect and hence restore the signal to the expected level we have to apply a gradient after the slice gradient which has a gradient area (gradient strength times duration) which is half that under the RF pulse (Fig. 4.3).

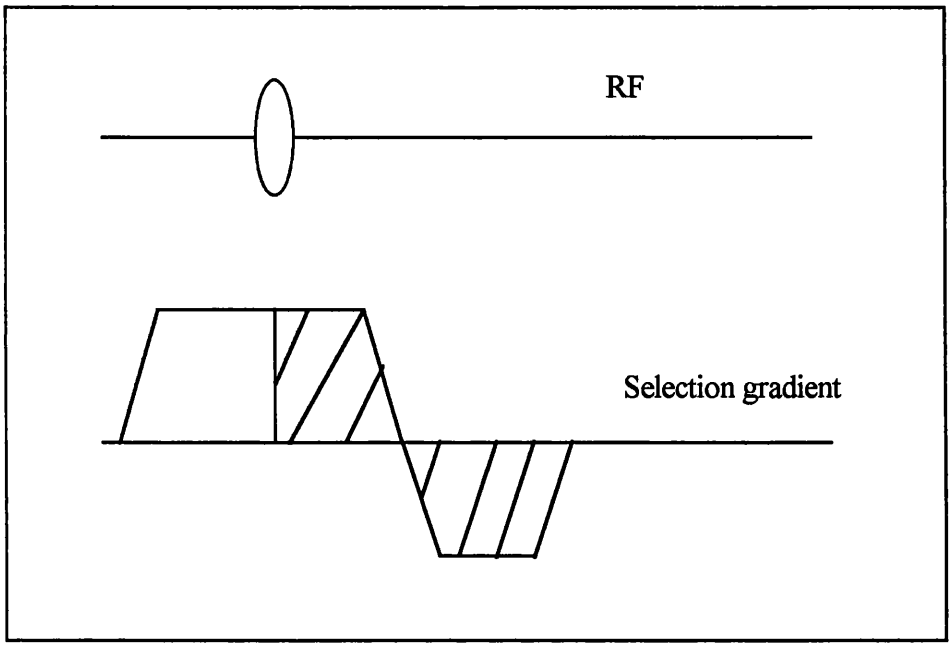

Fig 4.3 : *Slice refocusing gradient follows the selection gradient and optimizes the signal obtained.*

In many cases there is a certain delay between each excitation of a particular slice while we wait for the magnetization to recover, i.e. a relatively long repetition time, TR. This makes MRI a rather slow imaging technique. One way to speed up imaging is to make the most efficient use of this time. By offsetting the frequency of the RF pulse we can excite a number of different slices in each TR. After the first slice has been excited, another one at a different position along the gradient is selected, resulting in data from a parallel, offset slice. This procedure can be repeated to produce a series of slices, the number of which can be calculated by dividing the recovery interval by the time required for each slice. Providing there is no overlap between the slices, each slice is totally independent of the other.

4.3 Whole Imaging Experiments.

The most commonly used imaging sequence is the 2D Fourier (or spin- Warp) (Edelstein et al 1980) sequence in which a constant time interval for phase encoding is used, and the variation is achieved through the use of variable amplitude field gradient (Fig.4.4).

4.3.1 2D Fourier Imaging.

In a 2D Fourier Imaging Experiment the slice is defined by applying a shaped RF pulse in the presence of a selection gradient (SL) in the first interval. In the second interval of the sequence the slice rephase (SLR), the phase encoding (PE) and the read dephase (RD) gradient are applied simultaneously.

The frequency encoding gradient (RE) is switched on at the start of the third interval and observation of the signal can begin once the gradient has stabilized. The sampling period and read dephase gradient are usually chosen such that the gradient echo occurs in the middle of the sampling period. The resolution in the frequency encoding direction (NF) is determined by the number of points acquired during the sampling period (TAQ). The resolution in the phase encoding direction (NP) is determined by the number of steps corresponding to one repetition, while increasing the resolution in this direction increases the scan time, increasing the resolution in the frequency direction does not increase the scan time since we can simply extend the TAQ period. The resulting raw data consists of a matrix of NF.NP points (both of which are required to be powers of two for the Fourier Transform) and this is converted into an image by applying a 2D Fourier Transform.

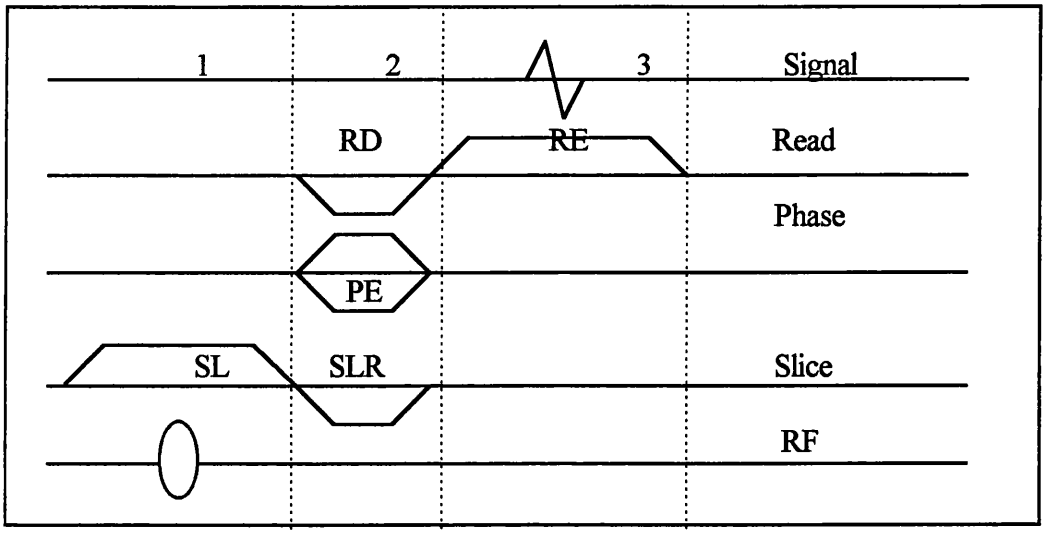

Fig. 4.4: *2D spin warp imaging sequence. Where: (SL) is the selection gradient; (SLR) the slice rephase; (PE) the phase encoding; (RD) the read dephase; and (RE) is the frequency encoding gradient.*

After the FT is complete the data will consist of real (R) and imaginary (I) signals for each pixel or picture element. Ideally all the data would be contained in the real image but imperfection in the magnetic resonance imager and in-vivo effects such as flow artifact cause the signal to be distributed between the two images. Normally a magnitude image is calculated from these two.

4.3.2. Pulse Sequences for Imaging.

Having considered how we can encode spatial information we can now consider how we can manipulate the form of the signal itself. The form of the magnetic resonance

signal is determined by a large number of factors including Proton Density (ρ), T_1, T_2, Flow and Diffusion.

By suitable preparation of the spins we can emphasise the contribution of one or more of these factors. The pulse sequences Saturation Recovery, Spin Echo and Stimulated Echo were discussed in chapter 3, and their signal and contrast behaviour will be considered in detail in the following chapters 5, 6 and 7.

CHAPTER (5)

5. Measurement of T_1-relaxation times of rat brain tissue at high field (7T-300 MHz)

5.1. Introduction.

Everybody involved in medical imaging shares one common dream which is to be able to distinguish the structures of the object under study with such sharpness and accuracy that analysis can be made with no room for speculation. Definition of normal anatomy and pathological changes should be easy and exact. This means that, for medical use, high contrast is a pre-requisite for a good imaging method.

This chapter will define the contrast and consider the factors affecting the image contrast in MRI. Experimental results of measurement of the T_1 relaxation time, of Sprague Dawley rat's brain using a 7T scanner will be introduced. Post mortem studies will be compared with the results from live animals collected using the same system and technique in an attempt to assess the myelination in specific areas of the rat brain.

5.2. Definition of contrast.

According to the American College of Radiology (Rinck 1990), contrast can be defined as the relative difference of the signal intensities in two adjacent regions. If the two intensities are I_a and I_b, a useful quantitative definition of contrast (C) can be given by the following equation:

$$C = (I_a - I_b)/(I_a + I_b) \qquad (5.1)$$

Digitization of images in nuclear medicine and X-ray computed tomography opened the door to more straight forward quantitative approaches to contrast. Now,

volume elements (voxels), or picture elements (pixels), are available. Their gray scale intensities can be expressed in numbers. The numerical difference between two intensities creates contrast. If there is no difference between two neighbouring pixels, they can not be distinguished and thus no contrast exists. The bigger the difference in the intensity of two pixels, the better the contrast will be.

Relating image contrast to object contrast is more difficult in magnetic resonance imaging than in conventional radiography, as there are more object parameters affecting the final image and their relative contributions are very dependent on the particular imaging technique used.

The primary obstacle in the detection of contrast is the image noise which is divided into two main categories namely

1) Statistical or random noise which reflects the pixel to pixel variation in signal intensities caused primarily by the receiver electronics at very low magnetic field strengths or eddy currents set up in the sample (patient) at high field strengths.This type of noise is independent of the pulse sequence used or the inter pulse delay time selected by the user. Statistical noise can be minimised relative to the signal by increasing the voxel volume (slice thickness or in-plane pixel size), by increasing the number of acquisitions in the phase encoding direction or by decreasing the bandwidth, thereby narrowing the range of frequencies over which noise can be recorded.

2) Systematic or structured noise is non random signal variation that arises from a number of possible sources such as motion artifact originating from patient movements, respiration and cardiac motion. This type of noise is dependent on inter pulse delay times

in spin echo pulse sequences. Therefore manipulating TR and TE may reduce the effect of this noise and gating of the cardic and respiratory motion will considerably improve these effects.

Alternatively signal averaging may improve the signal to noise ratio for both statistical and systematic noise effects on the image.

5.3. Contrast Factors.

As mentioned above MRI possesses far more contrast influencing factors than other imaging methods. Contrast in conventional radiograph and computed tomography images is essentially based on small density differences and can only be changed by adding contrast agents such as barium and iodinated substances which influence electron density within a certain organ. Contrast behaviour in MRI is more complex because it is influenced by numerous factors which can be divided into two groups, namely the intrinsic and extrinsic parameters. Table 5.1 gives an overview of the most important of these parameters.

Many of the extrinsic factors can manipulate the intrinsic factors. For the clinical application of MRI it is necessary to be aware of all their influences and interactions if one is to react rapidly and efficiently to a given diagnostic question.

One of the main advantages of MRI is the possibility to change contrast by choosing special pulse sequences and pulse sequence parameters. By emphasizing one factor or mixing several factors in a specific way the contrast behaviour of a certain morphologic region or pathological lesion can be highlighted. Comparison of two images of the same object taken with two different imaging systems with different field strengths

Table 5.1: *Contrast parameters in magnetic resonance imaging*

Intrinsic	Extrinsic	
1. Proton Density	1. Field Strength	3. Radiofrequency Sequences
2. T_1 - Relaxation	2. Hard- and Software Parameters	• Saturation Recovery
3. T_2 - Relaxation	• Number of Slices	• Inversion Recovery
4. Chemical Shift	• Slice Thickness and Gaps	• Spin Echo
5. Perfusion	• Slice Orientation	• Fast Sequences
6. Diffusion	• Number of Averages	4. Pulse Sequence Parameters
7. Bulk Flow	• Pulse Shape	• Repetition Time
8. Temperature	• Pixel Size/Field of View	• Echo Time
	• Acquisition Mode (2D/3D)	• Inversion Time
	• Artifact Suppression	• Flip Angle
		5. Contrast Changing Agents

apparently but otherwise using the same pulse parameters can often reveal different contrast patterns (Rink 1990). Three main tissue properties governing contrast in MRI may be distinguished. First, the Spin- Lattice and Spin-Spin MR-relaxation characterized by the T_1 and T_2 time value (sec.3.7.1&2).

The second important factor is the relative number of hydrogen nuclei (Protons) present in the tissue, the Proton Density ρ. Finally image contrast is influenced by motion e.g flow and diffusion.

Among the extrinsic technical factors which influence tissue contrast is the method of examination. In this study we only consider the Double Echo sequence which is essentially a Spin Echo (SE) sequence (sec. 2.8.3) with only two echoes. This is because this sequence can be manipulated to measure all three parameters T_1, T_2 and ρ as follows; The intensity (I) of a pixel in an image obtained via the SE method is approximately described by the following equation (McManus and Bartlet 1986)

$$I_{SE} = K * \rho [1- \exp (-TR/T_1)] * \exp (-TE/T_2) \qquad (5.2)$$

where K represents the influence of flow, perfusion and diffusion. Most soft tissue contains 80-90% water , i.e the proton densities are only slightly differing, therefore the ratio TR/T_1 and TE/T_2 are the contrast dominating factors in these tissues.

For the sake of simplicity, we can reduce equation 5.2 to

$$I = K * \rho [A * B] \qquad (5.3)$$

where $A = (1- \exp (-TR/T_1)$ and $B = \exp (-TE/T_2)$

Applying a SE sequence with a short TR and short TE will roughly cause factor B of equation 5.3 to equal one and hence the observed intensities will be predominantly a function of tissue T_1 values. On the other hand if a SE sequence with a long TR and long TE is used, the value of the factor A in equation 5.3 approaches unity and the image intensity will merely be dependent on T_2 values. Application of intermediate TR and TE values will give rise to images in which signal intensity is determined by both T_1 and T_2

differences between the tissues. Image obtained with very long TR and very short TE exhibit minimal influence of T_1 and T_2 relaxations on the image appearance and are hence called proton density images. In these latter images the proton density is the principle contrast determining factor.

5.4 Method of Experiment.

MR Images data were collected from 20 Sprague Dawley (S/D) rats. Ten of them were examined post mortem, the images being obtained 1-2 hours following death. All the rats were mature, aged between 3-6 months and weighed between 300-500 g. (mean 401, SD ±102). The rats used in the live studies were anaesthetized using intraperitoneal Urethane at 36% (4 ml/kg), then following cannulation of a neck vein, further Urethane (24%) was added intravenously as necessary to maintain anaesthesia. Animals were positioned in a holder which was designed and built specially for this purpose (see sec. 6.2.2). The head of the animal is held fixed in an exact position to meet the centre of the magnet. The whole assembly is then fitted into a 10 cm diameter RF probe which fits into the unshielded gradient coils in the magnet bore. ECG and temperature were monitored continuously. Animals were kept warm through the experiments by adjustable hot air blown through the holder.

Images were obtained with a superconducting magnet operating at 7T (Bruker), with a ^1H resonant frequency of approximately 300 MHz. The images were acquired with use of a 256×256 matrix, at 6 cm field of view. The system is provided with a 50 mT/m unshielded gradient coils set and a standard 10 cm birdcage RF probe. Slice thickness was 4mm. (only one slice is employed). All slices were Axial at the level of the basal ganglia.

Five regions of interest were chosen as shown in Fig 5.1. Four square regions, (each 16 (4*4) pixels in area) were selected. Two of them (regions 1 and 2 in fig. 5.1) were positioned in the corpus callosum of the cerebral hemispheres. This area is expected to be rich in myelin as it contains mostly the myelinated axons of the neuron cells (white matter). This is in contrast to the gray matter around the surface of the brain (regions 3 and 4 in fig. 5.1) which contains mainly the neurocell's body and is believed to be a largely myelin free area. Region five which is rectangular (16 (8*2) pixels in area). is located across the cerebellum as this area is one of the first to be myelinated during the early stages of life and therefore is expected to be most useful in our future follow up studies.

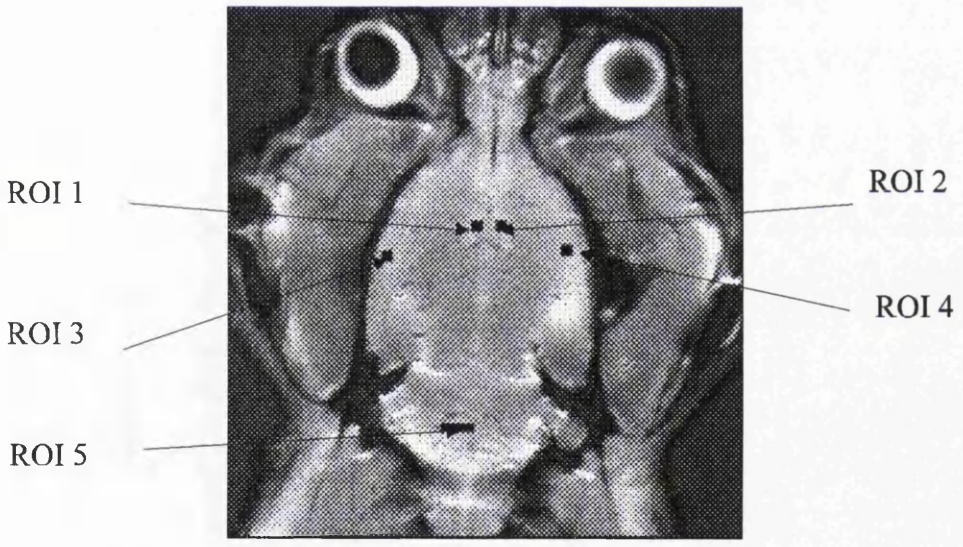

Fig. 5.1: *Axial slice across the rat brain showing the five regions of interest (ROI 1-5)*

T_1 was measured for each region using a Double Echo pulse sequence. Data was collected at repetition times TR ranging from 3000-300 msec in 300 msec steps (a total of 10 steps).

The echo time TE was kept fixed throughout the experiment at 33 msec. For each region studied, the relative intensity was plotted against the repetition time. The experimental data was fit to the theoretical equation (equ. 5.2) for signal intensity in a Spin Echo imaging pulse sequence.

The curve fit was performed using Sigmaplot software. The results of this study are shown in Fig.5.2. for ROI1 in one of the rats as an example.

Fig 5.2: *The fitting of T_1 curve using Sigma plot software.*

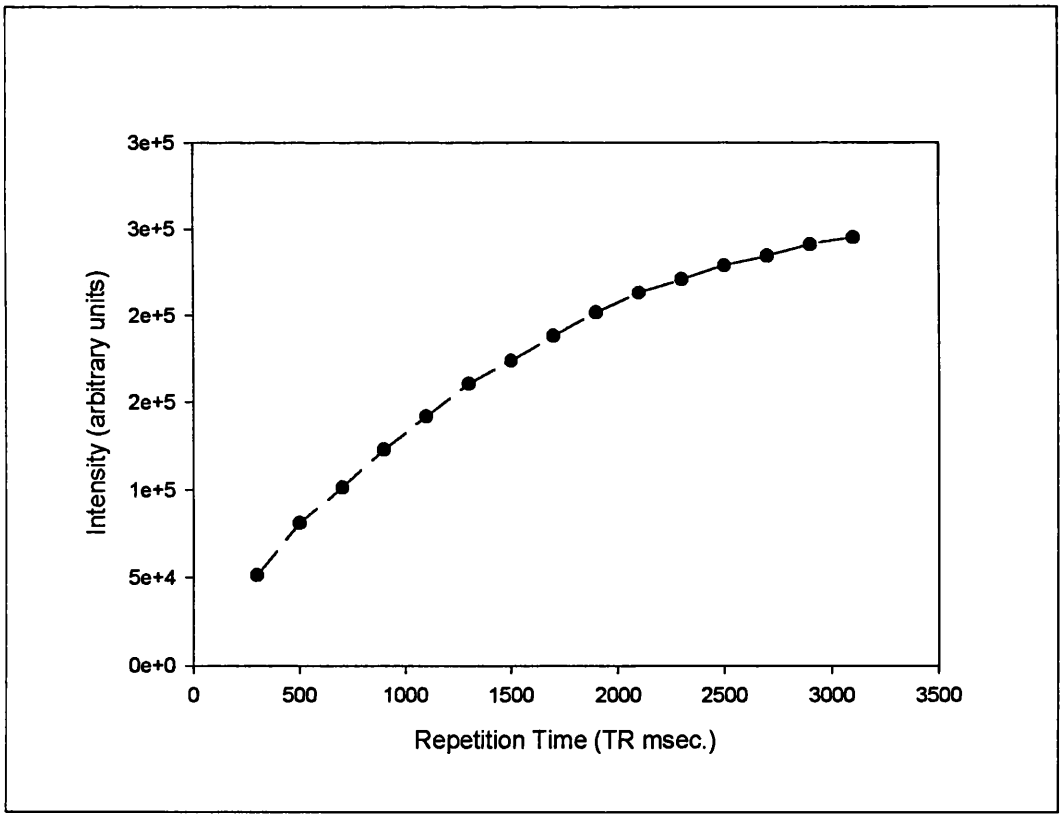

The pulse sequence used (DECH) has been tested on a reference phantom (10 mM Copper Sulphate - $CuSO_4$ - in distilled water) for measuring T_1, and also a Multiple

Slice Variable Echo (MSVE) pulse sequence has been used for measuring T_2 in the same phantom. The values of T_1 and T_2 were compared to the results of measuring these relaxation times on the same sample using a non-localized Carr Purcell Meiboom Gill (CPMG) pulse sequence for measuring T_2 and an IR pulse sequence (IR18) for the measurement of T_1 (John Thornton, UCL - personal communication). Results of this study are shown in table 5.2.

Pulse Seq.	T_1 msec	T_2 msec	± SD
DECH	133.5	-	± 9.5
IR18	131.5	-	± 3.9
MSVE	-	123.9	± 1.5
CPMG	-	126.4	± 2.6

Table 5.2 T_1 & T_2 measurements for a 10 mM $CuSO_4$ solution.

In this table the values for T_2 obtained with the Short T_2 Variable Echo (STVE) pulse sequence, which was specifically developed specially for this study, and CPMG sequences are in good agreement, also the phantom T_1 values obtained with the DECH and IR18 sequences were consistent. The Saturation Recovery pulse sequence (SR), which has also been shown to be suitable for the measurement of T_1 (Rink 1990), has been avoided in this study for two main reasons. Firstly, to avoid the Free Precession Steady State (FPSS) situation for which a repetition time of at least five times the expected T_1 (around 2 sec) has to be employed which will cause the imaging time to be impractically

long. Secondly, the selective 90°RF pulse has to be exact each time otherwise the signal will be affected.(Young *et al* 1985). However, the results in table 5.2 suggest that the pulse sequences used in this study were suitable for quantitative in-vivo evaluation of relaxation processes by MRI. The system was also checked by measuring T_1 and T_2 relaxation times of a phantom with known values (H_2O) at room temprature (21 °C) . The results were : T_1 = 2.849 sec ±25 ms (IR18) ; T_2 = 1.334 sec ±60 ms (CPMG).

5.5 Results

The mean T_1 value of the post mortem study is shown in table 5.3. This data was statistically analysed using SigmaStat statistical software (version 2). A one way Analysis Of Variance (ANOVA), which is a parametric test to compare two or more different

Table 5.3 : *Post Mortem T_1 measurements for S/D rat brain using 7T (300MHz) Double Echo Pulse Sequence (DECH).*

EXP. NO.	ROI NO.1	ROI NO.2	ROI NO.3	ROI NO.4	ROI NO.5
1 T_1 ms ±SD	1571 ±70.8	1618 ±45.7	1516 ±94.2	1538 ±61.1	1663 ±177.5
2 T_1 ms ±SD	1532 ±55.4	1572 ±46.7	1500 ±68.7	1513 ±100.4	1582 ±185.6
3 T_1 ms ±SD	1555 ±125.4	1580 ±110.6	1356 ±160.5	1322 ±157.9	1360 ±197.2
4 T_1ms ±SD	1469 ±118.6	1354 ±156	1515 ±89.1	1498 ±139.4	1395 ±178
5 T_1 ms ±SD	1452 ±115.1	1445 ±107.3	1496 ±156.0	1451 ±98.6	1575 ±165.2
6 T_1ms ±SD	1825 ±121.7	1857 ±147.5	1724 ±134.6	1652 ±176	1715 ±210.3
7 T_1ms ±SD	1583 ±144.3	1586 ±133.8	1619 ±110	1668 ±125.1	1780 ±190.0
8 T_1ms ±SD	1412 ±126.3	1448 ±127.1	1381 ±141	1419 ±146.5	1550 ±187.4
9 T_1ms ±SD	1381 ±94.9	1471 ±134.9	1416 ±139.3	1449 ±135.8	1536 ±169.6
10 T_1ms ±SD	1374 ±140.5	1424 ±146.6	1392 ±142.6	1480 ±124.9	1626 ±184.2
Mean ±SD	1515.4 ± 111.3	1535.5 ± 115.6	1491.5 ± 123.6	1499.0 ± 126.6	1578.2 ± 184.5

experimental groups, was performed to see if the mean values in the five selected ROIs were statistically different.The results of this study are summarised as follows:

T_1 mean values together with the standard deviations for post mortem animals are summarised in table 5.4.

Table 5.4: *Results of T_1 mean values and S/D for post mortem animals.*

Regions	Mean ms.	Std Dev ms
ROI 1	1515.400	± 111.3
ROI 2	1535.500	± 115.7
ROI 3	1491.500	± 123.6
ROI 4	1499.000	± 126.5
ROI 5	1578.200	± 184.5

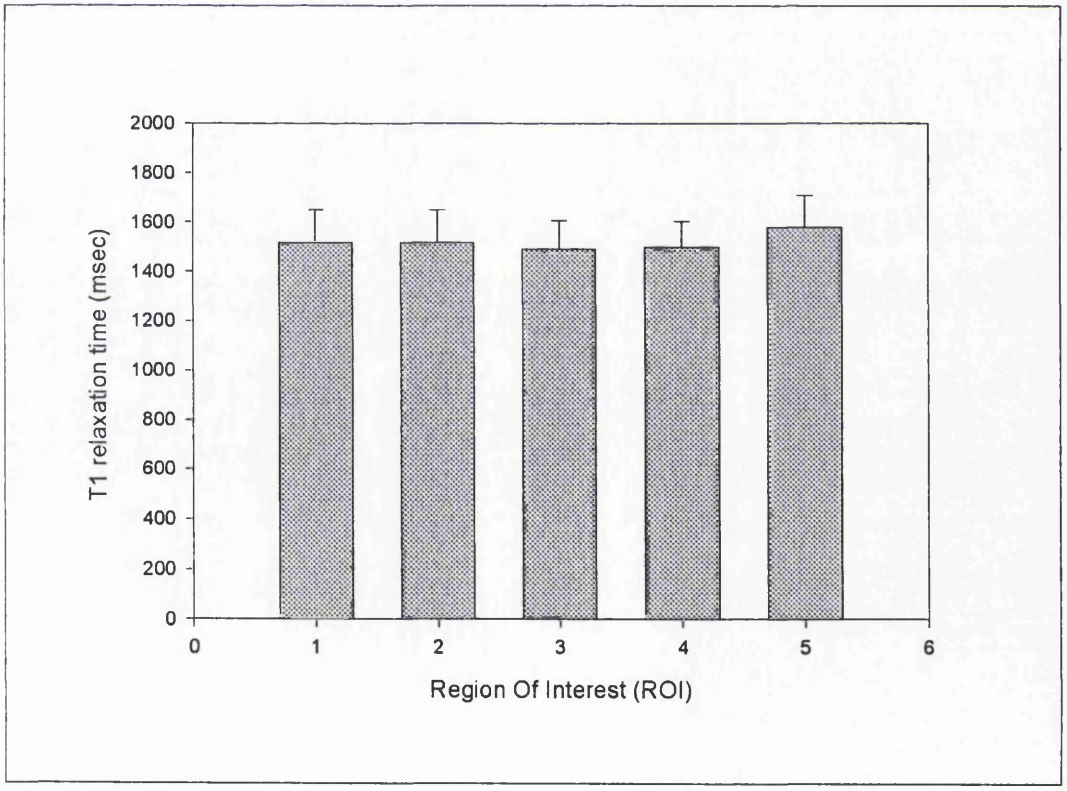

Fig. 5.3: *Results of T_1 relaxation time for post mortem S/D animals at 7T.*

The above results suggest that the differences in the mean values among the five ROIs for the post mortem animals are not great enough to exclude the possibility that the difference is due to random sampling variability and therefore we conclude that there is not a statistically significant difference ($p > 0.480$). This result can be observed clearly from the bar chart of the post mortem results Fig.5.3.

In Table 5.5 we have the results of the live animals study. The same data analysis procedure described above was performed to analyse the live animals data and the results are listed below.

Table 5.5: *Results of T_1 measurements for live S/D rat brain using 7T (300MHz) Double Echo Pulse Sequence (DECH).*

EXP. NO.	ROI1	ROI2	ROI3	ROI4	ROI5
1 T_1 ms±SD	1518 ±96.1	1463 ±48.8	1766 ±93.5	1528 ±95.7	1758 ±134.6
2 T_1ms ±SD	1843 ±59.7	1914 ±41.3	1826 ±78.1	1902 ±61.3	1833 ±145.2
3 T_1ms±SD	1751 ±69.7	1767 ±105.4	1516 ±100.3	1674 ±88.1	1488 ±160.2
4 T_1ms±SD	1877 ±151	1887 ±106	2052 ±70.2	2071 ±120	2114 ±159.8
5 T_1ms±SD	1873 ±154	1931 ±176	1912 ±187	1898 ±79.8	1886 ±196.5
6 T_1ms±SD	1848 ±80.6	1750 ±90.1	1845 ±107.6	1825 ±84.5	2127 ±207.9
7 T_1ms±SD	1996 ±73.9	1972 ±72.5	1934 ±59.5	1777 ±54.7	2026 ±198.9
8 T_1ms±SD	1759 ±55.9	1721 ±116.5	1698 ±127	1670 ±97.4	1708 ±178.4
9 T_1ms±SD	1570 ±57.2	1637 ±32.6	1599 ±44.8	1599 ±92.1	1734 ±112.7
10T_1ms ±SD	1645 ±116	1687 ±92.6	1698 ±111.5	1659 ±64.5	1637 ±98.4
Mean (ms) ±SD	1768.4 ±91.4	1772.9 ±88.2	1784.6 ±97.9	1760.3 ±83.8	1831.1 ±139.4

Table 5.6: *Results of T_1 mean value and S/D for live animals*

Region	Mean ms.	Std Dev
ROI 1	1768.400	±91.4
ROI 2	1772.900	±88.2
ROI 3	1784.600	±97.9
ROI 4	1760.300	±83.8
ROI 5	1831.100	±139.4

A summary of T_1 values together with the standard deviation for the live animals are shown in table 5.6. Again we have found that the differences in the mean values among the ROIs selected in the live animals are not great enough to exclude the possibility that the difference is due to random sampling variability and there is no statistically significant difference ($p > 0.855$) as can be seen from the bar chart for the live animals Fig. 5.4.

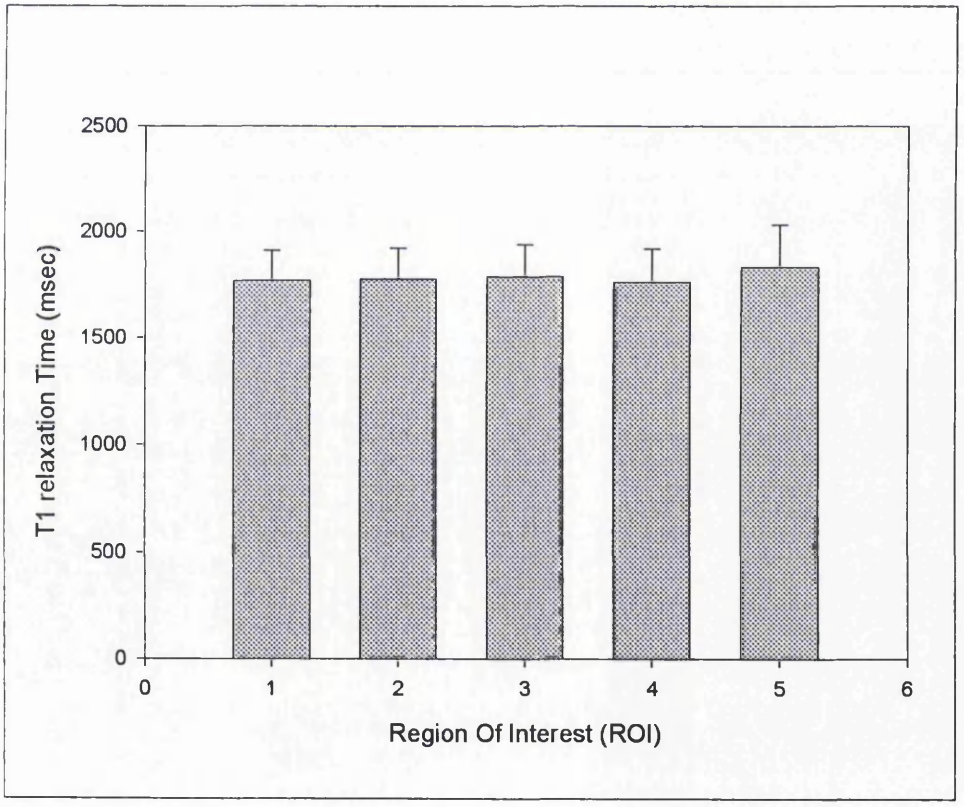

Fig.5.4: *Results of T_1 relaxation for the five regions in the live animals.*

5.6 Discussion and Summary

In this part of the study for measuring the T_1 relaxation times of the rat brain at 7T, the results shown in tables 5.4 and 5.6 were compared with the data obtained from similar studies at lower field strengths. According to the literature (Bottomley et al 1984), values of T_1 can be extrapolated using the expression

$$T_1 = A\, v^B \pm SD$$

Where T_1 is in sec., v is the frequency in Hz and the SD is expressed as a percentage of T_1. A & B are tissue dependent fitting constants.

T_1 values extrapolated to 300 MHz for the rat brain by using the above expression (Bottomley et al 1984) were 1529.9 ms ±290.6 which are comparable to the results from our study for post mortem animals shown in tables 5.4.

Inaccuracies caused by partial volume effects are not likely to contribute much to the relaxation time images as these effects were minimized by choosing a rather thin imaging slice and by careful selection of the ROIs used for evaluation. There is however a systematic error which will have affected the T_1 relaxation values, which is of the slice profile effect when the investigations are carried out with a repetition times less than five times the expected T_1 (Young *et al* 1985). As all our data were collected with a TR of 3 second maximum we should therefore, expect. the slice profile to be affected as it is strongly dependent on T_1 and the repetition rate TR (Young *et al* 1985). In addition, magnetic resonance imaging data accuracy and precision in measuring relaxation times will always be affected by the following (Johnson *et al* 1987):

(i) Image noise which is always present and will introduce inevitable imprecision in relaxation time measurements.

(ii) Image non-uniformity which will cause imprecision if the measured volume of tissue is not always in the same place in the image system.

(iii) There are also some other sources of relaxation variance reported by Harvey *et al* 1991. These include the re-scanning reproducibility, sample repositioning, machine drift and anatomical position such as left and right hemisphere asymmetry, and biological variability.

Region 5 in both results shows a slight difference in T_1 value and this is most probably due to the contamination of this particular region with CSF as it was sited across the cerebellum as shown in Fig. 5.1. There were no significant difference between regions 1 and 2 nor between regions 3 and 4 when comparing the regions on the opposite sides of the cerebral hemisphere within the same animal.

Results of T_1 in post mortem tissue (mean 1523.8 $\pm$ 132.3 SD) have a significantly different value than those obtained from live animals (mean 1783.5 $\pm$ 100 SD) ($p < 0.01$), as shown in tables 5.4 & 5.6. In a quantitative investigation reported by Barroilhet *et al* (1975) it was concluded that in general, relaxation times are strongly temperature dependent. As the relaxation times in this study were measured at a room temperature of approximately 23°C for post mortem and a physiological temperature of 38°C for live animals, we would expect this effect to be the main reason for the elevation of T_1 values in the case of live animals.

Magnetic field dependence of tissue spin- lattice and spin-spin relaxation times (T_1,T_2) has also been measured by a number of investigators, (Chen *et al* 1992.), the experiments involving field strengths ranging from 0.02-4.85T. The feasibility of high field > 4.85T imaging is an important issue for MR microscopists since it has long been recognized that an increase in magnetic field strength affords a greater SNR. Lower field measurements suggest the convergence of tissue T_1 values to that of water at very high fields, (Hoult *et al* 1986). If the T_1 difference between adjacent tissues becomes small at these higher field strength, the resulting image might not allow differentiation between tissue types. In a clinical environment it is generally T_1 and T_2 that determine image contrast. Thus, the dependence of T_1 and T_2 on field will impact significantly on the ability to image at high field.

From these result one can conclude that the T_1 method for assessing the myelination in a neural tissue will not be useful in the 7T magnetic field strength system. This is seen by comparing different regions for white matter areas of the brain (e.g. regions 1 and 2 in Fig. 5.1) and gray matter areas (regions 3 and 4 in Fig. 5.1) The explanation for this conclusion together with the reason for the slight difference in the value of T_1 - relaxation time between live and post mortem animals, which is mainly due to the temperature difference between the two groups will be discussed in more detail in chapter eight.

CHAPTER (6)

6.1 In-vitro T_2 determination for rat brain tissue in low and high fields

6.1.1 Introduction

Magnetic resonance spin-spin relaxation times of brain tissue provide useful information in distinguishing tissue regions of different cell composition. The cortical white matter, for example, contains myelinated neuroaxons and is expected to have a shorter T_2 values when compared with the cortical gray matter. The white matter will therefore, appear to have a darker or brighter contrast in magnetic resonance imaging depending on the imaging method or the pulse sequence used (Rinck et al 1990).

The aim of this study was to measure T_2 relaxation time for excised rat brain tissue at different magnetic field strengths using different measuring techniques in order to demonstrate that quantitative MR can be used to distinguish the different type of tissues.

6.1.2. Method of experiment.

Five adult female (Ex-Breeder) Sprague Dawley rats (300-400 g) were sacrificed by asphyxiation using a gas chamber (CO_2). The whole brain was rapidly removed and placed, carefully (to keep it intact), in the bottom of a 30 mm o.d and 50 mm long plastic bottle. The bottle was sealed using a plaster tape and positioned in a holder, the whole assembly was then placed in the magnet bore ready for imaging within one hour of the animal's death.

Spin-Spin relaxation time T_2 was determined first on a Bruker Biospec superconducting magnet operating at 7T, with a ^1H resonant frequency of 300 MHz. The images were acquired with use of a 128 X 256 matrix, at 6 cm field of view. The system is

provided with a 50 mT/m unshielded gradient coil set and a standard 10 cm birdcage rf probe. Data were collected from two regions of interest of an axial slice at the level of the basal ganglia. Each ROI was 16 (4*4) pixels in area and was placed in the corpus callosum on both sides of the cerebral hemisphere (see Fig. 5.1).

The pulse sequence used for imaging was a Multi Slice Variable Echo (MSVE), but only the first slice and first echo were used in the analysis with different echo times ranging from 30 msec to 80 msec in 10 msec steps totalling six steps Fig. 6.1. Repetition time was kept at 3 sec. Data were collected at room temperature (approx. 22°C). For each region studied the relative intensity was plotted against the time. The experimental data were fit to the following non-linear theoretical expression

$$f(t) = M * \exp(-TE/T2) \qquad (6.1)$$

The curve fit was performed using Sigmaplot software.

The second method for determining T2 relaxation time for the same samples was carried out in a Bruker IBM PC/20 series NMR analyzer (Minispec) operating at 0.47 T (a permanent magnet), with ^1H resonant frequency of 20 MHz.

The sample was removed from the plastic bottle. The cerebral hemispheres were separated along the midline and rapidly inserted into a 10 mm outer diameter 150 mm long NMR tube. The tube was then inserted into the probehead through the sample insertion funnel on the top of the minispec unit. Data were collected at the standard minispec magnet temperature, 40°C. The pulse sequence used for T_2 measurement in the Minispec was the Carr Parcel Meiboom Gill (CPMG). The data were fit to the linear logarithmic function

$$\ln f(t) = \ln M - TE/T_2 \qquad (6.2)$$

The fit was performed using the monoexponential fit routine supplied by the "Experiment Supervisor" software which is a linear regression fit on the log of the measured points.

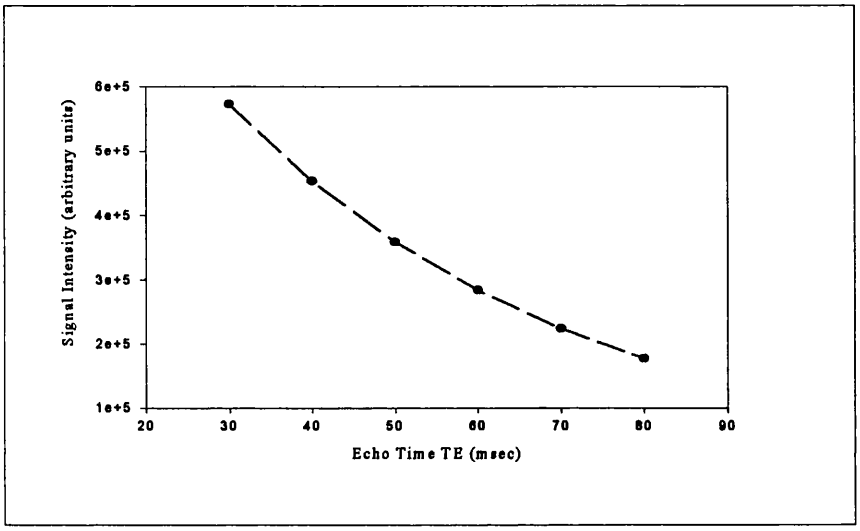

Fig 6.1: T_2 relaxation curve fit for region 3 of Fig.6.4 for S/D rat brain.

A more sophisticated routine also supplied by the "Experiment Supervisor" software was also used to try a biexponential fit to determine if there were any measurable short and long components of a T_2 relaxation time in the brain. Data in this case was fit to the biexponential expression

$$f(t) = M_a \exp(-TE_{long}/T_{2a}) + M_b \exp(-TE_{short}/T_{2b}) \qquad (6.3)$$

Echo times ranged from 5 msec to 100 msec and the number of data points was 20.

6.1.3. Results

The summary of the 7T study is shown in Fig 6.2. In this figure we have a mean T_2 value of 40.2 ms with an SD of ± 2.24 ms for region ROI1 and 39.9 ± 2.15 for region ROI2 which correspond to regions 1 and 2 respectively in Fig. 5.1. The mean values of T_2 are obtained using a monoexponential fit to equation 6.1.

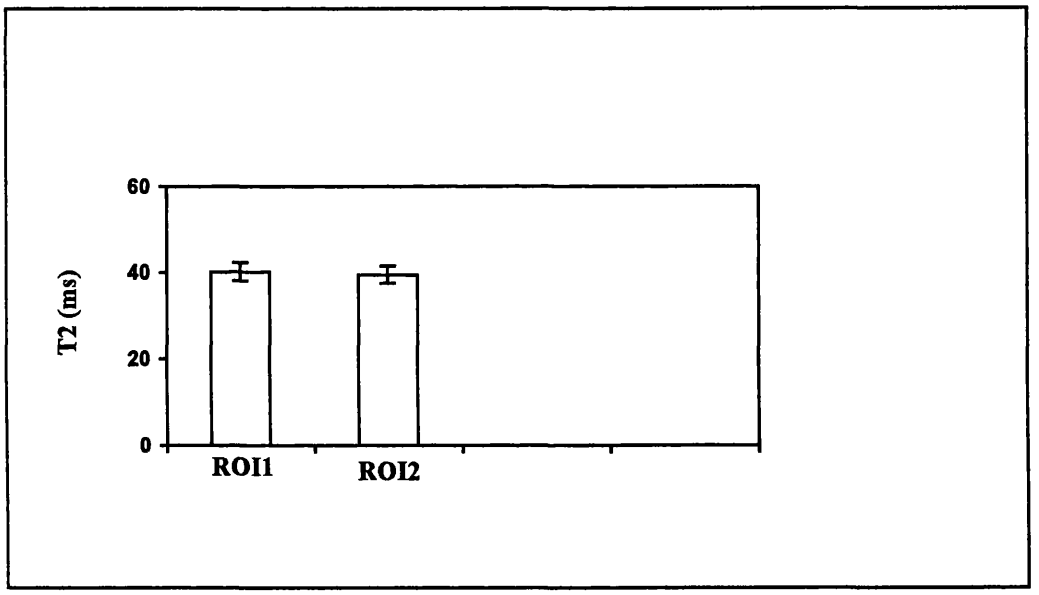

Fig. 6.2: In-vitro T_2 results at 7T for adult S/D rat for ROI1&2 (in fig.6.4)

(monoexponential fit. n=5)

The results from the minispec (0.47T) are shown in Fig. 6.3. These values were obtained by using the biexponential fit (equation 6.3) and they are 83.4 ±4.26 ms for T_{2long} (free water reservoir) and 14.4 ±5.86 for the $T_{2\,short}$ component (bound water reservoir) The results at the low field were found to be consistant with recent similar studies in the literature (MacKay *et al* 1994; Miot-Noirault *et al* 1996)

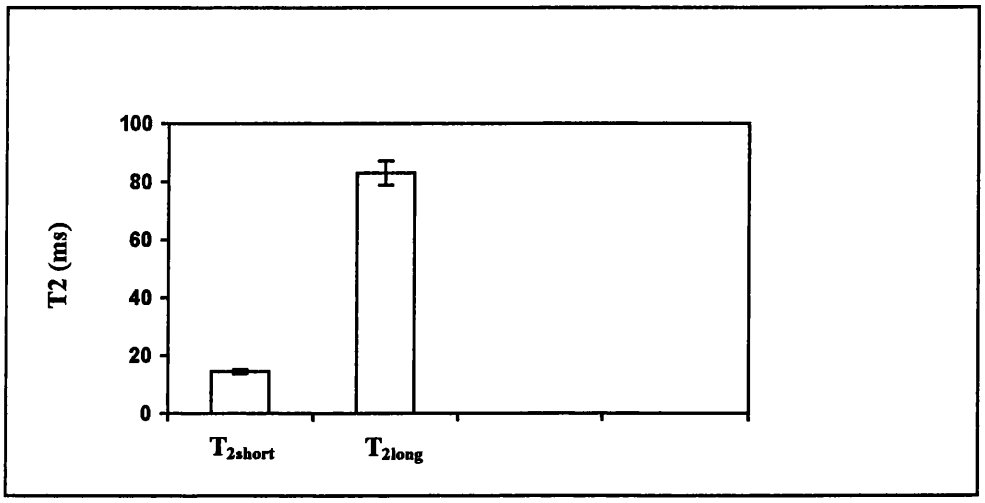

Fig. 6.3: *In-vitro T_2 results at 0.47T for the whole adult S/D rat brain (biexponential fit. n=5)*

6.1.4 Discussion and Summary

The above results summarised in Fig. 6.2 as a mean for five animals suggest that the T_2 relaxation value drops considerably at very high field strenth (7T) to 40.2 ms compared to 83.4 ms at low field (Fig. 6.3) for the same sample. This will effectively prevent the separation of the bound and free water reservoirs by using a biexponential fit.

In vitro T_2 relaxation time results obtained in the lower field part of this study (at 0.47T), which utilized undefined areas of cortex or whole brain, were compared with the results of similar in vitro studies by Besson *et al* in 1989 (T_2 = 77.7 ms ± 1.9 SD, rat brain) and recent in vivo studies at 1.5T by MacKay et al 1994 who claimed that they have observed a short T_2 myelin bound water component (T_2 between 10 - 55 msec, human

brain). It was found that the values reported in these studies and the outcome of our own studies were in good agreement.

The results obtained at 7T seem to be the only ones available and no similar data have been found so far, in the literature. Although the values we obtained for T_2 are low when compared with previous studies at low field (2.4T), Bottomley et al 1984 (T_2 = 76 msec, rat brain at 100 MHz.), they should be accurate as the system and the pulse sequence used for the study have been tested on a reference phantom of $MnCl_2$ (.05 mM). This test gave results for T_2 of 135 msec with an SD of ± 13.74 msec which is consistent with the previous data collected on this calibration solution using a CPMG sequence.

6.2 In-vivo T_2 determination for rat brain tissue at high field (7T) as a function of gestational age

6.2.1 Introduction

In the beginning of this chapter we have referred to the importance of the spin-spin relaxation time in distingishing tissue regions of different cell composition. To our knowledge, previous regional analysis of the rat brain has either relied on the examination of postmortem tissue or been carried at a low field strength < 7T. Besides the fact that the relaxation times are strongly field dependent the monitoring of the myelination process needs a living rat brain to study. So far no such studies have been found on the literature.

The purpose of this study was to extend the measurement described at the beginning of this chapter to determine T_2 in vivo in order to examine the feasibility of very high field imaging and to observe the age dependence of rat brain T_2 at 300 MHz (7T).

6.2.2. Method of Experiment.

MR image data were collected from 24 Sprague Dawley (S/D) rats. Six of them were 7-days old and weighed between 15.1-19.5 g (17.2 mean, SD ± 2.2 g), six were 10 days weighed between 22.7-24.5 g (23.6 mean, SD ± 1.8 g), six 14 days weighed between 27.9-29.8 g (28.85 mean, SD 1.9 g) and the rest were mature, aged 3-6 month and weighed between 320-355 g (331.7 mean, SD ± 18.6). The 7, 10 and 14 day old rats were anaesthetized by inhalation using Isoflurane at 4.5% with a 50:50 Air/O_2 flow of 2 l/min during induction. Anaesthesia was then maintained by 1.0% - 1.5% of Isoflurane with the same amount of Air/O_2. Mature animals were anaesthetized differently using intraperitoneal Urethane at 36% (4ml/kg), then following cannulation of a neck vein, further Urethane (24%) was added intravenously as necessary to maintain anaesthesia.

Although, images of all animals were obtained with the same superconducting magnet operating at 7T (Bruker) with a ^1H resonant frequency of 300 MHz, different RF coils and gradient sets were used in order to obtain the same resolution in both cases and maintain a high S/N ratio. Mature animals were positioned in a holder which was designed and built specially for this purpose. It is made from a perspex cylinder of 9cm diameter and 60cm long. The head of the animal is held fixed in an exact position inside the cylinder by a specially designed nonmetallic stereotaxic frame. This consists of a plastic mouth piece connected to an adjustable rod, and two ceramic points which then engage into the back of the skull to prevent any movements . The whole assembly is fitted into a 10cm diameter birdcage RF probe which fits into the unshielded gradient coil in the magnet bore. The RF probe used for the 7-days animals was a saddle coil of 2.6cm diameter inductively matched to 50Ω RF cable and tuned to the ^1H resonant frequency of 300Mhz

via a parallel capacitor. This coil was also designed and built specially for this study by Dr. M. Clemence (UCL N.M.R. group). The probe is mounted in a perspex holder of 11.5 cm diameter to fit into the unshielded gradient provided by the system manufacturer. Mature animals were kept warm through the experiments by an adjustable hot air flow through the holder, while the 7-days old animals were covered with a foam blanket to keep them warm. ECG and rectal temperature were monitored continuously for mature animals and for the 7-days animals only the surface (abdominal) body temperature was recorded.

The images for the mature animals were acquired with use of a 256×256 matrix, at 6cm field of view, the slice thickness being 4mm. The field of view and slice thickness for the 7,10 and 14-days animals were 2.56cm and 1mm respectively with image matrix of 128x256. All slices were coronal through the pituitary gland. Four regions of interest (ROI) were chosen as shown in fig 6.4. The area of the regions, 16 pixels (4*4), were positioned equidistant in the two cerebral hemispheres. The two inner regions were expected to cover an area which is rich in myelin as it contains mostly the myelinated axons of the neural cells (white matter). This is in contrast to the two outer regions which cover the gray matter area around the surface of the brain and which are expected to contain mainly the neural cell bodies and is believed to be a largely myelin free area, (see Chapter 2).

Spin-Spin relaxation time T_2 was measured for each region in the six animals using a Short T_2 Variable Echo pulse sequence (STVE) which was developed specially for this study. The pulse is a modification of the Bruker Multi Slice Fixed Echo (ME08) sequence which is in turn a modification of the Multi Slice Multi Echo (MSME) sequence with a fixed echo time of 8ms. The new feature of the STVE pulse is that the echo time can be

varied from 10 msec. minimum to a few seconds, although in the protocol we have used in the current study this was limited to a maximum echo time of 100 msec. This modification was achieved by inserting an assignable delay of a minimum value of 1msec on both sides of the 180° RF pulse of the original Spin Echo pulse sequence (Fig.3.8). Data were collected for each region of interest with a fixed repetition time of 3 sec. and two different variable echo times. The first echo time varied from 10 msec to 28 msec with a 2 msec step to allow for the possible measurement of the very short T_2 component, while the

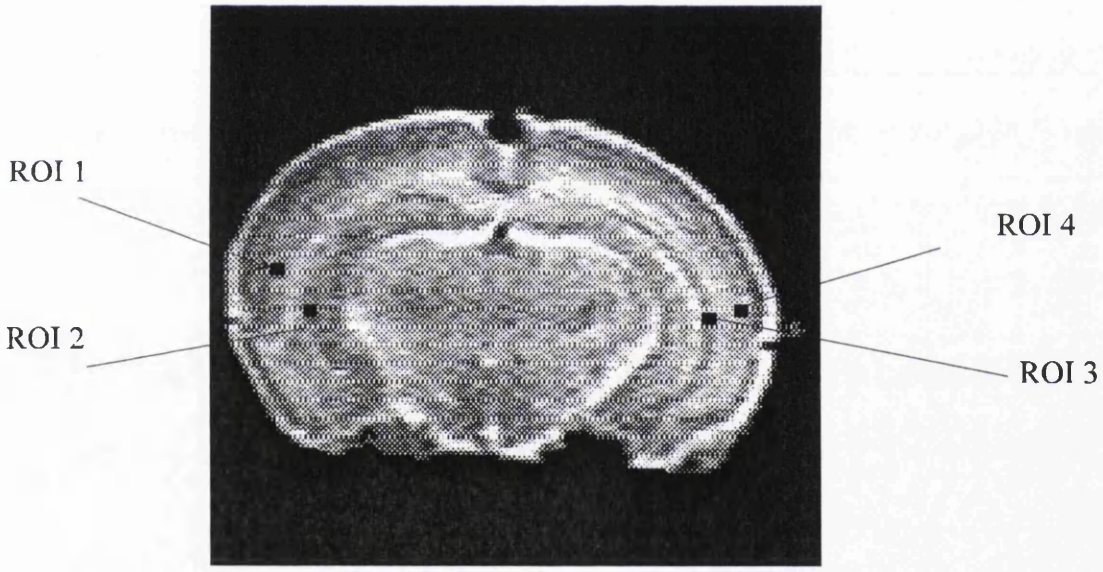

Fig. 6.4: *Coronal slice of the rat brain showing the four regions of interest.*

second echo time varied from 30 msec. to 100 msec with a 10 msec step to measure the short or medium T_2 component. The two sets of echo times, totalling 18 steps (data points) were fit to the following non-linear theoretical expression:

$$f(t) = M_a \exp(-TE_{short}/T_2) + M_b \exp(TE_{long}/T_2) \qquad (6.4)$$

The curve fit was then performed using Sigmaplot software.

Animal preparation took between 30-60 minutes and the data collection experiment lasted for approximately two hours per animal.

6.2.3. Results

There was no evidence of an observable separate very short T_2 component when the 7T data were fitted to expression 6.4. This may be due to the fact that the value for tissue T_2 reduces considerably at high fields and most probably it is too short at 7.0T to be measured with the pulse sequence used in this study which has a minimum TE of 10 ms. Therefore, results for T_2 values obtained by using monoexponential method for regions ROI1-4 of the rat brain are shown in figures 6.5 (A-D). In Fig. 6.5A we have the results for the 7-days old animals who have a mean value for T_2 of 62.64 ms (SD of $\pm$ 3.10) for regions 1 and 4 representing the cortical gray matter areas and 76.15 $\pm$ 4.4 for regions 2 and 3 which are representing the corpus callosum as one of the white matter areas of the brain (as shown in Fig. 6.4). In Fig. 6.5B (the 10 day old animals) the value for regions 2 and 3 dropped to 70.6 $\pm$ 3.8 ms while for regions 1 and 4 the value of T_2 remains at 61.9 $\pm$ 2.5 ms. Fig. 6.5C shows a further drop in T_2 value in regions 2 and 3 to 60.7 $\pm$ 3.4 with a slight drop in T_2 values for regions 1 and 4 to 58.4 $\pm$ 2.9 for the 14 days animals. Finally Fig. 6.5D shows a mean value of 40.6 with an SD of $\pm$ 1.41 for the mature animals for regions 1 and 4 while the value for regions 2 and 3 in this figure is 38 $\pm$ 1.1ms.

There were also no significant difference between 1 and 4 nor between regions 2 and 3 for the same animal when comparing these regions in the opposite sides of the cerebral hemisphere.

6.2.4 Discussion and Summary

In the case of in vivo T_2 measurements, the water content of the mature adult rat brain grey and white matter are 82 and 72% respectively (Norton 1975), compared to 89 and 87% for neonatal brain as estimated by Koenig *et al* 1990. Therefore, in MRI one would expect that the major difference between neonatal and adult grey and white matter would arise from a difference in water content. Although the results reported in this study are measured from regions, which we assume, represent the cortical grey matter (regions 1 and 4) and cerebral white matter (regions 2 and 3) in Fig. 6.4, one can not be certain that the difference in the T_2 values are merely due to the myelin content of the region unless a histological study supports this assumption. However, there is indirect evidence from these results that the drop in T_2 relaxation time in the middle regions of the mature animal brains are slightly higher than those in the peripheral regions which could be due to the former containing more myelinated fibres.

Neonatal grey and white matter are anatomically very different tissues, even though both are partially myelinated, and there is no reason to expect their relaxation values to have the same magnitude when comparing regions 2 and 3 with regions 1 and 4 for the 7-days old animals.

The results summarised in figures 6.5 A-D and suggests that T_2 value for white matter areas in the brain change markedly between young and mature animals. This can be explained by the fact that the young animals have less myelinated areas in the brain, so the tissues will be full of intra and extra-cellular water giving rise to an elevated T_2 values. As the animal grows, more myelin will develop covering more areas of the brain, and

myelin will therefore replace some of the extra and some of the intra-cellular water in the brain and hence reduce the T_2 values (see Chapter 2).

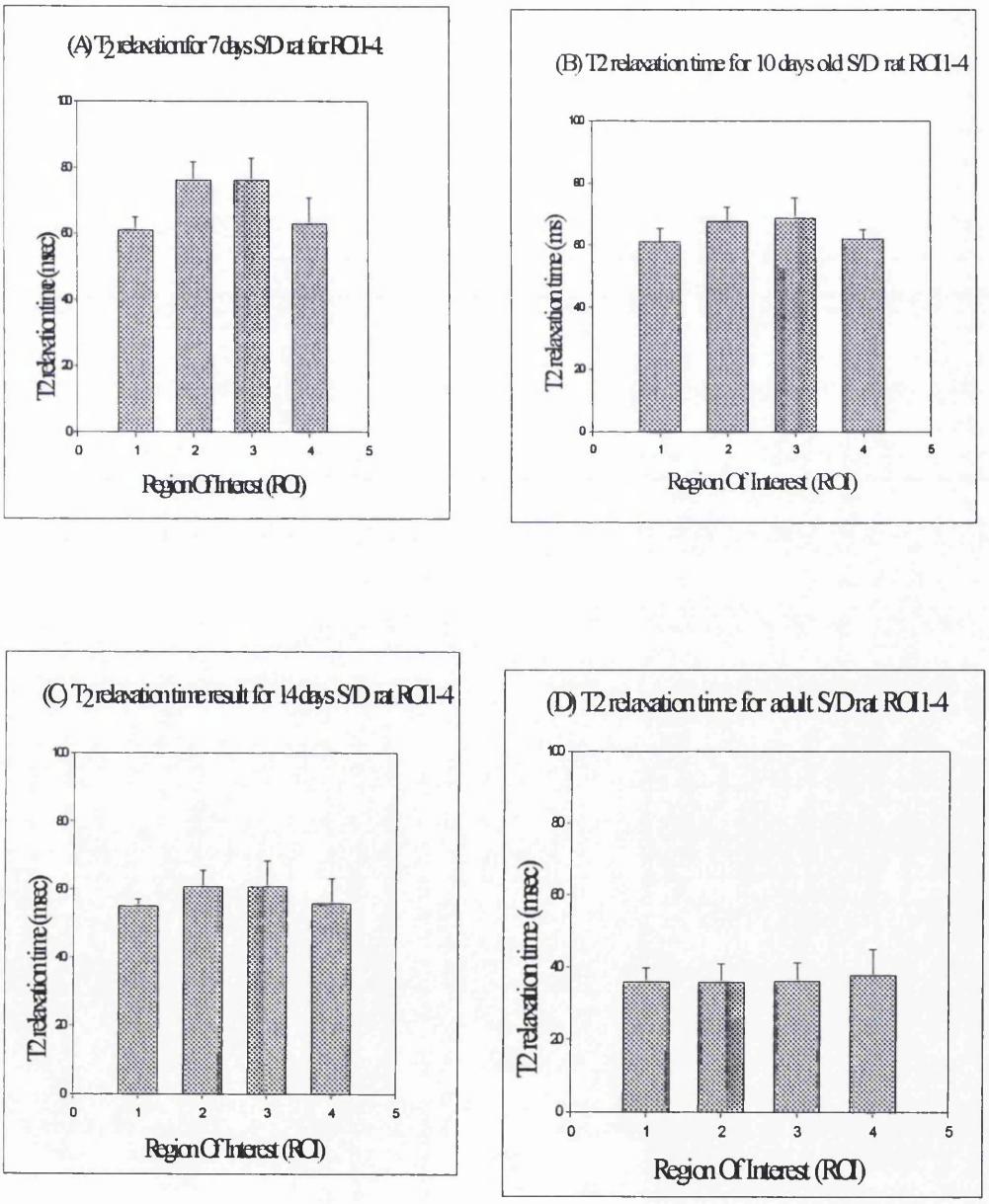

Fig. 6.5: *Results of T_2 relaxation times for animals of different age groups ranging from 7days to adults (n=6 for each age group) on a selected ROI-4 in fig 6.3.*

Figure 6.6 correlates the results of the in vivo T_2 relaxation times of figures 6.5A-D with age for the Sprague Dawley rat's brain at different sites, (ROI 1-4) which correspond to areas of white and gray matters. As can be seen from the figure there is a signal drop in the white matter areas as the age increases from 7 to 14 days. The T_2 value for the adult rats (over six weeks old) considerably dropped for both grey and white matter regions for two main reasons as follows:

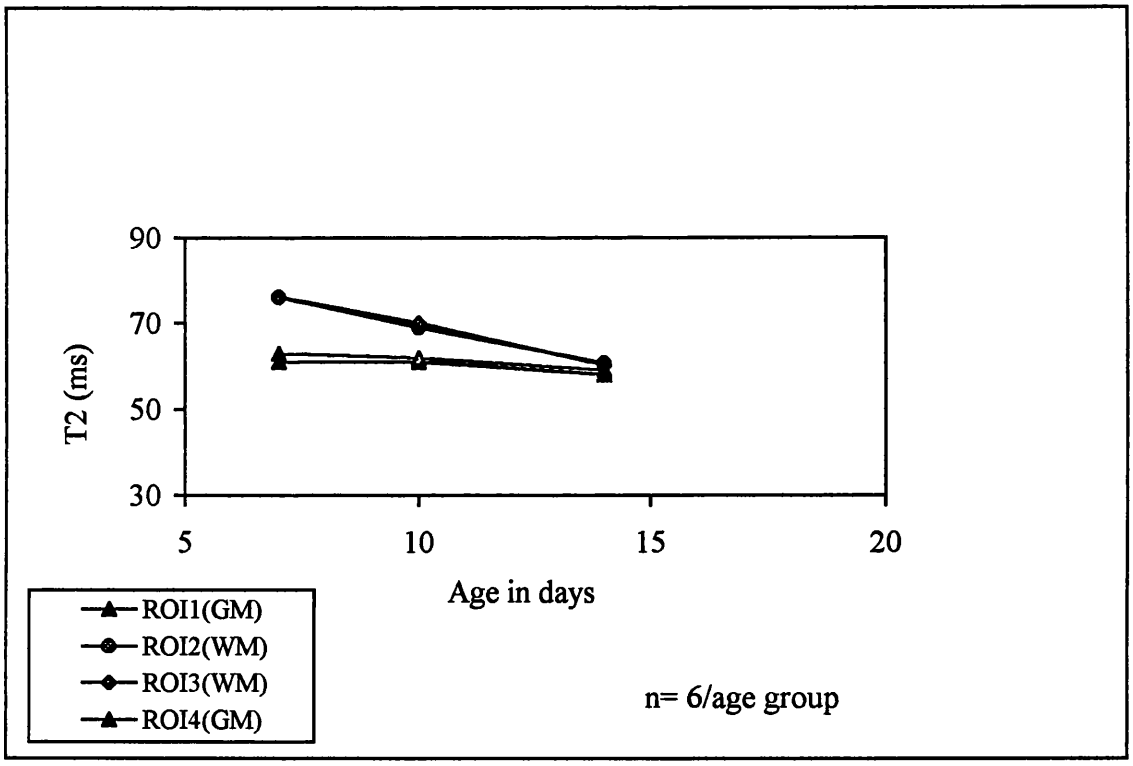

Fig..6.6: *In-vivo T_2 relaxation time for S/D rat brain plotted against animal age. ROI2 and 3 representing white matter areas of the brain are shown to be dropping relative to ROI1 and 4 representing gray matter areas as the animals develops.*

a. Firstly the multiplication of the glial cell replaces the water content of the brain as a whole.

b. Secondly the inverse proportionality of the T_2 relaxation and the field strength which is due to the susceptibility effect (Chen *et al* 1992) may become more pronounced with older animals as different types of tissue - which are completely formed at adulthood - create local interfaces between tissues of different magnetic susceptibility (Leach 1988). This finding will be discussed more thoroughly in chapter eight.

Finally, the results obtained from the mature S/D rat brain were added to the results shown in Fig. 6.6 to further show the amount of MRI signal loss due to myelin formation in a fully myelinated rat brain when compared to partly myelinated young animals brain (Fig. 6.7).

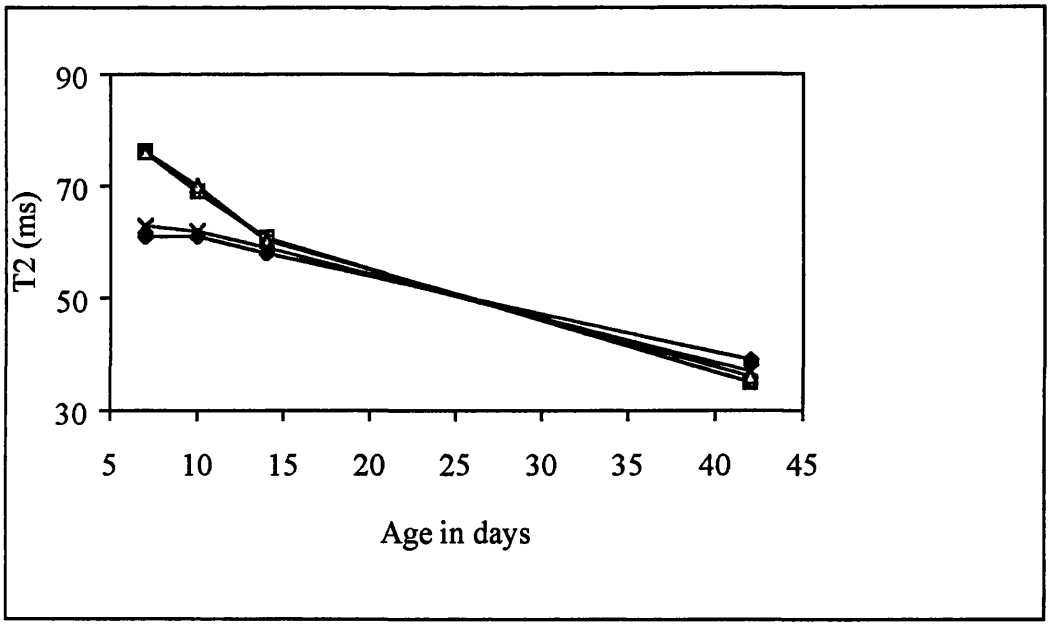

Fig. 6.7: *The results of In-vivo T_2 relaxation time for S/D adult rat brain plotted for ROI 1-4 (Fig 6.4) with adult data added to the results shown in Fig. 6.6.*

CHAPTER (7)

7. Diffusion Weighted Imaging (DWI)

7.1. Introduction

Magnetic Resonance Imaging is affected by physiological motion at different levels. Blood movement in large blood vessels which is predominantly in one direction, for instance, leads to a macroscopic flow effect, while flow at the capillary level which is effectively random leads to what are termed perfusion effects. Diffusion which reflects the effect of motion at the molecular level is however the primary focus of this chapter.

Considerable interest has recently emerged in the ability of MRI to image and measure molecular diffusion which is the result of the thermal, (so-called Brownian), random transitional motion that involves all molecules. This interest in diffusion results from the unique feature of this parameter, that it is a direct reflection of molecular mobility. Although this mobility also effects T_1 and T_2 relaxation times, the major difference remains that diffusion reflects only the translational motion while T_1 and T_2 reflects complex molecular interactions involving rotational motion and energy exchange. However, MRI is the only in-vivo technique available today that can non invasively measure diffusion directly from molecular translation.

In this chapter a brief description of the basic principles of diffusion measurement in tissue will first be given together with a review of how this parameter is quantified using MRI. The experimental method for collecting the data for this study will then be explained followed by the results which will eventually be discussed in the following chapter eight.

7.2. Diffusion principle and measurement.

Diffusion was originally described in nonuniform systems, where a macroscopic flux of differing species of particles could be observed. The classical Fick's Law describes how this flux density depends on the concentration gradient of the species (Stark et al 1992). Although this approach has been successfully applied to biological systems, it is found to be limited for in-vivo application because it relies on the introduction of a tracer in the medium. The other alternative is to monitor the diffusion process itself (i.e. the random molecular walk) by defining the diffusion coefficient (D) from the root mean square of the diffusion distance (r) according to the famous Einstein equation for three-dimensional motion (Le Bihan, 1991).

$$\langle r-r_0 \rangle^2 = 6Dt \qquad (7.1)$$

This technique is more suitable for NMR than the Fick's Law method.

The measurement of (D) is based on the insertion of a simple pulsed gradient on both sides of the 180° RF pulse in a spin echo imaging experiment (chapter 3). The purpose of these gradient pulses is to magnetically label spins carried by molecules. The first gradient pulse induces a phase shift of the spin transverse magnetisation, which depends on the spin position which is governed by the following relation assuming the gradient is along the z direction (Le Bihan, 1991).

$$\phi = \gamma \int_0^{\delta} G \; z_0 \; dt \qquad (7.2)$$

Where G is the gradient strength, and z_0 is the position of the spins along this direction. These phase shifts will be reversed by the 180° RF pulse. The second gradient

pulse will also induce a phase shift that depends on the position let us say z_1 . The net dephasing is therefore

$$\varphi = \gamma G \delta(z_1 - z_0) \qquad (7.3)$$

One immediately sees that for " static" spins $z_1 = z_0$, so the bipolar gradient pair will have no total dephasing effect. For "moving" spins, however, there is a net dephasing that will depend on the diffusion time. The net effect of the molecular diffusion on the spin echo (Hahn 1950) will be a signal attenuation (A) governed by the following relation

$$A = \exp(-bD) \qquad (7.4)$$

where D is the diffusion coefficient and b is a factor which depends only on the magnetic field gradients. For a pulsed gradient experiment (Stejskal-Tanner 1965) the b factor is expressed by the following expression

$$b = \gamma^2 G^2 \delta^2 (\Delta - \delta/3) \qquad (7.5)$$

Where δ is the gradient duration and Δ is the time interval between the pulse onsets (Fig. 3.9 chapter 3). In an MRI experiment the b value could be calculated numerically from equation 7.5 and may be confirmed by a phantom study by using equation 7.4.

Diffusion maps can be generated where the magnitude of the diffusion coefficient D along each axis is displayed in each pixel as shown in Fig. 7.1 where an example of Diffusion Weighted Images (DWI) are differently sensitized or "weighted". The degree of sensitization depends on the sensitizing gradient. Microscopic motion in biological tissues includes molecular diffusion and microcirculation of blood in the capillary network (perfusion). These two types of motion are inseparable and hence it is very difficult to quantify each type individually in -vivo. Therefore, in the MRI technique, the Apparent

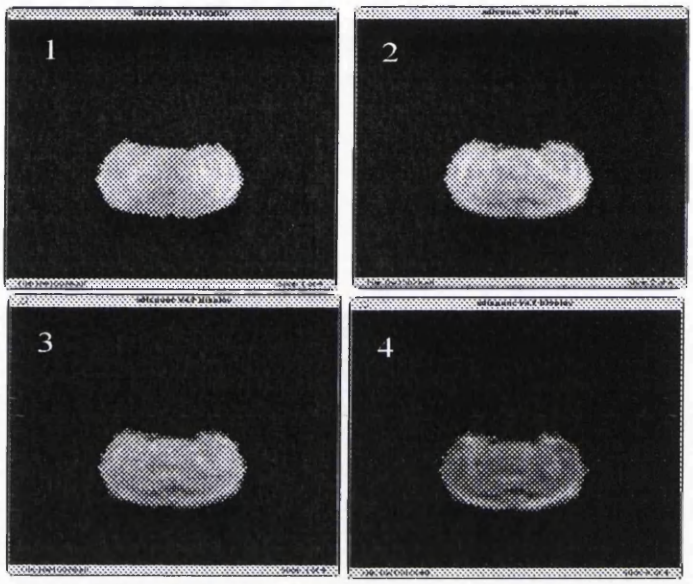

Fig 7.1: *Diffusion Weighted Images (DWI) of Sprague Dawley rat brain differently sensitized or "weighted", (1) without sensitizing gradient,(4) with maximum sensitizing gradient, (2 and 3) degrees in between.*

Diffusion Coefficient (ADC) is commonly used to replace D as shown in Fig. 7.2. The ADC integrates the effects of both diffusion and perfusion and it will equal D when diffusion is the only type of motion as demonstrated by Le Bihan and co-workers in phantom studies (Le Bihan *et al* 1988*)*. In vivo ADCs are often higher than expected due to perfusion contributions.

Diffusion is a three dimensional process. In biological tissues the molecular mobility may not be the same in all directions. This anisotropy (ANIS) may result from the physical arrangement of the medium or the presence of obstacles that restrict diffusion (e.g. the myelin sheath). In fact, diffusion is mathematically defined as a tensor, an array of

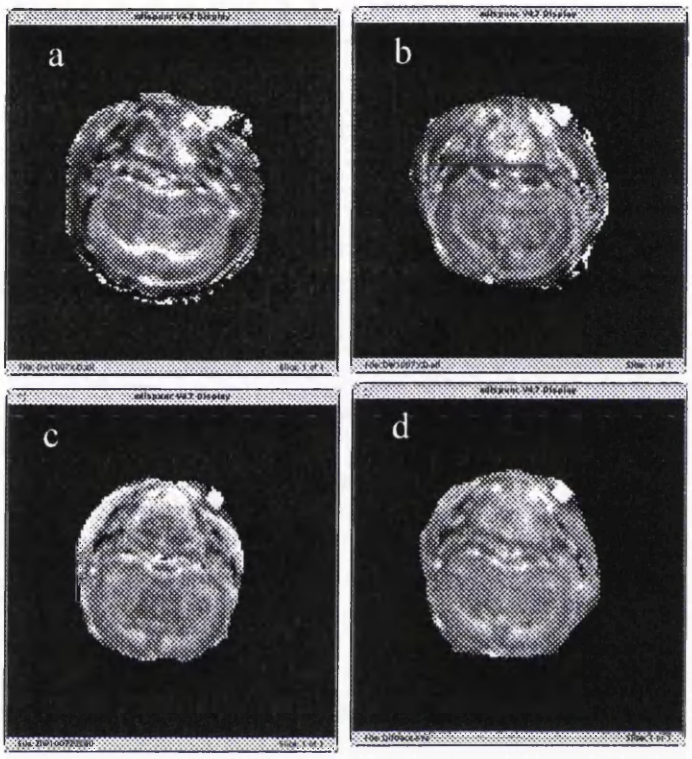

Fig. 7.2: *ADC maps for a 7 day old rat's brain fitted in different directions (a) ADC_x, (b) ADC_y, (c) ADC_z, (d) ADC_{xyz} (average).*

numbers that describe mobility rates in different directions. The degree of anisotropy can be quantified by using the ratio of the different diffusion tensor components (Coremans *et al* 1994). For measurements along x and y, for instance, the anisotropic diffusion ratio (ADR) in the xy plane could be

$$ADR = D_{xx}/D_{yy} \qquad (7.6)$$

This index can be used to determine the myelin fiber orientation in a given voxel as follows.

If the ADR>1, the fibers are predominantly oriented in the x direction. If ADR<1, the fiber direction is more likely to be along y. This technique will not be used in this study instead an overall numerical index of anisotropy ANIS will be calculated using formula 7.7 (see later).

7.3. Method of experiment

MR image data were collected from 32 Sprague Dawley (S/D) rats corresponding to four different age groups of seven, fourteen, twenty one and twenty eight days old (eight animals per group). The animal preparation was carried out in the same manner as in the T_2 relaxation measurement study (sec. 6.2.2). The animal head fixation in this study, which is more sensitive to motion, was secured by the removal of the skin from the surface of the skull which was then glued (using a cyanoacrylate adhesive) to a cylindrical delrin inserts which fitted into the imaging coils. Two different series of Delrin insert were used to fit into the 2.5 cm inner diameter RF coil used for the 7 and 14 day old animals and the bigger (3.5 cm i.d.) RF saddle coil which was designed and built specially for the study of the 21 and 28 days old animals.

Apparent Diffusion Coefficient (ADC) values were measured in a coronal plane using a diffusion-weighted stimulated echo acquisition sequence (Merboldt et al 1991). ECG and body peripheral temperature were continuously monitored. The sequence timing parameters were as follows: TR = 2s, echo time (TE) = 24 ms, mixing time (TM) = 200 ms, acquisition time = 2.2 min per image. The slice thickness was 1.5 mm, the field of view 2.56 cm and the image matrix of 128 x 64 was zero-filled to 128 x 128 to give a pixel resolution of 0.2 mm.

Rectangular diffusion-sensitizing gradient pulses were applied between the first and the second RF pulses, and after the third RF pulse of the STEAM sequence as shown in Fig. 3.9. The duration of each diffusion-sensitizing gradient pulse was 10 ms and the separation between the rising edges of the two gradient pulses was 214 ms. Gradient strengths of 0, 17, 25, and 30 $mT.m^{-1}$ were employed giving "b-factors" of 0, 440, 900, and 1350 x 10^{-9} $s.m^{-2}$ for diffusion sensitization along the x and y axes (corresponding respectively to horizontal and vertical directions in the image). The equivalent "b-factor" for diffusion-sensitization along the z axis were 0, 724, 1270 and 1780×10^{-9} $s.m^{-2}$ after taking into account crossterms arising from the slice selection (z) gradients. For measurements with diffusion-sensitization along the x and y axes, the readout gradient was applied along an orthogonal axis (e.g. y and x respectively), thereby minimising the errors due to additional crossterms in the calculation of "b-factors". Careful adjustment of the gradient system preemphasis was required to minimise artifacts arising from gradient-induced eddy currents.

ADC maps were calculated using a pixel by pixel log-linear fitting algorithm. ADC_{av} was calculated from the mean value of ADC in x y and z directions to give a parameter which is directionally independent and which was used to correlate diffusion with age as shown in Fig. 7.4.

A numerical index of anisotropy ANIS was calculated using the formula

$$ANIS_{ab} = \frac{ADC_a - ADC_b}{ADC_a} \times 100\% \qquad (7.7)$$

where ADC_a and ADC_b represent ADC values measured with the diffusion weighting gradients applied along separate orthogonal directions. Maps of ANIS were used to visually demonstrate the spatial distribution of anisotropy. A value of ANIS of zero, displayed as a midgray level on a linear gray scale, indicates an equal propensity to diffuse along both directions. Taking $ANIS_{xy}$ as an example, positive and negative values indicate preferential diffusion along the x and y direction respectively and are shown as regions of hyperintensity and hypointesity relative to the midgray level (Fig. 7.3).

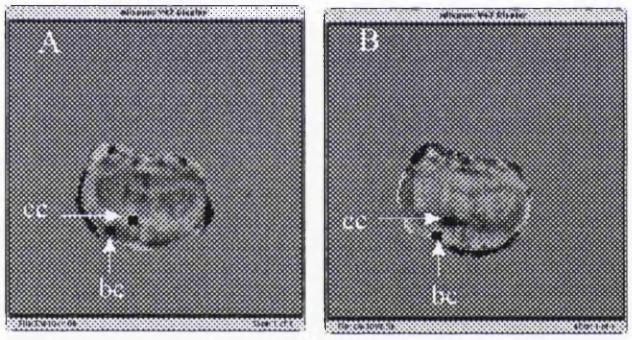

Fig 7.3: *Maps of diffusion anisotropy (ANSI)along (A) the x direction (B) the y direction. Hyperintensity of the corpus callosum (cc) in (A) indicates diffusion along the x direction. Hypointensity of the cc in (B) indicates restriction along the y direction.The region taken from the cerebral cortex (bc) is also shown.*

$ANIS_{xy}$ is not an absolute quantity, it is dependent upon the relative orientation of the animal's head within the Cartesian co-ordinate system. However, we believe that the positioning of the animals within the magnet bore was sufficiently consistent to allow a quantitative assessment of anisotropy in this manner, particularly because individual

animals were not moved between successive ADC measurements. The statistical significance of $ANIS_{xy}$ values was assessed by using SigmaStat software version 2 to perform paired *t*-test for mean ADC_x vs. mean ADC_y. Validation of ADC accuracy was performed using a distilled-water capillary tube positioned close to the animal's head during the imaging sequence.

7.4. Results

ADC_{av} values obtained from two regions of interest corresponding to the Corpus Callosum and the cerebral Cortex, as areas representing the brain myelinated white matter and the cortical gray matter, are shown in tables 7.1 & 7.2. respectively. In these

Animal age	Size (n)	Mean $10^{-10}.m^2.s^{-1}$	Std Dev
*cc 7 days	8	90.73	23.289
cc 14 days	8	76.30	11.942
cc 21 days	8	71.86	9.893
cc 28 days	8	62.10	5.343

Table 7.1 *Apparent Diffusion Coefficient values ($10^{-10}.m^2.s^{-1}$) for selected regions from the corpus callosum of the rat brain. Different age group were used*
* cc = Corpus Callosum

Animal age	Size (n)	Mean $10^{-10}.m^2.s^{-1}$	Std Dev
*bc 7 days	8	80.81	20.584
bc 14 days	8	66.30	7.715
bc 21 days	8	60.10	6.837
bc 28 days	8	58.985	10.870

Table 7.2 *Apparent Diffusion Coefficient values ($10^{-10}.m^2.s^{-1}$) for selected regions from the cerebral cortex of the rat brain. Different age group were used*
* bc = Cerebral Cortex

tables the means and standard deviations of the ADC are listed against each age group.

The differences in the mean values of ADC_{av} for the regions selected from Corpus Callosum (cc) among the age groups are greater than would be expected by chance; there is a statistically significant difference ($p < 0.01$), while the differences in the mean values of ADC_{av} for the regions selected from the Cerebral Cortex (bc) among the age groups are not great enough to exclude the possibility that the difference is due to random sampling variability; there is not a statistically significant difference ($p > 0.109$).

These results are summarised in the chart shown in Fig. 7.4. as a correlation of

Fig. 7.4: Apparent Diffusion Coefficient (ADC) for two regions in the rat's brain

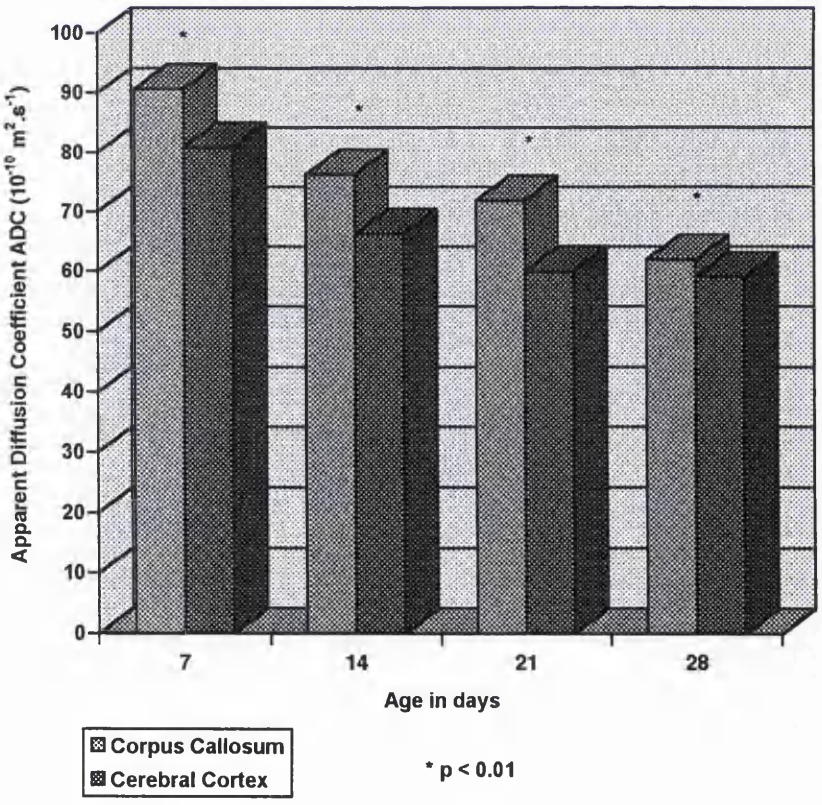

ADC_{av} against age. We notice that the ADC_{av} for the white matter areas of the brain (cc) were significantly greater than for the gray matter areas (bc) in the 7 day old animals ($p<.01$). This finding is markedly changed as the animals develop until it there is no significance at about 28 days, as shown in the figure. The ADC_{av} of the white matter areas is expected to further drop below that of the gray matter areas due to - among other factors - the diffusion anisotropy caused by the myelinated nerve fibres in the white matter areas of the brain (Wimberger *et al* 1995). This effect will be discussed thoroughly in chapter eight.

The above results are found to be in a good agreement with recent similar studies reported in the literature (Thornton J. *et al* 1997).

The results of the mean ANIS and SD values for white and gray matter regions are shown in tables 7.3 and 7.4 respectively for the same animals in each age group. These values, which represent the percentage change of ADC in the selected regions of interest (Fig 7.3) along the three orthogonal planes x-y, z-y and x-z, may suggest that diffusion is more restricted along the directions x and y and less restricted along the z direction of the Cartesian axes . This may be explained by the fiber orientation for these particular regions being predominantly along the z direction. The results in table 7.4 corresponding to gray matter areas did not show any significant difference of anisotropy along the three different directions.

Anisotropy in cerebral white and gray matter is based upon different structural mechanisms and thus must not be regarded as a purely myelination-specific phenomenon. These results were also found to be consistent with similar study in the human brain measured in a low magnetic field strength MRI systems (Wimberger *et at* 1995).

Animal age	ANISxy	ANISzy	ANISxz
7 days	24.4 ± 16.1	24.2 ± 12.4	8 ± 12.2
14 days	24.8 ± 16.4	25.7 ± 13.9	5.1 ± 10.4
21 days	26.0 ± 21.2	25.8 ± 18.8	7.3 ± 9.9
28 days	41.7 ± 38	21 ± 18	2.4 ± 9.4

Table 7.3: *Mean ANIS and SD values for white matter regions in eight experimental animals per age group.*

Animal age	ANISxy	ANISzy	ANISxz
7 days	-30.3 ± 19.5	-11.14 ± 10.9	-54.6 ± 16.6
14 days	-33.4 ± 25.1	-28.8 ± 16.1	-41.6 ± 18.6
21 days	-34.4 ± 22	-21.5 ± 17.3	-34.3 ± 25.3
28 days	- 35 ± 20.3	-18 ± 30	-25.3 ± 37

Table 7.4: *Mean ANIS and SD values for gray matter regions in eight experimental animals per age group.*

7.5 Discussion and Summary

The diffusion coefficient of water in tissue is two to three times less than its value in pure water. This is largely explained by the high viscosity of bulk water in tissue because of the presence of large molecules such as proteins in intracellular and extracellular spaces which represent obstacles to diffusion (Stark and Bradley 1992). Since

in heterogeneous tissues, the hindrance or restrictions to motion may not be the same for different directions, the measured diffusion coefficient may vary according to the direction of measurement (anisotropic diffusion). Examples of this have been shown in the cat (Moseley *et al* 1990) and more recently in human brain white matter (Chevert et al 1990). Water diffusion in grey matter does not generally exhibit anisotropy or restriction by impermeable walls (Le Bihan 1990). By contrast, diffusion in white matter is apparently extremely variable (Le Bihan 1991). In our study, for both the measurement of in vivo T_2 and the diffusion coefficient, the regions used were carefully selected in accordance with a previous histological study for the rat brain by Uzman (Uzman and Rumley 1958) which suggested that the calloso-tapetal of the corpus callosum (regions 2 & 3 Fig. 6.3) constitutes the main bulk of the myelinated fiber. Therefore, these region were thought to be the most appropriate for the study of the myelination process especially when we realise that the psychomotor performance in neonates is incomplete because neourosignals which are suppose to cross over through this area are arrested due to the lack of myelinated fibers (chapter 2).

The results shown in Fig. 7.4 were found to be in good agreement with those at low field (Back T. *et al* 1994) which may suggest an advantage in favour of the diffusion measurement over the T_2 method, namely the field strength independence of the diffusion. The anisotropic index maps of Fig. 7.3 were calculated using expression 7.7 . The values used represent the average apparent diffusion coefficient for the directions x & y which are drawn as the corresponding trace. Although the degree of anisotropy in these images is markedly different for the orthogonal directions used, we feel that measuring the degree of diffusion anisotropy in a heterogeneously oriented tissue like the brain white matter using

the diffusion tensor components (Basser *et al* 1994; Carlo Pierpaoli *et al* 1996) are more challenging than measuring their average diffusivity which is an under estimation of diffusion anisotropy (tables 7.3 and 7.4). Unfortunately we were unable to perform the diffusion tensor measurement because of a limitation of the MR system available at UCL at the time. The data needed for the tensor mapping requires the collection of four images in each of the six different directions involved in such a study, and this imposes an impractically long measuring time. A more sophisticated system and method (Turner et al 1990) will be needed for such study.

The results of the ADC_{av} for the rat brain show a significant change as the animal develops which is comparable to the T_2 results in chapter 6 which also show a similar effect. This may suggest that both techniques have been proved to be valuable in assessing brain maturation. The above results together with the T_2 results will be discussed thoroughly in chapter eight.

CHAPTER (8)

8. Discussion and Conclusion

8.1 Introduction

In the preceding chapters, different techniques have been used to assess the myelination process of the nerve fibres in the developing rat brain at the very high magnetic field of approximately 7T (300 MHz). A rat model was found to be most appropriate for this study as the developing rat brain reaches the adult stage at about approximately ten weeks (Uzman *et al* 1958) when compared to human brain which might take several years. This enables the monitoring of the rate of myelination over a relatively short period using the MRI technique.

In this chapter the results of the studies that we have performed will briefly be summarised and discussed. The results from those methods which have proved to be valuable will be compared with results from other similar studies. Finally, concluding remarks will be given towards the end of the chapter together with some discussion at future research options in the field of brain maturation and myelination research.

8.2 Discussion

Myelin in situ has a water content of approximately 40%. The dry mass of both CNS and PNS myelin is characterised by a high proportion of lipid (70-85%) and consequently a low proportion of protein (15-30%). In contrast, most biological membranes have a higher ratio of protein to lipid (chapter 2).

As the nervous system matures, portions of the PNS myelinate first then the spinal cord followed by the brain. In the rat, in which the CNS undergoes considerable development postnatally, the myelin begins to form at about 10 to 12 days (Uzman and

Rumley 1958). Although the maximal rate of accumulation of myelin in the rat is at about 20 days of age, in this species myelin accumulation continues at a decreasing rate throughout adulthood. At six month of age 60 mg of myelin can typically be isolated from one brain. This represents an increase of approximately 1500% over the brain myelin content of the 15 day old animal. During the same 5½ months period, the brain weight increases by 50-60% (Morell P. *et al* 1984). The above alterations in myelin content of the rat brain have been observed by using different MRI techniques as described in chapters five, six and seven of this thesis.

In conventional MRI, gray and white matter differentiation stems from a difference in mobile hydrogen density and associated T_1 and T_2 relaxation characteristics (Chapters 5 and 6) although it was shown in chapter 7, the MR image can be sensitive to the water diffusion coefficient. In the adult, the higher water content and less importantly, lower lipid and protein content of gray matter cause its relaxation times to be longer than those of white matter. Therefore, the higher water content of gray matter results in its higher spin density. The higher spin density in return results in its increased signal (regions 1 and 4 in Fig. 6.4 and Fig. 6.5) according to expression 5.1 (chapter 5). The lipid and protein content - the main components of the myelin (Chapter 2) - are of much less significance than water in determining gray and white matter differentiation on MRI. The protons of myelin, tightly bound in the fatty acid chains, do not contribute directly to gray and white matter differentiation. However lipid and protein concentration may indirectly affect contrast by changing the relaxation times of adjacent water protons (Holland *et al* 1986). This effect has also been demonstrated by Balaban and co-workers (Balaban *et al*

1992) by using the Magnetisation Transfer Contrast imaging techneque to monitor the effect of bound water to macromolecules in the MR signal (see conclusion).

Most authors, who have carried out similar studies, depend on a visual judgement or a qualitative assessment of the nerve tissue myelination which may be vulnerable to the difficulties mentioned earlier in chapter five, such as the pulse sequence conditions or other technical problems. To allow a more objective evaluation, tissue parameters such as the T_1, T_2 relaxation times and diffusion coefficient have to be calculated and quantified. To the best of our knowledge at the time of this study no similar work at a high field strength (7T) was available in the literature.

In the parts of the study aimed at measuring the T_1 relaxation times of the rat brain at 7T, the results shown in tables 5.3 and 5.5 indicate that there is no significant difference in contrast between the areas selected from the regions shown in figure 5.1 which represent white and gray matter in the rat brain. This may suggest that at 7T, all these regions have almost the same T_1 values resulting in difficulty in differentiating between different types of brain tissue.

The magnetic field dependence of tissue spin- lattice and spin-spin relaxation times (T_1,T_2) has been measured by a number of investigators, (Chen *et al* 1992.), the experiments involving field strengths ranging from 0.02-4.85T. The feasibility of high field > 4.85T imaging is an important issue for MR microscopists since it has long been recognized that an increase in magnetic field strength affords a greater SNR. Lower field measurements suggest the convergence of tissue T_1 values to that of water at very high fields, (Hoult *et al* 1986). If the T_1 difference between adjacent tissues becomes small at these higher field strength, the resulting image might not allow differentiation between

tissue types. In a clinical environment it is generally T_1 and T_2 that determine image contrast, but at high field the former will obviously be inadequate.

In vitro T_2 relaxation time results obtained in the lower field part of this study (at 0.47T), and which utilized undefined areas of cortex or whole brain, were compared with the results of similar in vitro studies by Besson et al in 1989 (T_2 = 77.7 ms ± 1.9 SD, rat brain) and recent in vivo studies at 1.5T by MacKay et al 1994 who claimed that they had also observed a short T_2 myelin bound water component (T_2 between 10 - 55 ms, human brain). It was found that the values reported in these studies and the outcome of our own studies were in good agreement.

The results obtained at 7T seem to be the only ones available and no similar data have been found so far in the literature. Although the values we obtained for T_2 are low when compared with previous studies at low field, (Bottomley et al 1984 ,T_2 = 76 ms, rat brain at 100 MHz.), they are believed to be accurate as the system and the pulse sequence used for the study were also tested on a reference phantom of $MnCl_2$. This test gave results for T_2 of 135 ms. with an SD of ± 13.74 ms which is consistent with the previous data collected on this system using a CPMG sequence. The observed low value of brain T_2 in our results is most probably due to the effects of magnetic susceptibility which are much more noticeable at such high magnetic fields.

In the case of in vivo T_2 measurements, the water content of the mature adult rat brain grey and white matter are 82 and 72% respectively (Norton 1975), compared to 89 and 87% for the neonatal brain as estimated by Koenig *et al* 1990. Therefore, in MRI one would expect that the major difference between neonatal and adult grey and white matter would arise from a difference in water content. Although the results reported in this study

are measured from regions, which we assume, represent the cortical grey matter (regions 1 and 4) and cerebral white matter (regions 2 and 3 in Fig. 6.4), one can not be certain that the difference in the T_2 values are merely due to the myelin content of the region unless a histological study supports this assumption. However, there is indirect evidence from these results that the drop in T_2 relaxation time in the middle regions of the mature animal brains are slightly higher than those in the peripheral regions which could be due to the former containing more myelinated fibres.

Neonatal grey and white matter are anatomically very different tissues, even though both are partially myelinated, and there is no reason to expect their relaxation values to have the same magnitude when comparing regions 2 and 3 with regions 1 and 4 for the 7 day old animals.

There are some difficulties in evaluations involving T_2 values. These were reported by Ono and co-workers (Ono *et al* 1993) when they carried out a similar study at a low field strength (1.5T). These can be summarised as follows:

i) The precise comparison of T_2 values is not possible unless the same MR instrument and the same pulse sequence are used.

ii) The ROI (region of interest) may affect the T_2 value. The use of a pure water phantom as a reference may enable data to be compared between different institutions.

As mentioned earlier, in tissue, the diffusion coefficient of water in tissue is two to three times less than its value in pure water. This is largely explained by the high viscosity of bulk water in tissue because of the presence of large molecules such as proteins in the intracellular and extracellular spaces which represent obstacles to diffusion (Stark and

Bradley 1992). Since in heterogeneous tissues, hindrance or restriction of molecular motion may not be the same for each direction, the measured diffusion coefficient may vary according to the direction of measurement (anisotropic diffusion). Examples of this have been shown in the cat (Moseley *et al* 1990) and more recently in human brain white matter (Chevert et al 1990). Water diffusion in grey matter does not generally exhibit anisotropy or restriction by impermeable walls (Le Bihan 1990). By contrast, diffusion in white matter is apparently extremely variable (Le Bihan 1991). Although these findings assume that myelin is an essential determinant of anisotropic diffusion, this assumption may no longer be sustainable in light of our results in tables 7.3 and 7.4 which demonstrate the insignificance of diffusion anisotropy in the selected regions of interest. These results agree with other findings in the literature such as Beaulieu and Allen 1994 who observed anisotropic water diffusion in the nonmyelinated olfactory nerve of the garfish and concluded that strutural features of the axon other than myelin are sufficient to give rise to anisotropy, even though myelin may still contribute. From the above discussion together with the result shown in Fig. 7.4, we may conclude that there is an observable anisotropic water diffusion in the axonal system, but this may not be attributed mainy to the presence of myelin sheath, other factor such as the structural features, the axons orintation and the selected regions may contribute to this phenomenon. In summary ADC maps may add information to the T_2 images about the size and course of unmyelinated as well as myelinated tracts in the brain as concluded by Tofts and co-workers (Tofts *et al* 1996).

The results shown in Fig. 7.4 were found to be in good agreement with others measured at low fields and with data from many diffusion studies that were conducted in

isolated biological tissues in the 1970s (Cooper *et al* 1974; Chang *et al* 1973; Cleveland *et al* 1976; Hansen *et al* 1971 and Brownstein *et al* 1979). This result also suggests an advantage in favour of the use of diffusion measurement over T_2 in that diffusion is field strength independent. Since the conclusion of this study in 1997 many similar studies at low magnetic field have been conducted (Miot-Noirrault *et al* 1997; Sie *et al* 1997; Prayer *et al* 1997 and Nakagawa 1998). Recently, just before the submission of this thesis some similar work has been reported in the literature by a group in the Institute of Child Health, U.C.L. (Calamante *et al* 1999). In their work they have investigated the evolution of water diffusion, perfusion, T_1 and T_2 at a high field strength of 8.5T (approximately 360 MHz) following permanent middle cerebral artery occlusion in the adult rat. Results of the control animals (pre-occlusion) were as follows:

1) T_1 relaxation time mean value was 1718 ± 25 ms.

2) T_2 relaxation time mean value was $42 \pm .9$.

3) Apparent Diffusion Coefficient mean value was 0.83×10^3 mm^2/sec.

The above values are consistent with the values reported in our present study which are summarised in tables 5.4 and 5.6 for T_1 relaxation, figure 6.5c for T_2 relaxation and tables 7.1 and 7.2 for ADC.

The anisotropy index maps of Fig. 7.3 were calculated using the expression 7.7. The values used in this expression represent the average apparent diffusion coefficient for the directions X & Y which are given in tables 7.3 and 7.4. Although the degrees of anisotropy in these images are markedly different for the orthogonal directions used, we feel that measuring the degree of diffusion anisotropy in a heterogeneously oriented tissue

like the brain white matter using the diffusion tensor components (Basser *et al* 1994; Pierpaoli *et al* 1996) are more challenging than measuring their average diffusivity although this is an under estimation of the diffusion anisotropy (tables 7.3 and 7.4). Unfortunately we were unable to perform the diffusion tensor measurement because of a limitation of the MR system available at UCL at the time. The data needed for the tensor mapping requires the collection of four images in each of the six different directions, and this requires an impractically long measuring time. A more sophisticated system and method (Turner *et al* 1990) will be needed for such study.

In our study for the measurements of in vivo T_2 and the diffusion coefficient, the regions used were carefully selected in accordance with a previous histological study for the rat brain by Uzman (Uzman and Rumley 1958) which suggested that the calloso-tapetal of the corpus callosum (regions 2 & 3 Fig. 6.3) constitute the main bulk of the myelinated fibers. Therefore, these region were thought to be the most appropriate for a study of the myelination process. Further evidence for this comes from the observations that the psychomotor performance in neonates is incomplete because neurosignals which are supposed to cross over through this area are arrested due to the lack of myelinated fibers (chapter 2).

8.3 Conclusion

In conclusion, myelin characterization solely based on the determination of T_1 relaxation time in the ROI's (at 7T), does not seems to be possible for two main reasons. Firstly, the T_1 values of soft tissues (brain) are proportional to the magnetic field strength, i.e. T_1 increases as the magnetic field increases. Therefore, it will approach values closer to the free water proton values at very high fields such as 7T. This will result in all the brain

tissue having very similar T_1 values. Hence, discrimination between different tissue types such as grey and white matter will not be possible. This result is consistent with the outcome of a similar study by Wimberger in 1995 (Wimberger *et at* 1995). Secondly, the S/N ratio which is expected to increase with field strength and hence provide a better quality image is also associated with a drop in the signal due to the increase in T_1 relaxation value according to the relation

$$S(t) = P *[1-\exp(-TR/T_1)]$$

This may explain the possibility of producing a good quality image at fields as low as 650 Gauss (Stark and Bradley 1992).

For in vitro T_2 measurement there is evidence in the literature of a multiexponential water spin-spin relaxation decay due to heterogeneity, (Stewart and Bradley 1993) which also appears to have been detected in our Minispec system studies at a low field. This may suggest that spin-spin relaxation could provide a direct method of determining the presence of intact myelin at low fields.

There is no evidence of a better multiexponential fit to the data collected in the 7T system. This is due to the fact that the minimum value of the echo time TE in the 7T system when using the STVE pulse sequence is limited to 10 ms which would prevent signals from tissues with T_2 relaxation times of less than 10 ms from being detected. Also, the number of measured data points was only six compared to 20 in the Minispec and this will reduce the measured value of T_2 as demonstrated by Wesbey (Wesbey *et al* 1984). In that study it was found that the value of T_2 for a water sample changed from 519 ms when the data was collected by using two CPMG spin-echoes to 719 ms with four CPMG spin-echoes till it reached a value of 887 ms when ten CPMG spin-echoes were used.

Analytical models for T_2 relaxation measurement of the rat brain at very high fields (7T) against which to compare the results of the in vivo T_2 measurements in this study are not available, therefore an experimental approach is required. The data here represent the first such measures of cerebral T_2 at these fields. Further, the fact that T_2 decreases as one moves towards 300MHz (Chen *et al* 1992) suggests that previously accepted theoretical models of relaxation are probably inaccurate (Gadian 1982). The T_2 field dependence will largely affect the detection of any very short T_2 component of heterogeneous tissues such as the brain. In addition, if one considers the dimensions of the pixels and the magnitude of the gradients involved in this study, it becomes clear that diffusion may further impact on the detected NMR signal. This observation was also made by Wesbey and co-workers (Wesbey *et al* 1984) when they measured the T_2 for water in the absence of an applied magnetic gradient, even utilizing only two CPMG spin-echoes. The measured value was 519 ms compared to 177 ms for the same water sample when measured using the same system with a spin echo MRI pulse sequence with all gradients fully on.

When diffusion measurement are made parallel to the direction of the nerve fiber, diffusion is much less restricted resulting in higher measured diffusion coefficient. This effect together with the results of the in vivo T_2 relaxation time measurements (Fig. 6.6) suggest that MRI can differentiate grey matter, myelinated and unmyelinated white matter and grades of myelination on the basis of difference in intensity. If we consider in depth the alterations of this signal intensity we will find that signal intensity in MRI depends on various factors including proton density, T_1 and T_2 of protons and the pulse sequence used (Chapters 3, 4 & 5). As most protons in the brain that contribute to the signal in MR images are water protons, differences in water content will lead to differences in signal

intensity on the images. But differences in signal intensity can not be attributed completely to differences in water content. The mobility (diffusion, perfusion and flow) and structural organisation of water protons (free and bound to macromolecules) and their biochemical environment (lipid, proteins (Chapter 3)) also influence the relaxation parameters and hence the signal intensity. As discussed in Chapter two, major changes occur in the biochemical composition of the brain mainly as a result of myelin deposition and loss of tissue water. Myelin is predominantly deposited in white matter. Loss of tissue water involves both white and grey matter, but white matter to a greater extent. All these alterations lead to changes in T_2 in the grey and white matter which may explain the changes in the measured signal intensity in figures 6.5. In the Apparent Diffusion Coefficient results Fig. 7.4 the reduction in signal intensity with age can be explained by the decreased water mobility through the successive lipid layers (Le Bihan *et al* 1990) as it has been shown by NMR dispersion studies that the myelin sheath is somewhat permeable to water (Koenig *et al* 1990). In comparing these two figures one may notice the signal drop in both cases with maturation. This was explained earlier as being due to the associated reduction in the amount of the water contents (^1H protons) in the corresponding selected regions. In summary, based on these, both measurements may be used for the assessment of myelination specially when one realises that these two intrinsic tissue parameters are interrelated in heterogeneous tissue in vivo as found by several workers in previous studies (Wesbey *et al* 1984; Mansfield *et al* 1982).

In conclusion, the relaxation properties of myelin are unique (Chapter 3). Different approaches are therefore required to assess myelination using NMR. The measurement of Diffusion and T_2 have proved to be valuable. It seems that the T_2- weighted images and

the myelin fibre orientation maps may be useful in gaining a better understanding of white matter diseases, such as multiple sclerosis or abnormal white matter development in children. To fully evaluate this will require studies in which the MRI assessment of myelination are accompanied by developmental testing and histological studies both before and after an intervention which alters the progress of myelination.

Another promising area of interest for future studies is the application of Magnetisation Transfer Contrast (MTC) which has been reported by Balaban *et al* 1992, to cause a gross reduction in pixel intensity in myelinated white, but not grey, matter when a broad background of proton resonances (with a short T_2 and thus not detectable) are saturated by off-resonance radiation at low fields. A limitation of this technique may be the amount of the RF power deposition in the tissue. In our primary studies using MTC for the assessment of the myelination (not reported here) pilot images have been produced which indicate that the technique may be useful at least in animal studies.

REFERENCES

1) Back T.; Hoehn-Berlage M.; Kohno K.; Hossmann K.A. (1994). Diffusion Nuclear Magnetic Resonance Imaging in Experimental Stroke. Stroke (25) 494-500.

2) Balaban R.S.; Ceckler T.L (1992). Magnetization Transfer Contrast in Magnetic Resonance Imaging. Mag. Res. Quarterly (8) 2, 116-137.

3) Basser P.J; Mattiello J.; Le Bihan D. (1994). MR Diffusion Tensor Spectroscopy and Imaging. Biophs. J.(66) Jan. 259-267.

4) Barroilhet L.E.; Moran P.R.(1975). Nuclear Magnetic Resonance (NMR) relaxation spectroscopy in tissue. Med. Phys. 2,4 191-194.

5) Beaulieu C.; Allen P.S. (1994). Determination of anisotropc water diffusion in nerve. Mag. Res. Med. (31) 394-400.

6) Besson J.A.O.; Greentree S.G.; Foster M.A.; Rimmington J.E. (1989). Regional variation in rat brain proton relaxation times and water content. Mag. Res. Img. (7) 2: 141-143.

7) Bhat S.; Barbarese E.; Pfeifferf S.E. (1981). Requirement for nonoligodendrocyte cell signals for enhanced myelinogenic gene expression in long-term cultures of purified rat oligodendrocytes. Proc Natl Acad Sci USA. (78) 1283-1287.

8) Bloch F.; Hansen W.W.; Packard M.E. (1946). Nuclear induction , Phys. Rev.(69) 127.

9) Bologa L. (1985). Oligodendrocytes, key cells in myelination and target in demyelinating diseases. J Neurosci Res. (14) 1-20.

10) Bottomley P.A.; Foster T.H.; Argersinger R.E; Leach M. Pfeifer (1984). A review of normal tissue hydrogen NMR relaxation mechanisms from 1-100 MHz: Dependence on tissue type, NMR frequency, temperature, species, excision and age. Med Phys. 11(4) 425-448.

11) Brady R.O.; Quarles R.H. (1973).The enzymology of myelination. Mol Cell Biochem. (2) 23-29.

12) Brownstein K.R.; Tarr C.E. (1979). Importance of classical diffusion in NMR studies in biological cell. Phys. Rev. (19) 2446-53.

13) Braun P.E. (1984). Molecular organization of myelin. In: Morell P. Myelin, 2nd ed. New York: Plenum Press, 97-116.

14) Brody B.A.; Kinny H.C.; Kloman A.S.; Gilles F.H. (1987). Sequence of central nervous system myelination in human infancy. An autopsy study of myelination. J Neuropathol Exp Neurol. (46): 283-301.

15) Bydder G.M.; Steiner R.E.; Young I. (1982). Clinical NMR imaging of the brain. AJR 139, 215.

16) Cady E.B. (1990). Clinical Magnetic Resonance Spectroscopy. Plenum Press, New York.

17) Calamante F.; Lythgoe M.F.; Pell G.S.; Thomas D.L.; King M.D.; Busza A.L.; Sotak C.H.; Williams S.R.; Ordidge R.J.; Gadian D.G. (1999). Early changes in water diffusion, perfusion, T_1 and T_2 during focal cerebral ischemia in rat studied at 8.5T. MRM 41:479-485.

18) Chang D.C.; Rorschach H.E.; Nichols B.L.; Hazlewood C.F. (1973). Implication of diffusion coefficient measurements for the structure of cellular water. Ann NY Acad. Sci. (204) 434-43.

19) Chen J.H.; Avram H.E; Crooks L.E.; Arakawa M.; Kaufman L.; Brito A.C.(1992). In Vivo Relaxation Times and Hydrogen Density at 0.063-4.85T in rats with Implanted Mammary Adenocarcinomas. Radiology, (184) 427-434.

20) Chenevert T.L.; Brunberg J.A.; Pipe J.G. (1990). Anisotropic Diffusion in Human White Matter: Demonstration with MR Techniques in vivo. Radiology, (177) 401-405.

21) Cleveland G.G.; Chang D.C.; Hazlewood C.F. (1976). Nuclear magnetic resonance measurement of skeletal muscle. Anisotropy of the diffusion coefficient of the intercellular water. Biophys. J. (16) 1043-53.

22) Cooper R.L.; Chang D.B.; Young A.C. (1974). Restricted diffusion in biophysical systems. Biophys. J. (14) 161-77.

23) Coremans J.; Luypaert R.; Verhelle F.; Stadnik T.; Osteaux M. (1994). A methode for myeiln fiber orientation mapping using diffusion-weighted MR images. Mag. Res. Img. (12) 3: 443-454.

24) Damadian R.; Goldsmith M.; Minkof L. (1977). NMR in cancer: XVI, FONAR Image of the life human body, Physiol. Chem. Phys.(9) 97-100.

25) Davis P.L.; Kaufman L; Crooks L.; Mrargulis A.R (1981). NMRI in medicine edited by R.L Witcofski.

26) Dickinson W.C. (1950). Dependence of F^{19} Nuclear Resonance Position on Chemical Compound. Phys. Rev. 77,736.

27) Edelstein W.A.; Hutchison J.M.S.; Johnson G.; Redpath T.W. (1980). Spin warp NMR Imaging. Phys. Med. Biol. (25) 751.

28) Edelstien W.A.; Bottomley P.A.; Hart H.R.; Smith L.S. (1983). Signal, noise, and contrast in Nuclear Magnetic Resonance (NMR) Imaging. J Comp Asst Tomog. 7(3): 391-401.

29) Fischer H.W.; Rinck P.A.; Haverbeke Y.V.; Muller R.N. (1990). Nuclear relaxation of human body gray and white matter: Analysis of field dependence and implications for MRI. Mag Res Med. (16) 317-334.

30) Friede R.L.; Bischhausen R. (1982). How are sheath dimensions affected by axon caliber and inter node length? Brain Res. (235) 335-350.

31) Friede R.L. (1972). Control of myelin formation by axon calibre (with a model of the control mechanism). J Comp Neurol. (144) 233-252.

32) Gadian D.G. (1982). Nuclear Magnetic Resonance and its Application to living Systems. Clarendon Press, Oxford.

33) Hahn E.L. (1950). Spin Echoes. Phys. Rev. (80) 580-594.

34) Hansen J.R. (1971). Pulsed NMR study of water mobility in muscle and brain tissue. Biochem. Biophys. Acta. (230) 482-6.

35) Harvey P.S.; Tofts J.K.; Morris D.G. and Ron M.A. (1991). Sources of T_1 Variance in Normal Human White Matter. Mag. Reson. Imag. 9, 53-59.

36) Hayes C.E.; Edelstein W.A; Schenck J.F.; Muller O.M; Eash M.(1985). An efficient highly-homogeneous radiofrequency coil for whole body imaging at 1.5T. J. Magn. Reson. 63, 622-8

37) Holland B.A.; Haas D.K.; Norman D.; Brant-Zawadzki M.; Newton T.H. (1986). Magnetic Resonance Imaging of normal brain maturation. AJNR, 7: 201-208.

38) Hoult D.; Richards R. (1976). The signal to noise ratio of the NMR experiment. J. mag. Res. 24: 71-85.

39) Hoult D.I.; Chen C.N.; Sank V.J. (1986). The field dependence of NMR imaging. II. Arguments concerning an optimal field strength. Mag. Res. Med. (3) 730-46.

40) Johnson G.; Ormerod I.; Tofts P.; Macmanus D. (1987). Accuracy and precision in the measurement of relaxation times from nuclear magnetic resonance images. BJR, 60, 143-153.

41) Keene M.F.L.; Hewer E.E. (1931). Some observations on myelination in the human central nervous system. J Anat. (66) 1-13.

42) Kirschner D.A. ; Ganser A.L., Caspar D.L.D. (1984). Diffraction studies of molecualr organization and membrane interactions in myelin. In: Morell P. Myelin, 2nd ed. New York: Plenum Press, 51-95.

43) Koeing S.H.; Brown R.D.; Spiller M.; Lundbom N. (1990). Relaxometry of Brain: Why white Matter Appears Bright in MRI. Mag. Res. Med. (14) 482-495.

44) Lassmann H.; Ammerer H.P.; Kulnig W. (1978). Ultrastructural sequence of myelin degradation. Wallerian degeneration in rat optic nerve. Acta Neuropathol, 44, 91-102.

45) Lauterbur P.C. (1973). Image information by induced local interaction: Examples employing NMR. Nature (242) 190-191.

46) Leach M.O. (1988). Spatially localised NMR, The physics of medical imaging ,S. Webb editor. IOP Pub. Adam Hilger, Bristol and Philadelphia.

47) Le Bihan D.; Breton E.; Lallemand D.; Aubin M.; Vignaud J.; Jeantet M. (1988). Separation of Diffusion and Perfusion in Intravoxel Incoherent Motion MR Imaging. Radiology (168) 497-505.

48) Le Bihan D.; Turner R.; Douek P. (1990). Is Water Diffusion in Human Brain Restricted. (Absct.) 9th ann. SMRM New York. (1) 377.

49) Le Bihan D. (1991). Molecular Diffusion Nuclear Magnetic Resonance Imaging. Mag. res. Qurt. (7) 1-30.

50) Ludin H.P. (1984). Function of myelin in the normal nerve fiber. Neuropediatrics. (15) (Suppl), 21-23.

51) MacKay A.; Whittall K.; Adler J.; Li D.; Paty D.; Graeb D. (1994). In Vivo Visualization of Myelin Water in Brain by Magnetic Resonance. Mag. Res. Med. (31) 673-677.

52) Mansfield P.; Grannell P.K. (1973). NMR diffraction in solids, J. Phys. C: Solid state physics(6) L422-6.

53) Mansfield P.; Morris P.G. (1982). NMR Imaging in Biomedicine, in Advances in MR, suppl. 2 (ed. J.S. Waugh). Academic Press, New York.

54) McDonald W.I.; Ohlrich G.D. (1971). Quantitative anatomical measurements on single isolated fibres from the cat spinal cord. J Anat; (10) 191-202.

55) McManus D.; Bartlet P. (1986). Image Contrast in Nuclear Magnetic Resonance Imaging. Radiography, (52) 103-108.

56) Merboldt K.; Hanicke W.; Frahm J. (1991). Diffusion Imaging Using Stimulated Echoes. Mag. Res. Med. (19) 233-239.

57) Miot-Noirault E.; Barantin L.; Akoka S.; Le Pape A. (1996). T_2 relaxation time as a marker of brain myelination: exprimental MR study in two neonatal animal models. J.Neur.Sci.Meth. (72) 5-14.

58) Moon R.B.; Richard J.H. (1973). Determination of Intracellular pH by ^{31}P Magnetic Resonance, J. Biol. Chem.(248) 7276-8.

59) Morell P.; Quarles R. H.; Norton W.T. (1984). Formation, structure and biochemistry of myelin. In: Morell P,ed. Myelin, 2nd ed. New York: Plenium Press. 109-136.

60) Morris P.G. (1986). Nuclear Magnetic Resonance Imaging in Medicine and biology/ Peter. Oxford: Clarendon.

61) Moseley M.E.; Cohen Y.; Kucharczk J. (1990). Diffusion weighted MR imaging of anisotropic water diffusion in cat central nervous system. Radiology (176) 439-46.

62) Nakagwa H. (1998). Normal myelination of anatomic nerve fiber bundles: MR analysis . AJNR (19) 6: 1005-6.

63) Norton W.T. (1975). Myelin: Structure and Biochemistry. In the nervous System. vol. 1: The Basic Neurosciences. (ed. Tower D.B.) Raven Press. New York.

64) Norton W.T.; Siegel G.J.; Albers R.W.; Agranoff B.V.; Katzman R. (1981). Formation, structure and biochemistry of myelin. In: Basic neurochemistry, 3rd ed. Boston: Little, Brown and Company, 63-92.

65) Norton W.T.; Cammer W. (1984). Isolation and characterization of myelin. In: Morell P. Myelin, 2nd ed. New York: Plenum Press, 147-195.

66) Ono J.; Kokada R.; Imai K.; Itagaki Y.; Tanaka J.; Inui K.; Nagai Toshisaburo; Sakurai K.; Harada K.; Okada S. (1993). Evaluation of myelination by means of the T_1 value on magnetic resonance imaging. Brain & Development. (15) 433-438.

67) O'Brien J.S. (1965). Stability of the myelin membrane. Science, (147) 1099-1107.

68) O'Brien J.S. (1970). Lipids and myelination. In: Himwhich W.E., ed. Developmental neurobiology. Springfield: Thomas, 262-286.

69) Pettmann B.; Delamunoy J.P.; Courageot J. Devilliers G. Sensenbrenner M. (1980). Rat brain glial cells in culture: effect of brain extracts on the development of oligodendroglial-like cells. Dev Biol. (75) 278-287.

70) Pierpaoli C.; Basser P. (1996). Toward a Quantitative Assessment of Diffusion Anisotropy. Mag. Res. Med. (36) 893-906.

71) Poser C.M. (1961). Leukodistrophy and the concept of dysmyelination. Arch Neurol. (4) 323-332.

72) Prayer D.; Robert T.; Barkovich A.J.; Pryer L.; Kucharczk J.; Moseley M.; Ariefff. A. (1997). Diffusion weighted MRI of myelination in rat brain following treatment with gondal hormones. Neuroradiology (39) 5: 320-5.

73) Proctor W.G.; Yu F.C. (1950). The Dependence of a Nuclear Magnetic Resonance Frequency upon Chemical Compound. Phys. Rev. 77, 717.

74) Purcell E.M.; Torrey H.C.; Pound R.V. (1946). Resonance absorption by nuclear magnetic moment in a solid, Phys. Rev.(69) 37-8.

75) Pykett I.L. (1982). NMR in medicine. Scientific American. (246) 54-64.

76) Raine C.S. (1984). Morphology of myelin and myelination. In: Morell P. Myelin, 2nd ed. New York: Plenum Press, 1-50.

77) Remahal S.; Hildebrand C. (1982). Changing relation between onset of mylenation and axon diameter range in developing feline white matter. J neurol sci. (54) 33-45.

78) Rinck P.A. (1990). An Introduction to Magnetic Resonance in Medicine. Thieme Med. Pupl. New York.

79) Ritchie J.M. (1984). Physiological basis of conduction in myelinated nerve fibres. In: Morell P. Myelin, 2nd ed. New York: Plenum Press, 117-145.

80) Sie L.T.; van der Knaap M.S.; van Wezel-Meijler G.; Valk J. (1997). MRI assessment of myelination of motor and sensory pathways in the brain of preterm and term-born infants. Neuro. Ped. (28) 2: 97-105.

81) Singer M. (1968). Penetration of labelled amino acids into the peripheral nerve fibre from surrounding body fluids. In: Wolstenholme G.E.W.; O'Connor M., eds. Ciba Foundation symposium. Growth of nervous system. London: Churchill. 200-215.

82) Stark D.; Bradley W. (1992). Magnetic Resonance Imaging. Vol. 1 (2en ed.) Mosby publ. St. Louis.

83) Stejskal E.O.; Tanner J.E. (1965). Spin diffusion measurements: Spin echoes in the presence of a time-dependent field gradient. J. Chem. Physol. 42:288-292.

84) Stewart W.A.; MacKay A.L.; Whittall K.P.; Moore G.R.W.; Patty D.W. (1993). Spin-spin relaxation in experimental allergic encephalomyelitis. Analysis of CPMG data using non-linear least square method and linear inverse theory. Mag. Res. Med. (29) 767-775.

85) Szuchet S.; Polak P.E.; Yim S.H. (1986). Mature oligodendrocytes cultured in absence of neurons recapitulate the ontogenic development of myelin membranes. Dev Neurosci. (8) 208-221.

86) Thornton J.S.; Ordidge R.J.; Cady B.; Clemence M.; *et al* (1997). Anisotropic water diffusion in white and gray matter of neonatal piglet brain before and after transient hypoxi-iscaemia. Mag. Res. Img. (15) 1-7.

87) Tofts P.B.; Leth H.; Peitersen B.; Lou H.C.; Thomsen C. (1996). The apparent diffusion coefficient of water in gray and white matter in the infant brain. J. Com. Ass. Tom. 20(6):1006-1011.

88) Turner R.; Le Bihan D.; Maier J. Varek R.; Hedges L.; Pekar J. (1990). Echo-Planar Imaging of Intravoxel Incoherent motion. Radiology (177) 407-414.

89) Uzman L.; Rumley M. (1958). Changes in the Composition of the Developing Mouse Brain During Early Myelination. JNS (3) 170-184.

90) Van der Knaap M.S. (1991). Myelination and Myelin disorder. Thesis, Utrecht, Netherland.

91) Walton, Sir John (1985). Brain's diseases of the nervous system. 9th ed. Oxford, Oxford University Press. 298-321.

92) Waxman S.G. (1985). Structure and function of the myelinated fiber. In: Koetsier J.C., ed. Handbook of clinical neurology, vol 3. Demyelinating diseases. Amsterdam: Elsevier. 1-28.

93) Wesby G.E.; Moseby M.E; Ehman R.L (1984). Translational molecular self-diffusion in magnetic resonance imaging. I. effects on observed spin-spin relaxation. Invest. Radiol. 19, 484.

94) Wimberger D.; Roberts T.; Barkovich J.; Prayer L. Moseley M.; Kucharczyk J. (1995). Identification of Premyelination by Diffusion-Weighted MRI. J. Comp. Ass. Tom. (19) 28-33.

95) Young I.R.; Bryant D.J.; Payne J.A (1985). Variation in Slice Shape and Absorption as Artifacts in the Determination of Tissue Parameters in NMR Imaging. Magn. Reson. Med. 2, 355-389.